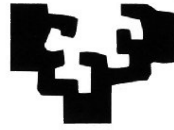eman ta zabal zazu

Universidad del País Vasco
Euskal Herriko Unibertsitatea
The University of the Basque Country

Physical principles underlying structure, mechanics and dynamic re-organization of hyaluronan-rich matrices — from tissues to supramolecular models in experiment and theory

Dissertation presented to the Department of Biochemistry and Molecular Biology to obtain the degree of Doctor from the University of Basque Country

Xinyue Chen

2016

Thesis supervisor: Dr. Ralf P. Richter

University tutor: Prof. Felix Goñi Urcelay

eman ta zabal zazu

Universidad del País Vasco
Euskal Herriko Unibertsitatea
The University of the Basque Country

Physical principles underlying structure, mechanics and dynamic re-organization of hyaluronan-rich matrices — from tissues to supramolecular models in experiment and theory

Dissertation presented to the Department of Biochemistry and Molecular Biology to obtain the degree of Doctor from the University of Basque Country

Xinyue Chen

Thesis supervisor: Dr. Ralf P. Richter

University tutor: Prof. Felix Goñi Urcelay

Donostia-San Sebastian 2016

The research work related to this thesis has been performed at:

CIC biomaGUNE

Donostia-San Sebastian,

Spain

Max-Planck-Institute for Intelligent Systems

Stuttgart,

Germany

Success is the ability to go from one failure to another with no loss of enthusiasm.

Sir Winston Churchill

Acknowledgement

This thesis work would not have been accomplished without the generous support from many people around me. To only some of them it is possible to give particular mention here.

First and foremost, I would like to express my sincere gratitude to Dr. Ralf Richter, who served as my supervisor and continuously piloted my professional life in the past four years. I do greatly appreciate he offered me the opportunity to commence my PhD in his group with only curiosity and passion but not proper knowledge background. He brought me to this new scientific field and guided me to achieve every progressive step in the exploring journey with his extraordinary patience. I am grateful to have his support on all scientific aspects, throughout research idea exchanges, technical instructions and guidance of writing. As a brilliant principle investigator, his scientific criticism, broad and deep knowledge background and perfect organization will be a benchmark in my future professional career steps. Thank you Ralf, I will always remember and cherish everything learned from you.

My gratitude also goes to the collaborators, in particular Dr. Oleg Borisov and Prof. Antonietta Salustri. They are experts in their scientific fields and contributed to this interdisciplinary project as best as they could. Without their support in theory development and biological sample preparation, the work in this thesis would not be completed. It was also a great fun to have fruitful discussions with them. Appreciate a lot for your kindness.

I would like to thank all my former and current colleagues in the group, for both valuable scientific interactions and wonderful time outside the lab. Special gratitude goes to Dr. Natalia Baranova for guidance during my initial days in the lab and all the rest fantastic communications, Dr. Raphael Zahn for great co-working experience, and Dr. Leire Diaz for helping me to settle down in Spain and all the translations. Thank you all for your friendly support in different ways.

My gratitude is extended to many other people in CIC biomaGUNE, throughout other research groups, platform managers, administrative and maintenance staff. Their support on different aspects provided me better working experience. Also thanks the administrative staff in Max Planck Institute for Intelligent Systems and the University of Basque Country for helping me on necessary paper work.

I am also grateful to all sisters and girls in Residencia ¨El Carmelo¨. Their care and kindness helped me to quickly settle down in a city that I was completely unfamiliar with, and encouraged me throughout the past four years. Thank you very much for providing me the home-feeling in Donosti.

My special gratitude goes to Prof. Udo Seifert. Thanks a lot for your enlightenments of how to better understand knowledge and structure my career. On top of this, thank you for all the encouragements when I faced difficulties or confusions.

I would also like to express my particular thankfulness to Prof. Dave Fernig, for opening the door of science for me, for fruitful and inspiring discussions, for caring and supporting my progress. Thank you very much for all your contributions to my professional development.

Last but certainly not the least, I appreciate my parents for their unconditional love. They always fully supported my decision of how to develop my career, even though sometimes it was tough for them. Thank you very much for your enormous contributions in every phase of my life.

Thanks all the people participated in this journey.

Abstract

The extracellular matrix (ECM) is the acellular structure of all tissues and essential for multicellular life. Next to biochemical signals, the physical properties of the ECM provide important signals to cells. The polysaccharide hyaluronan (HA) is ubiquitous in the extracellular space of vertebrates and an important structural component of the ECM. HA is a linear, unbranched and regular polymer of the glycosaminoglycan (GAG) family, and serves as a scaffold that responds dynamically to molecular stimuli such as HA-binding proteins, or changes in pH or ionic strength. The objective of this PhD research project was to elucidate physical principles underlying the structure, mechanics and dynamic re-organization of HA-rich matrices. To address this question, we have studied the mechanical properties and morphology of HA-rich matrices at distinct levels of complexity. On one hand, we have studied the cumulus cell-oocyte complex (COC) matrix as an example of complex, native HA-rich tissue. On the other hand, we have studied so-called HA brushes as a well-defined *in vitro* reconstituted model of HA-rich matrices.

The HA-rich matrix in the COC forms around oocytes just before ovulation and plays vital roles in oocyte biology. We have analyzed the micromechanical response of mouse COC matrix by colloidal probe atomic force microscopy (AFM). We found the COC matrix to be extremely soft yet elastic, suggesting a stable gel-like network structure with high porosity and a large mesh size. With a Young's modulus around 1 Pa, COC matrices are among the softest elastic biological materials known to date. In addition, the elastic modulus increased progressively with indentation. Furthermore, using optical microscopy to correlate these mechanical properties with ultra-structure, we discovered that the COC is surrounded by a thick matrix shell that is essentially devoid of cumulus cells. We propose that the pronounced non-linear elastic behaviour of COC matrix is a consequence of structural heterogeneity and serves important functions in biological processes, such as oocyte transport in the oviduct and sperm penetration.

To understand more comprehensively the response of HA polymers to changes in their aqueous environment, the thickness and viscoelastic properties of films of end-grafted HA (also called HA brushes) as a well defined *in vitro* model of HA-rich matrices were characterized by reflection interference contrast microscopy (RICM) and quartz crystal microbalance with dissipation monitoring (QCM-D) as a function of Ca^{2+}

concentration and pH. Within the physiological range, the thickness of HA brushes decreased significantly with Ca^{2+} concentration but did not change with pH. By screening a large range of Ca^{2+} concentrations, we discovered that the effect of Ca^{2+} on HA brush thickness is virtually identical to the effect of Na^+ at 10-fold higher concentrations. HA brushes responded only weakly to pH changes above pH 6.0, but showed a sharp collapse around pH 3. Our results provide insights into how HA matrices are affected by solution properties, which is relevant in biological systems and for the design of synthetic tissues.

Finally, using theoretical computations based on self-consistent mean field theory, we elucidated how the morphology of polymer brushes is influenced by the formation of physical cross-links between polymers, such as they would occur in the presence of cross-linking proteins. We find that cross-links promote a denser and more homogeneous brush morphology. The effect of cross-links is comparable to the effect of reduced solvent quality when the density of cross-links is low, but unique features including the retention of solvent even with strong cross-links emerge at high cross-linking densities.

This work provides novel insights into how the supramolecular structure and thus the mechanical properties of HA-rich matrices can be dynamically regulated by changes in microenvironmental conditions. This can be linked to different biological functions of native HA-rich extracellular matrices but is also of interest for the design of tailored, synthetic HA-based materials for applications in tissue engineering.

Table of contents

Resumen

Las células en organismos multicelulares se mantienen unidas por un componente acelular que las envuelve llamado matriz extracelular (MEC). La MEC está presente en todos los tejidos y órganos y juega diversas funciones en los sistemas bilógicos (1-3). Además de ser un andamiaje celular esencial para las células (4), la MEC también funciona como un sustrato adhesivo para la migración celular (5, 6). También puede proporcionar señales bioquímicas interpretadas por receptores de la superficie celular (7), e iniciar, así, una cascada de señales a través de la mediación de múltiples comportamientos celulares (8).

La MEC está compuesta por una variedad de proteínas y polisacáridos que son secretados de forma local por las células (1, 2). Los tipos y cantidades relativas de las macromoléculas de la matriz, y la manera en la que están organizadas en la MEC, varía entre los distintos tejidos, y de esta manera, la MEC se adapta a las necesidades funcionales específicas de cada tejido. La MEC madura sufre continuas modificaciones en respuesta a estimulos del entorno (9, 10). Es importante regular de forma precisa la estructura dinámica de la MEC para diversos procesos fisiológicos.

El ácido hialurónico (HA) es uno de los principales componentes y ubicuo en el espacio extracelular de los vertebrados. Es un polisacárido linear, no ramificado compuesto por unidades de disacáridos idénticos que contienen ácido glucurónico y N-acetilglucosamina, unidos a través de enlaces glicosídicos β-1,4 y β-1,3 (11, 12). Cada disacárido, que tiene una longitud de 1.0 nm (13) y tiene un peso molecular de 400 Da, tiene un grupo carboxílico que se puede cargar. La pKa del HA polimérico es aproximadamente 3 (14), y HA tiene, en consecuencia, carga negativa en condiciones de pH fisiológico. La morfología de un polímero libre de HA en solución acuosa se puede describir como una madeja aleatoria endurecida, es decir, un ensamblaje

altamente dinámico de estados intercambiables estocásticamente (15), donde la longitud persistente del HA se determinó en estar entre 4 y 14 nm (13, 16, 17).

Como miembro de la familia de los glicosaminoglicanos (GAG), el HA se diferencia de otros GAGs en varios aspectos. A diferencia de otros GAGs, el HA no contiene azúcares sulfatados. También, es un gigante comparado con otros GAGs. La masa molecular del HA alcanza a menudo los millones de Dalton (11) de manera que la longitud de contorno puede ser de hasta varios micrómetros. Mientras que el resto de GAGs se sintetizan dentro de la célula, en el aparato de Golgi, y se liberan por exocitosis, el HA es sintetizado por sintasas de HA (HASs) que residen en la membrana plasmática (18).

La conformación y las propiedades fisicoquímicas del HA, que sostiene sus roles funcionales, dependen de su peso molecular (19) y también se ven afectadas por las condiciones ambientales locales, como la fuerza iónica (20, 21) y los estímulos mecánicos (22), además de la interacción con otros componentes de la MEC, incluídos los receptores de la superficie celular (23-25) y otros componentes del espacio intersticial (26-30). HA recién sintetizado puede ser tanto liberado en disolución/la MEC, como permanecer injertado a la superficie celular a través de sus sintasas (18) y/o si no permanecer fijado a través de diversos receptores de la superficie celular (23-25) para formar lo que se conoce como capa pericelular (PCC) que es crucial para funciones celulares básicas, como la proliferación y migración (31), y también para regular la adhesión entre células (32). Como sub-grupo de proteínas HA-ligantes (también llamadas hialadherinas), proteoglicanos como agrecano y versicano, se pueden ensamblar dentro de la MEC al estar ligados al HA a través de proteínas de unión (33-35) formando grandes complejos. Debido a sus particulares propiedades fisicoquímicas y su fuerte hidratación, éstos complejos ricos en HA pueden actuar como relleno de

espacio y/o lubricantes (34). El HA también se puede reticular al interactuar con otras hialadherinas como TSG-6 (26), cuya influencia en el ensamblaje y propiedades de las matrices ricas en HA ha sido identificada (36). Éstos complejos ricos en HA también se conocen por ser claves en procesos fisiológicos y patológicos, como desarrollo embrionario (37, 38), inflamación (36) y desarollo tumoral (39, 40).

Está probado que las propiedades mecánicas de la MEC tienen un gran efecto en las células a las que rodean. Las células pueden sentir las propiedades mecánicas de la MEC que las rodea aplicándole fuerzas y midiendo el feedback resultante (41). Se ha confirmado que ésta capacidad facilita muchos procesos celulares importantes, incluyendo contracción celular (42), proliferación celular (43), migración (44, 45), diferenciación (46) y muerte celular (apóptosis) (47), además de patologías como progresión tumoral (40, 48). En particular, la importancia funcional de las propiedades mecánicas de la MEC rica en HA se identificó claramente en décadas anteriores en matrices ricas en HA tanto nativas como sintéticas. Debido a estudios relevantes sobre cartílagos, se sabe que las matrices ricas en HA son esenciales para resistir la compresión y que actúan como lubricantes (49, 50). Además, las propiedades mecánicas bien afinadas de la matriz del cumulus oophorus (COC), una MEC rica en HA que rodea los oocitos en el folículo ovárico y en su viaje en el oviducto, son críticas para el transporte del ovocito (51). Entretanto, las propiedades mecánicas bien reguladas de las matrices reticuladas de HA reconstituídas *in vitro* demostraron ser importantes para la adhesión celular y la propagación en aplicaciones de bioingeniería (52).

En contraste a la reconocida importancia funcional, los principios (en particular de aspecto físico) subyacentes a las características clave y consecuentemente las funciones de las MEC ricas en HA siguen sin clarificarse. Por lo tanto, el objetivo de esta tésis es elucidar las principios físicos que subyacen la estructura, mecánica y dinámica de

reorganización de las matrices ricas en HA, y así llenar el espacio entre las características moleculares bien conocidas de matrices ricas en HA y las funciones de las complejas MEC ricas en HA nativas. Con este fin, hemos llevado a cabo un estudio sistemático que cubre los diferentes niveles de complejidad de la matriz, y usa métodos experimentales y teóricos.

El estudio comienza con tejido nativo, donde utilizamos la matriz de COC como ejemplo. Las matriz del COC es una capa extensa que se forma alrededor del ovocito unas horas antes de la ovulación y juega un papel vital en la biología del ovocito (53). El HA es el andamiaje principal de la matriz del COC y carece de otras proteínas estructurales de la matriz (por ejemplo colágeno, fibronectina), y, por lo tanto, esta matriz es de particular interés en esta tesis. Las propiedades micromecánicas de la matriz del COC se caracterizaron de forma cuantitativa por microscopía de fuerza atómica (AFM), y revelamos más información sobre la ultra estructura de la COC por combinación de AFM y microscopía óptica (ver **Chapter II**). Las caracterizaciones micromecánicas indican que la matriz del COC es extremadamente blanda pero elástica, y mecánicamente heterogénea. Además, se ha encontrado una capa externa gruesa libre de cumulus que nunca había sido reportada. Tal caracterización revela propiedades prominentes del tejido nativo, pero no son suficientes para resolver los principios físicos que subyacen a éstas propiedades debido a la compleja organización de los tejidos nativos.

Para analizar la auto-organización del HA como el principal componente de la matriz, hemos estudiado un modelo *in vitro* simplificado de la matriz. El modelo elegido son películas de polímeros de HA injertados por un extremo a una superficie sólida (es decir, cepillos de HA). Las cadenas de HA injertadas por un extremo imitan a las cadenas de HA fijadas a la superficie celular, tal como ocurriría en células del

cumulus u otras células que tienen capas pericelulares extensas. En esta tesis, determinamos las propiedades estructurales (es decir, grosor del cepillo) y mecánicas (es decir, la viscoelesticidad) de dichos cepillos de HA valiéndonos de microscopía de contraste de la interferencia de reflexión (RICM) y microbalanza de cristal de cuarzo con monitorización de la disipación (QCM-D), respectivamente, concentrándonos en el efecto de la concentración del calcio o del pH (ver **Chapter III**). Estos estudios han revelado que las propiedades morfológicas y mecánicas del cepillo son sensibles a la concentración de calcio y estables con el pH dentro del rango fisiológico. Al cubrir un amplio rango de concentraciones de Ca^{2+}, descubrimos que el efecto del Ca^{2+} en los cepillos de HA es prácticamente igual al efecto del Na^+ en concentraciones mayores por un factor de 10, y que los cepillos se colapsan con una protonación por debajo de pH 6.0. Esto nos acerca a la resolución de los principios físicos que subyacen a estas propiedades.

Las características clave de las matrices ricas en HA están básicamente determinadas por las propiedades de moléculas que las constituyen y sus interacciones, y por lo tanto es rentable vincular las observaciones de ensamblajes supramoleculares como el cepillo de HA a características de moléculas individuales. El estudio de la estructura y dinámica de cadenas de polímeros de HA individuales sigue siendo desafiante en el contexto de los cepillos de HA y de las matrices del COC. Por lo tanto, accedemos a los principios clave que vinculan moléculas individuales y ensamblajes supramoleculares a través de un método alternativo: teoría física de polímeros. En esta tesis, nos concentramos en el efecto de la reticulación (reversible) física sobre la morfología de cepillos poliméricos, y analizamos este caso utilizando la teoría de campo medio (ver **Chapter IV**). La teoría predice que la compactación y cambios en el perfil de densidad de un cepillo polimérico debido a la reticulación es equivalente a la reducción en volumen excluído cuando hay

poca reticulación, mientras que un comportamiento cualitativamente nuevo surge para cuando aumenta la reticulación. Para probar esta teoría, la contrastamos con datos experimentales de la barrera del poro nuclear (otro ensamblaje biológico que consiste en cadenas poliméricas flexibles) de los que disponemos en el laboratorio. La correlación con los datos experimentales en cepillos regulares de dominios de neo-FG no sólo provee valores importantes a los que no tenemos acceso experimentalmente, como la fuerza de interacción de reticulaciones individuales, sino también demuestra la aplicabilidad de la teoría. De este modo, damos luz a los mecanismos que conectan la compleja organización y las propiedades fisico-químicas a las propiedades de las moléculas individuales de los biopolímeros.

En resumen, hemos caracterizado las características estructurales y mecánicas prominentes de las MEC ricas en HA y de las matrices de HA recosntituídas *in vitro* en determinadas condiciones. Teoricamente, las caracteristicas de los ensamblajes supramoleculares se correlacionan con las caracteristicas individuales de las moleculas. Los estudios sistematicos en esta tesis revelan el principio fisico de interes, y pueden ser extendidos con la mejora de las tecnicas/modelos/teoria, asi como ser integrados con el conocimiento sobre el espacio intracellular o pistas bioquimicas.

Abbreviations

8-Br-cAMP	8-bromoadenosine 3',5'-cyclic monophosphate
AC	Alternating current
ADAMTS-1	A disintegrin and metalloproteinase with thrombospondin motifs 1
AFM	Atomic force microscopy
Au	Gold
BSA	Bovine serum albumin
CD44	CD44 antigen
COC	Cumulus cell-oocyte complex
COMP	Cartilage oligomeric matrix protein
CS	Chondroitin sulphate
DS	Dermatan sulphate
ECM	Extracellular matrix
FG	Phenylalanine-glycine
FSH	Follicle-stimulating hormone
GAG	Glycosaminoglycan
Gal	Galactose
GalNAc	N-acetylgalactosamine
GlcA	Glucuronic acid
GlcNAc	N-acetylglucosamine
HA	Hyaluronan
HAS	Hyaluronan synthase
HC	Heavy chain
hCG	Human chorionic gonadotropin
HER2	Human epidermal growth factor receptor 2
HS	Heparan sulphate
IdoA	Iduronic acid
IVF	*In vitro* fertilization
IVM	*In vitro* maturation
IαI	Inter-alpha-inhibitor
KS	Keratan sulfate
LH	Luteinizing hormone
NPC	Nuclear pore complex

NTR	Nuclear transport receptor
OEG	Oligo-ethylene glycol
PCC	Pericellular coat
PE	Polyelectrolyte
PG	Proteoglycan
PI3K	Phosphatidylinositol 3-kinase
PMSG	Pregnant mares' serum gonadotropin
PTX3	Pentraxin 3
QCM-D	Quartz crystal microbalance with dissipation monitoring
RHAMM	Receptor for HA-mediated motility
RICM	Reflection interference contrast microscopy
SAM	Self-assembled monolayer
SAv	Streptavidin
SCFT	Self-consistent field theory
SE	Spectroscopic ellipsometry
SLB	Supported lipid bilayer
SUV	Small unilamellar lipid vesicles
TSG-6	Tumor necrosis factor-inducible gene 6 protein
UDP	Uridine diphosphate

Objective and outline

Tissues are not made up solely of cells, but also an intricate network of macromolecules between cells constituting the so-called extracellular matrix (ECM). The ECM is composed of a variety of proteins and polysaccharides that are secreted locally by cells (2). It provides not only essential physical scaffolding for cells but also crucial biochemical and biomechanical cues that are required for tissue morphogenesis, differentiation and homeostasis (1). The types and relative amounts of matrix macromolecules and the way they are organized in the ECM vary to a great extent across different tissues, and in this way, the ECM adapts to the tissue-specific functional requirements (1, 2).

Hyaluronan (HA) is one of the chief components of the ECM and ubiquitous in the extracellular space of vertebrates. It is a linear, unbranched polysaccharide composed of identical disaccharide units. As the simplest member of the glycosaminoglycan (GAG) family, HA differs from other GAGs in many aspects, such as sugar sulfation degree, molecular mass and its biosynthesis (18). The uniformity of molecular structure never blocks HA from playing various biological roles in the ECM. The conformation and physicochemical properties of HA, which support its functional roles, are dependent on its molecular weight (19) and also affected by the local environmental conditions, such as ionic strength (20, 21) and mechanical stimuli (22). HA can also form more complex supramolecular structures by interactions with other ECM components including cell surface receptors (23-25) and other components from the inter-cellular space (26-30). Such HA-rich supramolecular assemblies have been known to play key roles in physiological and pathological processes, including embryonic development (37, 38), inflammation (36) and tumour development (39, 40).

In particular, the functional importance of the mechanical properties of HA-rich assemblies was clearly identified in the last decades on both native and reconstituted HA-rich matrices. For instance, HA-rich matrices were found to be essential for resistance to compression and act as lubricant in cartilage (49, 50), as well as involved in oocyte transport (51) and cellular mechanotransduction (54). The mechanical properties of artificial HA gels were also shown to be an important regulator for cellular adhesion and spreading in bioengineering applications (52).

9

While the functional importance of the physical properties of HA-rich matrices is well established, the molecular and physical mechanisms that define the physical properties are less well understood and thus are the main interests in this thesis. Therefore, the objective of this PhD thesis is to identify the principles, in particular physical principles that underlie the structure, mechanics and dynamic re-organization of HA-rich matrices. To address this question, a systematic study of the structural and mechanical properties of HA-rich matrices was performed, which covered distinct levels of matrix complexity and used both experiment and theory.

Outline

The biological context and the methodology relevant to this research project are introduced in **Chapter I**. On the biological side, this includes a presentation of extracellular matrices, and hyaluronan as a key component, and in particular their crucial role from a mechanics point of view. With regard to methodology, relevant methods for the biofunctionalization of surfaces, and for the biophysical characterization of soft films and tissues will be covered.

The scientific results of this research project are presented in **Chapters II** to **IV**. These chapters are presented in the format of scientific articles. A detailed description of the specific biological context and methods used is also covered in each chapter.

An archetypical example of HA-rich ECM is the cumulus cell-oocyte complex (COC) matrix, and extended coat that forms around oocytes before ovulation and plays vital roles in oocyte biology (53). Very limited information about the mechanical properties of COC matrices has been available. **Chapter II** presents a quantitative analysis by colloidal probe atomic force microscopy (AFM) combined with optical microscopy of the micromechanical properties and ultra-structure of COC matrices.

Chapter III presents the physical characterization, by a combination of acousto-mechanical and optical techniques, of the effect of ions and pH on films of end-grafted HA polymers. Such 'HA brushes' represent a simplified *in vitro* model of HA-rich matrices. Because these are well-defined, it becomes possible to elucidate how the molecular features of HA polymer chains and its confinement define the physico-chemical properties of HA-rich materials.

The morphology of HA brushes is not only affected by ions and pH, but some HA-binding proteins are known to physically cross-link HA. We applied self-consistent mean field theory in an effort to understand the consequences of cross-linking on

polymer brush morphology, and this is described in **Chapter IV**. The insights gained are of relevance for polymer brushes in general, and we illustrate this by applying the theory to analyze well-defined experimental models of another biological material, the nuclear pore permeability barrier which gates selective macromolecular transport into the cell nucleus.

Last but not least, **Chapter V** summarizes the main findings and significance of this research project, and indicates potential future developments.

I   Introduction

I.1   BIOLOGICAL CONTEXT

I.1.1   ECM

I.1.1.i   Definition and functions

In multi-cellular organisms, cells are held together by the surrounding acellular component called the extracellular matrix (ECM). The ECM is present within all tissues and organs and plays various roles in biological systems (1-3). Apart from being an essential physical scaffold for the cells (4), the ECM also serves as an adhesive substrate for cell migration (5, 6). It can also provide biochemical cues interpreted by cell surface receptors, such as the integrins (7), and thus initiate signalling cascades mediating multiple cell behaviours (8). These diverse functions are supported by the complex composition and organization of the ECM.

I.1.1.ii   Main components and self-organization

The ECM is composed of a variety of proteins (*e.g.* structural proteins including collagen, elastin, fibronectin, laminin and signalling proteins such as chemokines and growth factors) and polysaccharides of the glycosaminoglycan (GAG) family, which are secreted locally by cells residing in the matrix and assembled into organized networks (1, 2). The ECMs of each tissue possess unique compositions, ultrastructure and physical properties that are first defined at early embryonic stages (1, 9) and markedly heterogeneous (1). For instance, the main matrix molecule of interest for this thesis, hyaluronan (HA), exists in both the coating around ovulated oocytes (the cumulus cell-oocyte complex (COC) matrix) and in cartilage. However, the compositions of these two types of matrices differ appreciably (as shown in Figure I.1). Consequently, these matrices are responsible for different biological functions. The precise organization of the ECM is crucial for maintaining normal biological functions (1, 2).

The ECM is not a static entity. The mature ECM undergoes continuous remodelling in response to environmental stimuli to control tissue homeostasis (9, 10). The remodelling of the ECM is mediated either enzymatically or non-enzymatically (8-10), and is important for various physiological processes (*e.g.* in response to injury). Mis-regulation of the dynamic ECM structure may lead to pathologies (55, 56).
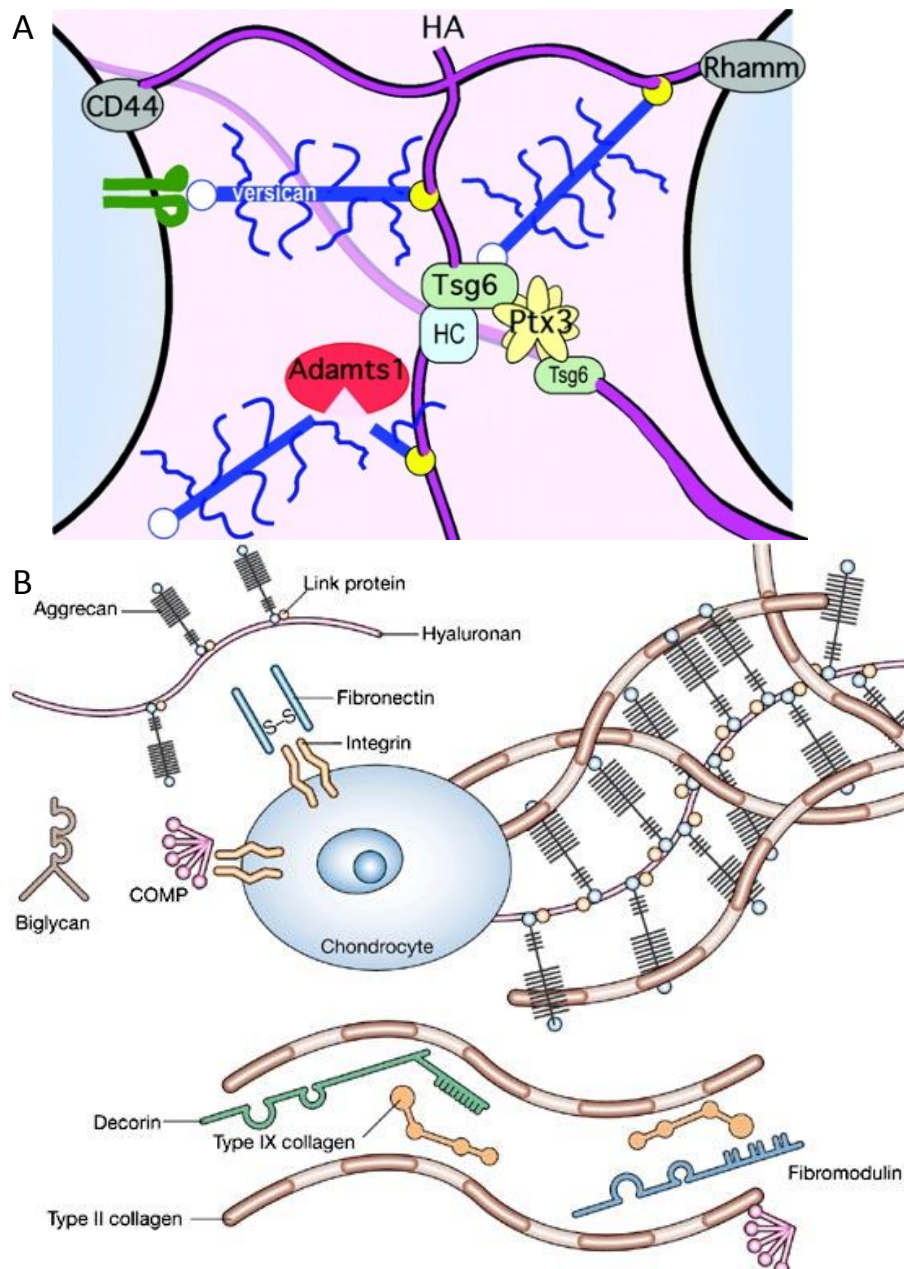
Figure I.1 Composition of the ECM in different tissues. (A) Molecular structure of the expanded COC matrix. HA is attached to cumulus cell surface via receptors (*e.g.* CD44 and/or Rhamm). The TSG-6/IαI heavy chains (HC)/PTX3 cross-link stabilizes the HA matrix. Versican interacts with both HA and cell surface proteins and may further anchor the HA matrix to cumulus cells, or gets cleaved by the protease ADAMTS-1 that possibly modulates the COC matrix structure during ovulation. Image taken from ref. (57). (B) Components of cartilage ECM. The matrix also contains HA but HA here is normally densely coated with aggrecan and link proteins. There are also other important components, such as collagen (mostly type II collagen), non-collagenous proteins like fibronectin and cartilage oligomeric matrix protein (COMP), as well as other smaller

proteoglycans (*e.g.* biglycan, decorin and fibromodulin). The interaction between highly negatively charged cartilage proteoglycans and type II collagen fibrils is essential for the tissue resisting load *in vivo*. Image taken from ref. (58).

I.1.1.iii   GAGs

GAGs are a group of long unbranched polysaccharides ubiquitously present on the cell surface (glycocalyx) and in the ECM. GAGs are formed by multiple disaccharide units, where each unit consists of an amino sugar (N-acetylglucosamine (GlcNAc) or N-acetylgalactosamine (GalNAc)) along with an uronic sugar (iduronic acid (IdoA) or glucuronic acid (GlcA)) or galactose (Gal) (Figure I.2) (59). Each monosaccharide is possibly sulfated at different positions (Figure I.2). GAG synthesis is not template driven (as for proteins or nucleic acids), and GAGs are instead dynamically formed and modulated by processing enzymes (60), GAGs have high diversity with regards to molecular mass (chain lengths can range from a few to a few thousand of disaccharide units), sulfation (different sulfated positions, such as N- and O-sulfations, as well as varied sulfation degrees along a chain can be found) and saccharide configuration (epimerizations and varied linkages) (59). According to these diverse structural features, GAGs can be classified into four main groups, known as chondroitin sulphate (CS) /dermatan sulphate (DS), heparin/heparan sulphate (HS), keratan sulfate (KS) and hyaluronan (HA) (Figure I.2) (59).

Complex supramolecular structures formed by interactions of GAGs with other ECM components are essential for the general architecture and functions of the ECM. GAGs (except HA) are usually attached covalently to core proteins through their reducing end and form proteoglycans (PGs) (59, 61-63). These PGs can aggregate into larger complexes. One typical example is the aggrecan-HA complex in cartilage. Aggrecans are non-covalently linked to a high molecular weight HA polymer through link proteins (Figure I.1*B*) (59, 61). Other complex supramolecular structures arise from binding of GAGs to structural proteins (64, 65) or from crosslinking of GAGs by ECM proteins (26, 36), such as the HA network in the COC matrix described in Figure I.1*A* (57).
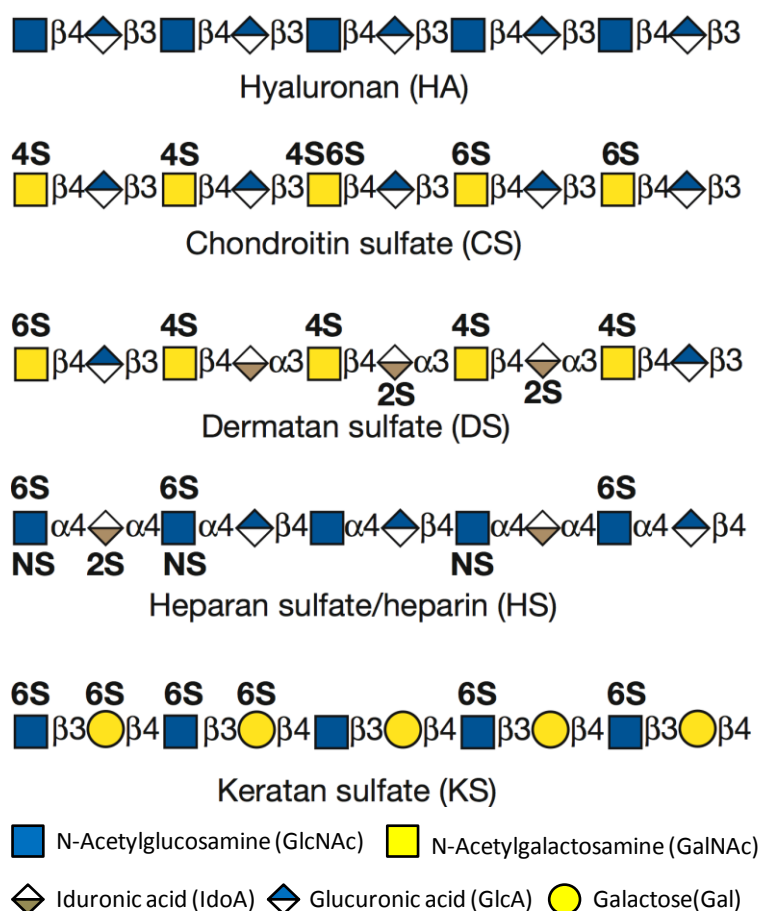
Figure I.2 Schematic of saccharide units in the different types of GAGs. Each saccharide unit is connected by α- or β-glycosidic bonds *via* position 3 or 4 of the saccharide. RS (R = 2, 4, 6 or N) represents O-sulfation at different positions (2, 4 or 6) of the saccharide or N-sulfation. Image modified from ref. (59).

I.1.2   Hyaluronan

In this thesis, the main molecule of interest is HA. As one of the chief components of the ECM, HA is ubiquitous in the extracellular space of vertebrates and plays a variety of biological roles. It is exceptional in the GAG family, differing from the other members in structure, biosynthesis and biological functions.

I.1.2.i   Structure and physicochemical properties

HA is often also called as hyaluronic acid, though the molecule is typically used together with counterions and thus is a salt rather than an acid. It was discovered in 1934 by Karl Meyer (66) yet its structure was only determined almost 20 years later (67). HA is a linear, unbranched polysaccharide composed of identical disaccharide units containing glucuronic acid and N-acetylglucosamine, linked together via β-1,4 and β-1,3 glycosidic bonds (Figure I.3) (11, 12). Unlike other GAGs, HA contains no

16

sulfated sugars. Each disaccharide, which is 1.0 nm long (13) and has a molecular weight of 401 Da, carries one chargeable carboxylic group. HA is a giant compared to other GAG members. Its molecular mass reaches up to a few million Dalton (11) so that its contour length (*i.e.* the length of the molecule when it is fully stretched) can be up to several micrometers. The pK_a of polymeric HA is approximately 3 (14), and HA is thus negatively charged at physiological pH.
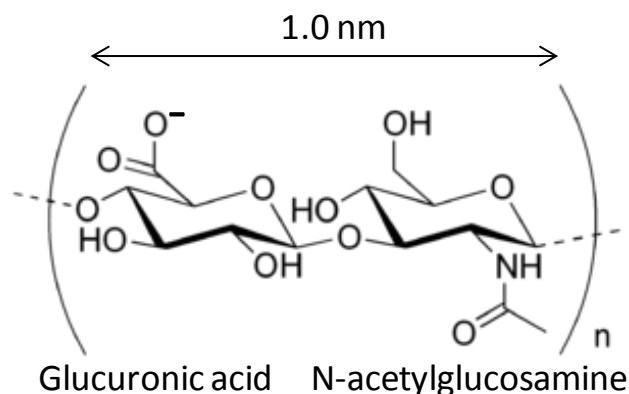
Figure I.3 Chemical formula of HA, without its counterions. The number of repeat disaccharide units *n* varies and can reach 10^4 or more.

The morphology of HA was described as a stiffened random coil occupying a large volume (68). Hydrogen bonding between adjacent monosaccharides combined with the effect of mutual electrostatic repulsion between carboxyl groups were proposed as the explanation for the local stiffening of HA chains (13), while the persistence length of HA was predicted as approximately 14 nm by simulations (13) in contrast to 4 – 8 nm obtained from experimental data (16, 17). Subsequently, an argument appeared, which attributed the physicochemical properties of HA in solution mainly to the self-association of HA through hydrophobic patches (69, 70). However, data on the self-diffusion of HA and the properties of HA brushes (20) revealed that inter-chain associations are not responsible for HA solution properties (71, 72). The current view describes HA in aqueous solution with physiological pH and ionic strength as a well solvated polymer that forms a stiffened and highly dynamic ensemble of stochastically interchanging states (15).

The conformation and physicochemical properties of HA, which support its functional roles, are dependent on its molecular weight (19) and also affected by the local environmental conditions, such as ionic strength (20, 21) and mechanical stimuli

(22), as well as interaction with other ECM components including cell surface receptors (23-25) and other components from the inter-cellular space (26-30).

I.1.2.ii   Biosynthesis

The biosynthesis of HA is exceptional within the GAG family. Whereas all other GAGs are synthesized inside the cell in the Golgi apparatus and released by exocytosis (60, 61, 68), HA is synthesized by HA synthases (HASs) (18, 73) that reside in the plasma membrane (18, 74-76). Sugar units are added from nucleotide precursors to the chain on the cytoplasmic side of the membrane and simultaneously the chain is extruded through the membrane into the extracellular space (or to make the cell capsule in the case of bacteria) (11, 18). This mechanism allows unconstrained polymer growth, and thus accomplishes the exceptionally large size of HA, whereas confinement of synthesis within a Golgi or post-Golgi compartment could limit the overall amount or length of the polymers formed (18). On the other hand, it is known that different enzymes in HAS family can produce HA of varying molecular masses (77). How the size of synthesized HA is controlled is not well understood.

Moreover, the mechanism of HA synthesis was found distinctly different from that for other GAGs (78). All other members of the GAG family are elongated on core proteins by transferring an appropriate sugar from a sugar nucleotide onto the non-reducing terminus of a growing chain (79). In contrast, HA synthesis occurs at the reducing end of a growing HA chain. The two-site mechanism of HA synthesis was first proposed by Prehm (see Figure I.4) (78, 80). Two substrates, uridine diphosphate (UDP)-GlcA and UDP-GlcNAc, bind to two active sites within the enzyme. HA chains are elongated by alternate addition of their reducing end to the substrates on the other site with liberation of UDP. This synthesis mechanism is unusual and does not occur with other systems, such as the eukaryotic HS synthase (81) and the bacterial polysaccharide synthases (82), even though they utilize the same nucleotide sugar substrates.

---[-β-1,4-GlcA-β-1,3-GlcNAc-]$_n$-β-1,4-**GlcA-UDP** >>>> HAS Site 1

GlcNAc-UDP >>>> HAS Site 2

UDP ⟵

GlcA-UDP ⟶ >>>> HAS Site 1

---[-β-1,4-GlcA-β-1,3-GlcNAc-]$_n$-β-1,4-**GlcA**-β-1,3-***GlcNAc-UDP*** >>>> HAS Site 2
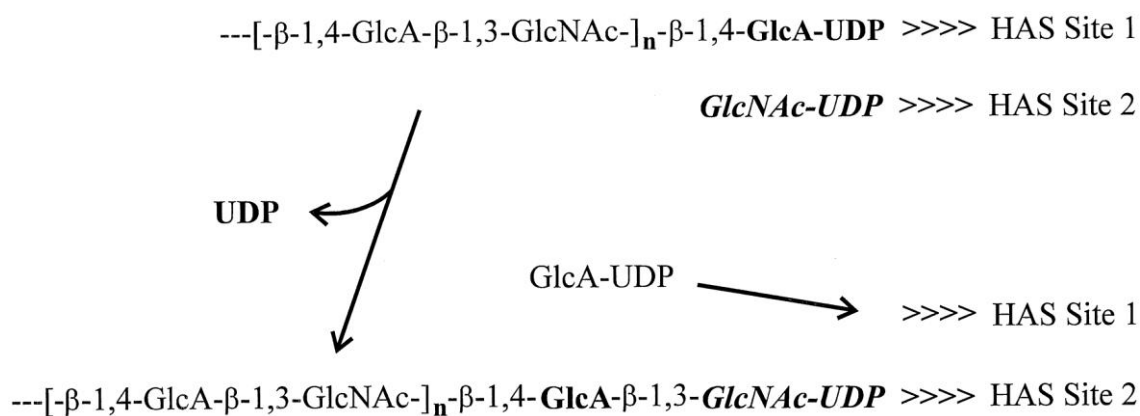
Figure I.4 Schematic of the two-site mechanism of HA synthesis. The reducing end sugar of the growing HA chain remains covalently bound to a UDP and attaches to one active site of the enzyme (HAS). The growing UDP-HA chain shuttles from one site to the other with the substrate during elongation, while its terminal UDP can be replaced by the substrate and attach a new UDP-sugar. Image taken from ref. (18).

I.1.2.iii   Roles in biological systems

HA is predominantly present in the ECM and interacts with a variety of ECM molecules. Newly synthesized HA can either be released into solution/the ECM, or stay grafted to the cell surface via its synthases (18) and/or otherwise attached via several cell surface receptors, such as CD44 (23, 25) and RHAMM (24, 25), to form so-called pericellular coats (PCCs). HA-rich PCCs are crucial for basic cellular functions, such as proliferation and migration (31), and also regulate adhesion between cells (32).

HA can form more complex supramolecular structures by interacting with HA-binding proteins (also called hyaladherins). As a sub-group of hyaladherins, proteoglycans like aggrecan and versican, can be assembled within the ECM by being linked to HA via link proteins (33-35) forming large complexes (as shown in Figure I.1). Due to its particular physicochemical properties and strong hydration, these HA-rich complexes can act as space filler and/or lubricant. For instance, the complexes formed by aggrecan and HA in cartilage provide load-bearing function in articular cartilage (34). HA can be cross-linked by interacting with other hyaladherins such as TSG-6, alone (26) or in complex with the proteoglycan IαI (27) and the protein PTX3 (83), which has been identified to influence the HA-rich matrix assembly and properties (36). These HA-rich complexes are also known to play key roles in physiological and pathological processes, including embryonic development (37, 38), inflammation (36) and tumour development (39, 40).

I.1.3   An example of HA-rich ECM — the COC matrix

An example of HA-rich ECM is the cumulus cell-oocyte complex (COC) matrix (Figure I.5). The COC matrix is devoid of other structural matrix proteins (*e.g.* collagen, fibronectin) and because HA is the main scaffold of the COC matrix, this matrix is of particular interest in this thesis.
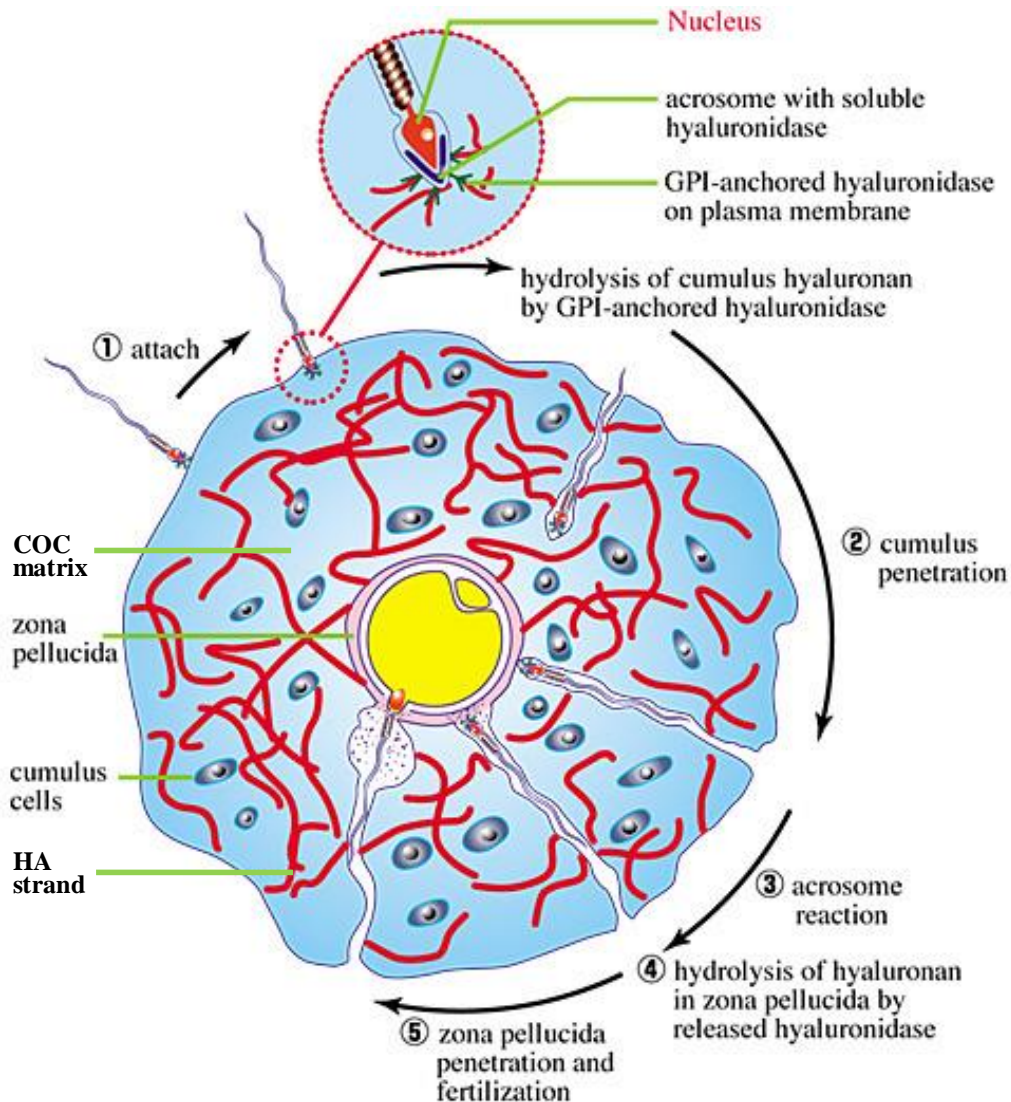
Figure I.5 Schematic of the COC matrix and sperm penetration process. Image modified from ref. (38).

I.1.3.i   Definition, expansion and function of COC matrix

Both in the ovarian follicle and after ovulation, the oocyte is surrounded by a distinct population of somatic cells known as the cumulus cells (53). In response to the ovulatory luteinizing hormone (LH) surge, the cumulus cells express proteins and HA that assemble into a unique matrix embedding the cumulus cells and enveloping the

oocyte. This process, known as the COC matrix expansion, is dependent on a cascade of intracellular signals inducing ECM gene expression (53). The main component of the COC matrix in all examined species is HA (53). Synthesis of HA is a fundamental process for COC matrix expansion. COC expansion can be induced *in vivo* after LH surge or by injection of human chorionic gonadotropin (hCG) to animals primed with pregnant mares' serum gonadotropin (PMSG) (Figure I.6) (84, 85). COC expansion can also be reproduced *in vitro* by culturing isolated COCs with follicle-stimulating hormone (FSH) (86). The enzyme that polymerizes HA chains in the COC is hyaluronan synthase type 2 (HAS2) (87-90). HA chains synthesized and released by HAS2 have extremely large size, with molecular masses larger than 2 MDa (91).
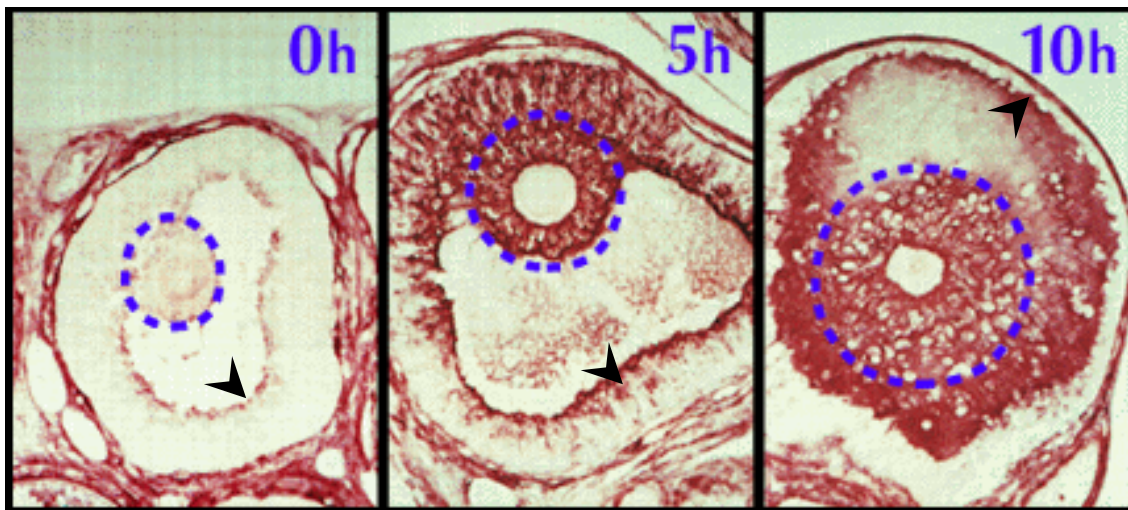
Figure I.6 HA synthesis during the COC expansion in mouse ovaries *in vivo*. HA was stained in red by a biotinylated HA-specific protein probe (92). Each frame presents individual follicles from ovaries that were isolated at times 0, 5 and 10 h after injection of an ovulatory dose of hCG. The COC is encircled by a dotted blue line. It is notable that HA synthetic activity is not exclusively localized to cumulus cells, but also occurs at the innermost layers of mural granulosa cells (85), as pointed out by black arrows. Image modified from ref. (38).

The synthesis of COC matrix and cumulus gene expression has been linked to oocyte quality (85, 93) and developmental capacity, and thus the degree of cumulus expansion has been used as a criterion for selection of oocytes for *in vitro* fertilization (IVF) for many years (94-96). The presence of the COC matrix has been found to reduce oxidative stress on the oocyte (97), and hence may protect the oocyte during the events of tissue hyperemia and inflammation that increase oxidative free radicals during

ovulation (53). Animal models with disrupted COC matrix expansion show entrapment of oocytes in luteinized follicles (98), and thus reveal that the matrix is crucial for oocyte release. The COC matrix is also known to facilitate the transport of COCs along the oviduct. Matrix-enclosed COCs are efficiently transported in the oviductal lumen (99, 100), whereas cumulus-denuded oocytes are not (101, 102). Moreover, fertilization is also likely dependent on the COC matrix, where sperm has to interact with the matrix before making contact with the oocyte (Figure I.5) (38, 53). Components of the COC matrix, such as PTX3 (83), were proposed to possibly act as an active sperm attractant (103) and contribute to capacitation of sperm (104). The COC matrix may also present a selective barrier that screens for sperm with high fertilization potential (105), and accelerates the human sperm acrosome reaction (106, 107).

I.1.3.ii   HA in the COC matrix

Visualization of the unperturbed COC matrix ultra-structure is challenging due to the low degree of order and strong hydration. Therefore, it is not surprising that the HA matrix ultrastrutures reported in some previous studies were found to be significantly affected by preparation artifact due to a large amount of shrinkage in the cumulus material (108). Ultra-structural analysis of the COC matrix based on improved freeze substitution provides more reliable matrix architecture and suggests that HA strands are organized in a mesh-like network in the matrix (109). Protease treatment was found to be able to disrupt the matrix stability, thus demonstrating that proteins are necessary to organize and retain the HA matrix (110).

The functional role(s) for HA in the COC is still an area of intense research. Some of the functional properties given by HA in other tissues are also considered to be important in the HA-rich COC matrix. For instance, the poly-anionic and locally stiff characteristic of HA promotes the highly hydrated conformation of the COC matrix (53). This hydrated matrix can act as a space filler and its viscoelastic properties allow the COC to deform and easily pass through the ruptured follicle wall and the oviduct. Moreover, by binding to cell surface receptors that are synthesized in parallel with HA by cumulus cells (89, 93, 111), HA contributes to mediate cell signalling pathways (53). As an example, binding between HA and CD44 receptor on the surface of tumour cells has been confirmed to transactivate the HER2 receptor (112), which in turn stimulates the PI3K-dependent signalling pathway (113, 114) that participates in controlling key properties and functions of cells such as growth, aging and malignant transformation

(115). Transactivation of the HER2 receptor by binding between HA and CD44 is likely also active in the COCs (53).

I.1.4   Importance of structure and mechanical properties of HA-rich ECM

It is now well established that the mechanical properties of ECM have profound effects on the cells that they surround. Cells can sense the mechanical properties of their environmental ECM by applying forces and measuring the resulting feedback (41). This has been confirmed to facilitate many important cellular processes including cellular contraction (42), cell proliferation (43), migration (44, 45), differentiation (46) and cell death (apoptosis) (47), in addition to pathologies such as tumour progression (40, 48). In particular, the functional importance of the mechanical properties of HA-rich ECM was clearly identified in the last decades on both native and reconstituted HA-rich matrices. Well known from cartilage, HA-rich matrices are essential for resistance to compression and act as lubricant (49, 50). Moreover, a stiffened COC matrix was found to impair oocyte transport (51). It was also confirmed that HA-rich matrices are involved in cellular mechanotransduction (54). Meanwhile, *in-vitro* reconstituted HA-rich matrices have become popular in the last decade in tissue engineering research (116-118). The mechanical properties of cross-linked HA gels, which can be very well regulated (119-121), were shown to be an important regulator for cellular adhesion and spreading in bioengineering applications (52).

While the functional importance of the physical properties of HA-rich matrices is well established, the molecular and physical mechanisms that define the physical properties are less well understood. To this end, it is essential to identify principles, in particular physical principles, that connect molecular and supramolecular structure with matrix mechanical properties and dynamic re-organization, and this is the main interest in this thesis.

Previous studies have provided a good quantitative characterization of key features, such as the average mechanical properties, at tissue or cellular level for some HA-rich matrices. For instance, studies on brain tissue (122) or bovine lung microvascular endothelial cells (123) indicated an elastic modulus on the order of 100 Pa in magnitude. Nevertheless, the composition of HA-rich ECMs varies dramatically between tissues and even within a given tissue over time (recall Figure I.1), and so will the mechanical and other physical properties. Measurements of one type of HA rich matrix will thus not

be representative for another HA rich matrix, and there is still a need to quantify the properties of native HA-rich ECMs. In this regard, the COC matrix is of particular interest in this thesis.

Moreover, it still remains challenging to understand the physical principles underlying matrix properties, assembly and reorganization, and thus, the mechanisms of function of HA-rich ECMs and in particular the role of HA within the matrix. Previous studies on the native matrices,such as the coat around chondrocyte (124) and the matrix in murine growth plate cartilage (125), have well presented quantitative information of the matrix properties at given conditions. However, these studies alone are insufficient to reveal the principles underlying matrix assembly and properties, because accessible parameter range is limited and the contributions of individual components within the matrix are hardly identified.

Studies on simplified artificial models enable key structural features, mechanical properties and the re-organization of HA-rich matrices to be quantified over a parameter range that is larger than in native ECMs, and the reduced number of components and controlled assembly conditions for model matrices also make it easier to reveal the physical principles underlying matrix assembly and physical properties.

Previous investigations on HA in solution and macroscopic hydrogels reported how the morphology and mechanical properties of HA-rich matrices can be affected by ions and pH (17, 21, 126-128), or cross-linking density (117, 118, 129). Although these studies provide by no means a complete description of the native biological system, they shed light on the principles underlying the structure, mechanical properties and re-organization of HA-rich matrices. More biologically relevant studies were previously performed based on a model composed of HA end-grafted to a solid surface. In these so-called HA brushes, the confinement of HA to the cell surface is reproduced and the effect of external cues can be readily quantified. In comparison with pure HA brushes under standard physiological buffer conditions (130), the environmental NaCl concentration (20) and introducing other ECM components such as aggrecan (29) were found to significantly affect brush morphology and mechanical properties. Proteins existing in the native ECM like TSG-6, alone and in complex with other proteins and proteoglycans, were also already shown to cross-link the HA brush and change brush morphology (26-28). HA brushes were used in this thesis work to study how other soluble cues, in particular divalent calcium ions and pH, influence HA matrix properties.

I.2   OBJECTIVE AND CONCEPTUAL APPROACH

The objective of this thesis was to elucidate physical principles that underlie the structure, mechanics and dynamic re-organization of HA-rich matrices. To this end, a systematic study was performed that covered distinct levels of matrix complexity, and used both experiment and theory. The conceptual approach is schematically illustrated in Figure I.7.
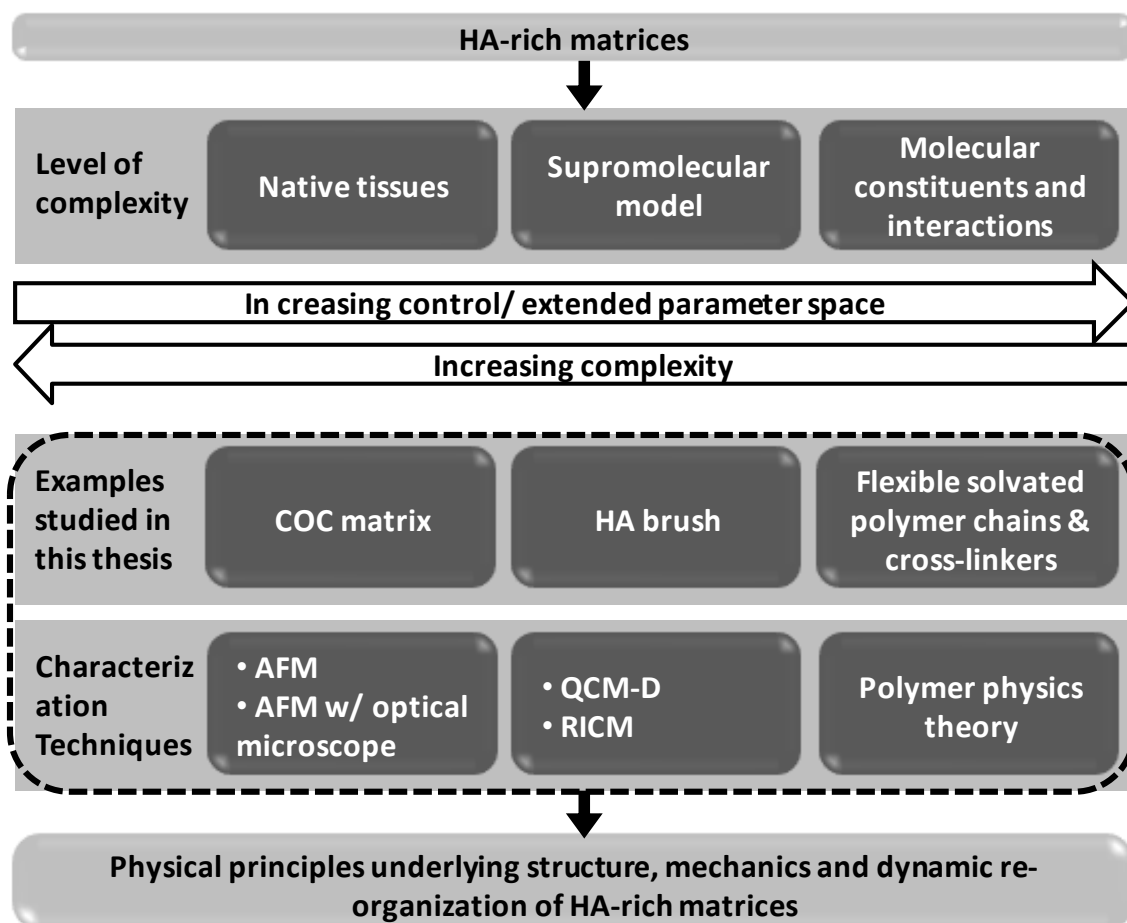
Figure I.7 Overview of the conceptual approach for and elements of the systematic study in this thesis.

The study commences with native tissue, where we use the COC matrix as example. The micromechanical properties of the COC matrix are quantitatively characterized by atomic force microscopy (AFM), and further information about the COC ultra-structure are revealed by combining AFM with optical microscopy (see **Chapter II**). Such a characterization reveals salient properties of the native tissue, but it is not enough to resolve the physical principles underlying these properties. This is due to the complex organization of native tissues. Because the native matrix consists of various molecules

at unknown concentration and distribution, it is difficult to define how individual components contribute.

To analyse the self-organization of HA as the major matrix component, we therefore study simplified *in vitro* models of matrix. The chosen models are films of HA polymers end-grafted to a solid surface (*i.e.* HA brushes). End-grafting mimics HA chains attached to the cell surface, such as it may occur on cumulus cells or other cells that have extended pericellular coats. In this thesis, the structural (*i.e.* brush thickness) and mechanical (*i.e.* visco-elastic) properties of such HA brushes are determined by reflection interference contrast microscopy (RICM) and quartz crystal microbalance with dissipation monitoring (QCM-D), respectively, with focus on the effect of calcium ions and pH (see **Chapter III**). Importantly, a parameter range can be covered that is not accessible with native matrix. Consequently, we can quantitatively study how individual parameters contribute to the structure, mechanics and dynamic re-organization of HA-rich matrices. This brings us a step closer to resolving the physical principles underlying these properties.

The key features of HA-rich matrices are ultimately determined by the properties of the constituent molecules and their interactions, and thus it is worthwhile to link the observations on supramolecular assemblies like the HA brush or the COC matrix to individual molecular features. The structure and dynamics of individual HA polymers remain very challenging to study in the context of HA brushes or COC matrices. However, the features of individual HA molecules (131) have been characterized in previous studies, and it is clear that the properties of HA as a flexible and solvated polymer chain must play an important role in defining matrix properties. Key principles linking individual molecules and supramolecular assemblies can be accessed by an alternative method: polymer physics theory. In this thesis, we focus on the effect of physical (reversible) crosslinks on the morphology of polymer brushes, and develop a mean field theory to analyse this case and test the new theory by confronting it with experimental data (see **Chapter IV**).

In the following section, the main methods used in this work are introduced in some detail.

I.3   METHODS

I.3.1   Surface functionalization and *in-vitro* model systems

I.3.1.i   Immobilization platform

An essential technique for the experimental work was the controlled deposition of molecules and tissues on surfaces.

An oligo ethylene glycol (OEG) monolayer deposited on gold (Au) substrates based on Au-thiol adsorption strategy developed in previous studies (132, 133), was adopted as solid support (Figure I.8). Although OEGs contain only hydrophilic ethylene glycol units (134), which is not same as the amphiphilic molecules (135) used for the well known self-assembled monolayers (SAMs), they can also form a robust and reproducible monolayer that passivates the Au surface and prevents non-specific adsorption of non-target molecules (136-138) or even cells (139). The resistance was hypothesized to be supported by the ability of OEG to bind large amounts of interfacial water (140). Through mixing two types of OEG molecules where one thiol was slightly longer in length compared to the other and possessed a biotin tag, the passivated solid substrate can be further functionalized with biotin-binding proteins for further functionalization purposes.

An intermediate monolayer of streptavidin (SAv) serves as a 'molecular breadboard' (141) for the anchorage of desired molecules (Figure I.8). Through strong and specific interactions between SAv and biotin exposed on the OEG monolayer, SAv can self-assemble into a well-organized monolayer (26, 132, 142-144). SAv is expected to be immobilized in such way that two of its four biotin-binding sites are facing the surface for locking with the biotin exposed in the OEG layer while the other two binding sites are facing the solution to accommodate target biotinylated molecules through a site-specifically attached biotin tag (Figure I.8). The orientation and grafting density of target molecules can be well controlled, which facilitates subsequent quantitative characterizations.
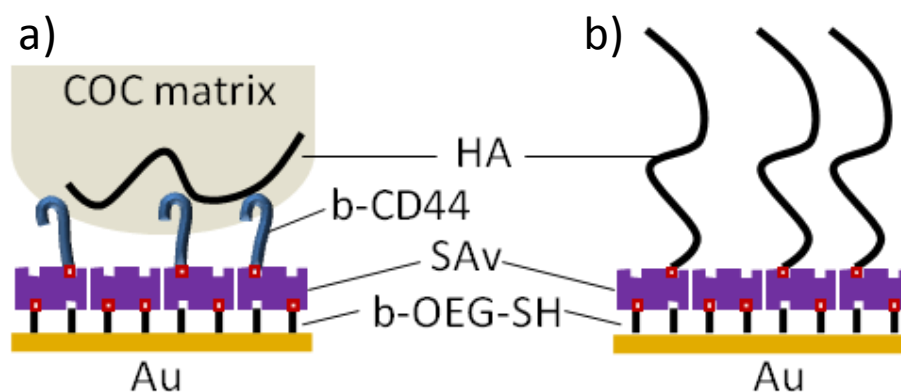
Figure I.8 Schematics of immobilization of the HA-rich COC matrix through CD44 monolayers (a) and design of the *in-vitro* HA brush model (b).

I.3.1.ii   Surface functionalization for immobilization of HA-rich tissues

The analysis of native tissues by techniques that probe mechanically such as AFM reveals the challenge of immobilizing the tissue firmly without excessive perturbation. In this thesis, this was necessary for the COC matrix. COCs did not adhere efficiently to plain glass or plastic substrates, and the specific interaction between CD44 and HA (23) was thus adopted for more stable immobilization. Hence, we needed to first immobilize CD44 on a solid support.

Ectodomains of the HA receptor CD44 were immobilized on the SAv layer *via* a biotin at CD44's carboxyl terminus (Figure I.8a). On this COC capturing substrate, the HA binding domain of CD44 is arranged in the same orientation as on the intact receptor in the cell membrane. In addition, optimizing the grafting density of CD44 provided rapid and efficient adhesion between the COC matrix and the substrate, while avoiding overly strong spreading of the matrix (see **Chapter II**).

I.3.1.iii   Well defined *in-vitro* model of HA-rich matrix (HA brush)

To better understand the role of HA in the ECM, we studied a simplified *in-vitro* reconstituted model composed of end-grafted HA polymers (Figure I.8b). In this *in-vitro* model, polymeric HA molecules are specifically conjugated to the SAv functionalized substrate, as described above, with well controlled orientation through a biotin tag at the reducing end. The grafting density is tuned to obtain a brush like structure (144). The HA molecular weight in this *in-vitro* model is well-defined ($M_w =$ 280 kDa, corresponding to a contour length ~ 698 nm). With all these controlled properties, key features of the HA brush model as a function of external cues becomes quantitatively accessible by surface-sensitive biophysical techniques (20, 26, 29).

The HA brush model mimics the presentation of HA (through HASes) on cell surfaces in native ECMs but neglects any other ECM components. It allows focussing on HA behaviour under varying conditions, which is essential for extracting the physical principles underlying key features of HA matrices on the supramolecular level. The reduced complexity of this *in-vitro* model compared to the native matrix allows highly controlled measurements and to derive quantitative information of the mechanical properties correlating with the morphology of HA on supramolecular level under specific conditions. Previous studies on similar brush system by varying salt concentration revealed HA behaving as a strongly charged and semi-flexible polyelectrolyte (20). The effects of cross-linking proteins such as TSG-6 on such HA brushes were also well established (26). In this thesis work, the HA brush model is characterized within a broad range of solution calcium concentration and pH to reveal the effect of divalent cations and pH on the mechanical properties and the morphology of HA supramolecular assemblies (see **Chapter III**).

I.3.2   Biophysical characterization

I.3.2.i   Mechanical method: AFM

Since its invention in 1986 (145), AFM has developed rapidly and is now widely used in many scientific fields. The main applications of AFM go into three categories: force measurements, nanoscale topographic imaging and micro/nano-scale manipulation. AFM is a scanning probe technique, and all functions rely on the interaction between a microscopic (or nanoscopic) probe and a sample. In contrast to other scanning probe techniques, AFM can be operated in liquid, which makes it particularly interesting for biological specimen. We used atomic force microscopy (AFM) for force measurements on the COC matrix. The basic working principle of AFM force measurements on cells and tissues are described next.

I.3.2.i.a   *Force measurements by AFM − working principle*

The working principle of AFM is shown in Figure I.9. The sample is placed on a stage, in the case of cell and tissue specimen typically combined with an inverted optical microscope to enable simultaneous observation of the sample on the micrometer scale. A cantilever with a micron-sized tip (*i.e.* the probe) on the end approaches to or retracts from the sample by control from a piezoelectric scanner (*z*). Upon interaction between the tip and the sample, repulsion or attraction, the cantilever bends. A laser beam is reflected from the back side of the cantilever, and the laser beam movement due

to cantilever deflection is determined with a 4-quadrant photodiode. With known spring constant of the cantilever k, which is usually determined by the thermal noise method (146), the interaction force F can be obtained by simple Hooke´s law:

$$F = k \cdot \delta ,$$

where δ represents the cantilever deflection.
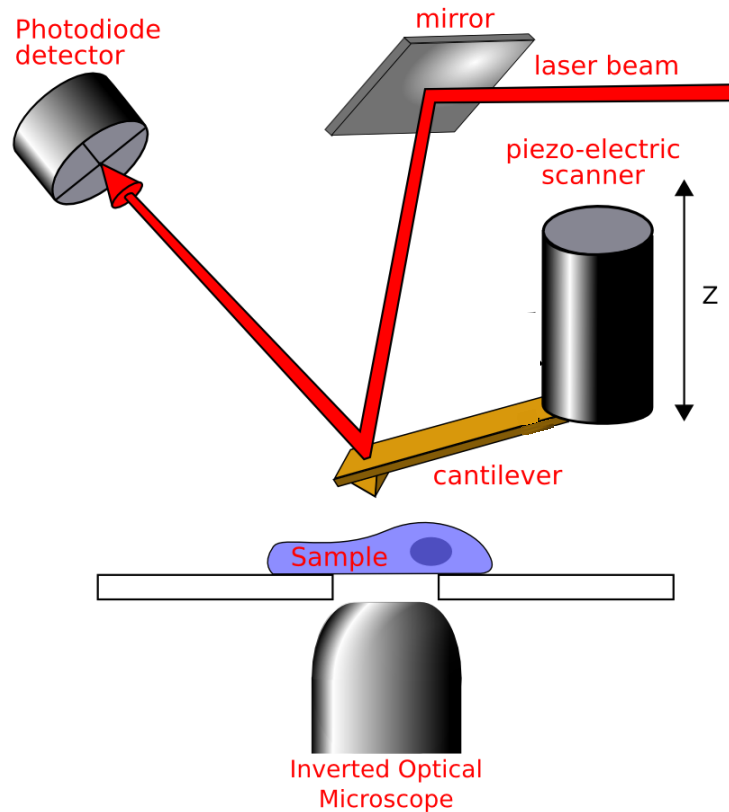
Figure I.9 Schematic of AFM setup for force measurements on cells or tissues. Image taken from website http://www.freesbi.ch/en/illustration/figures.

From the piezo movement z and the cantilever deflection δ, the distance between the probe and the sample, or the indentation depth if the probe has compressed the sample, are obtained. The output of AFM thus are curves presenting the interaction force as a function of the probe-sample separation/ indentation. Such curves provide insight into the nano/micromechanical properties of the sample, where the size of the probe defines the length scale of interactions being probed.

AFM is attractive for the micromechanical characterization of the COC for several reasons. First, AFM is applicable in aqueous environment, which is essential for adequate mechanical characterization of hydrates species (123, 147-150). Second, AFM allows probing micromechanical properties at controlled locations on the sample, so

that information about local mechanical properties and mechanical heterogeneity can be obtained. Finally, AFM is able to probe a large range of magnitudes in elastic modulus (from Pa to GPa (29, 151)) and length scale (from nm to μm (149, 152)). This is essential for measurements on the COC matrix considering its size and softness. In order to be sensitive to the range of mechanical properties characteristic for a given sample, the size of the probe and the softness of the cantilever need to be carefully selected.

I.3.2.i.b   Colloidal probe AFM

Conventional sharp AFM tips, which usually have an apex radius as small as a few nanometers, are crucial for high resolution AFM topographical imaging and provide good performance in compression of hard objects. However, they are not appropriate for the COC matrix or other biological materials that are very soft. Like a sharp knife, the sharp tip may cut into the sample without any appreciable force being measured. The accessible softness range can be significantly expanded by using colloidal probes, hard spheres of desired size, attached to cantilevers of appropriate softness.

Colloidal probe AFM, developed in the early 1990s (153, 154), is a versatile technique and popular for investigating the mechanical properties of thin films and macroscopic materials (154-157). It measures the forces, down to pN resolution, that act on a nanometer or micrometer-sized spherical probe as it interacts with the material of interest. An advantage of using colloidal probes is that their shape and size are well defined. This makes the geometry of interaction between probe and sample well-controlled. The interactions between the probe and sample can be quantified with improved sensitivity because at constant pressure (*i.e.* force per area) the total force increases compared to using a conventional sharp AFM tip (157). This is crucial for successful measurements on extremely soft materials, such as the COC matrix (see **Chapter II**).

I.3.2.i.c   Quantification of elasticity

The local elastic modulus E (Young´s modulus) of the sample can be determined from the interaction forces (F) *vs.* the probe-sample indentation (δ) curves using a classical theory in contact mechanics, the Hertz indentation model (158). For contact between a hard sphere and an elastic half space (*e.g.* in our experiments the spherical colloidal probe compressing on the COC matrix), the Hertz model gives

$$F = \frac{4}{3} \frac{E}{1-\mu^2} \sqrt{R\delta^3}$$

31

where R represents the radius of spherical probe and µ is Poisson's ratio (159) of the elastic material that can be fixed. Most materials have Poisson's ratio values ranging between 0 and 0.5 (160), and thus E will be over-/underestimated by at most 25% even if the exact value of µ remains unknown for a given sample.

The Hertz model makes a number of assumptions that are important to consider for its application. First, it assumes the elastic modulus of the sample to be much smaller than that of the probe, and the probe radius R to be much smaller than the effective radius of the sample. Second, the Hertz model requires the indentation depth δ to be small compared to the sample thickness. Third, the Hertz model is strictly valid only for indentation depths much smaller than the probe radius. Moreover, the Hertz model assumes zero probe-sample adhesion. Ultimately, the Hertz model makes the important assumption that the probed material is isotropic. **Chapter II** illustrates that these assumptions are fulfilled reasonably well for the analysis of COC matrix elasticity, and the Young´s modulus E of the COC matrix was thus extracted by applying the above equation to the F *vs*. δ curves acquired by AFM.

I.3.2.ii   Acoustical method: QCM-D

Quartz crystal microbalance with dissipation monitoring (QCM-D) has been widely used (161-163) to study soft and solvated interfaces. In this thesis, the mechanical properties of the *in vitro* HA brush model were analyzed by QCM-D.

I.3.2.ii.a   Working principle of QCM-D

The quartz crystal microbalance (QCM) relies on the piezoelectricity of quartz (164). Specifically, an electrical signal is used to excite a quartz plate into mechanical oscillation (inverse piezoelectric effect) and the response of the mechanical oscillations to changes in the environment (*e.g*. due to molecules binding to the quartz sensor surface) are then detected as an electrical signal (piezoelectric effect). As shown in Figure I.10, the sensor is made of a quartz crystal plate that is sandwiched between two electrodes. Shear oscillation of the quartz crystal can be excited by applying an AC electric field at a frequency close to the resonance frequency (f_1) that is related to the quartz crystal thickness, or to odd overtones (f_i, $i = 3, 5, 7…$) of the resonant frequency. The working principle of the QCM-D is based on the so-called ring-down approach (165), where the external electric field driving the oscillation is intermittently cut off and the decay of the oscillation is monitored. The resonance frequency (f) of the crystal and the energy dissipation (D) can be extracted from the oscillation profiles by fitting an

exponentially decaying curve. Both *f* and *D* are sensitive to processes occurring at the sensor surface, such as macromolecular binding events. QCM-D measures changes, Δf and ΔD, and allows monitoring of adsorption processes in real time in air and in aqueous environment. Key information about binding processes such as kinetics and stability, and about interfacial films such as morphology and mechanical properties, can be obtained by QCM-D in real time without any labelling. The time resolution of the QCM-D technique is typically better than 1 s.
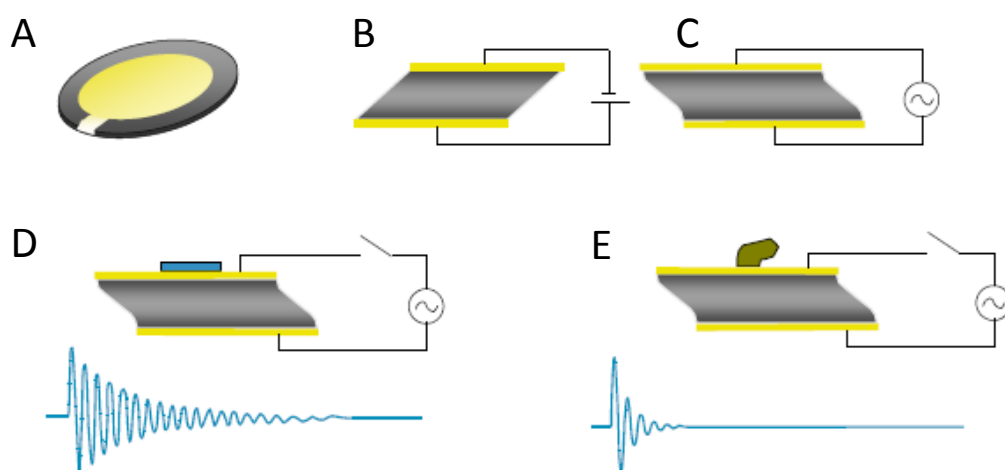
Figure I.10 Schematic of the QCM-D working principle. (A) A quartz crystal sensor where the piezoelectric quartz crystal is sandwiched between two gold electrodes. So-called AT-cut crystals have shear motion when an electric field is applied between the two electrodes (B). Oscillatory voltage (C) results in resonance of the shear motion. (D, E) After cutting the driving circuit, the freely decaying oscillation of the crystal is monitored. From the decay curve, the change in resonance frequency, Δf, and in energy dissipation, ΔD, due to attached components can be extracted. Attachment of both (D) a rigid mass and (E) a soft (viscoelastic) mass will lead to decreasing in resonance frequency, while the latter also results in faster energy dissipation.

From the frequency shift, the adsorbed areal mass density can be estimated by the Sauerbrey equation (166), given by

$$\Delta m = -C\frac{\Delta f_i}{i},$$

where C is the mass sensitivity constant that depends solely on the material properties of the sensor crystal. For a typical quartz sensor with a fundamental frequency of $f_0 \approx$ 4.95 MHz, $C = 18$ ng·cm^{-2}·Hz^{-1}. The resolution in frequency is currently in the range of

0.2 Hz (in liquid), corresponding to a resolution in areal mass density of a few ng/cm^2. Although originally derived for applications in air or vacuum 198, the Sauerbrey equation is also valid for films immersed in Newtonian liquids such as water. It is important to note that solvent that is hydrodynamically trapped in the interfacial film also contributes to the areal mass density determined by QCM-D. However, for the Sauerbrey equation to hold, the films have to be sufficiently rigid. Soft films will not fully couple to the crystal oscillation resulting in underestimation of the mass by the Sauerbrey equation. Soft film will give rise to an increase in dissipation, as well as Δf and ΔD. The viscoelastic properties of these films can be accessed (161). Quantitative information about the viscoelastic properties can in some cases be extracted by fitting the QCM-D data with viscoelastic models (161, 167). A simple way to obtain information about trends in film rigidity that is robust and does not require extensive data fitting is to consider the parameter $-\Delta D/\Delta f$. To a first approximation, this parameter relates to the elastic compliance (or simply softness). This parameter is used in this thesis to describe the effects of environmental conditions on the mechanical properties of HA brushes (see **Chapter III**).

Another advantage of the QCM-D is that it readily allows *in situ* measurements in aqueous environment while exchanging the properties of the liquid medium surrounding the film of interest on the sensor surface. This is essential for characterizing the effect of changes in the ionic strength and pH on HA brushes over a large parameter range, as done in this thesis (see **Chapter III**).

I.3.2.iii   Optical method: RICM

Reflection interference contrast microscopy (RICM) is employed in this thesis to probe the HA brush morphology (*i.e.* thickness). RICM is an interferometric technique. It was initially applied to study the interaction between cells and a planar substrate to characterize the distance between the glass substrate and the underside of a living cell (168). Later, the setup was greatly improved by introducing the antiflex method to enhance the image contrast (169, 170). Subsequent work revealed that the quantitative analysis of the RICM images for cell-substrate distances study is challenging due to the presence of many partially reflecting interfaces within living cells (169). Instead, RICM with improved contrast was found to have excellent potential for characterizing the distance between a planar transparent substrate and simplified biological specimen such as giant unilamellar vesicles or spherical objects such as colloidal probes of several

micrometers in size (171, 172). A colloidal probe hovering on top of a soft solvated film thus can be exploited to determine the film thickness. The working principle of colloidal probe RICM is introduced below.

I.3.2.iii.a   Working principle of colloidal probe RICM

In the RICM setup with a spherical colloidal probe based on an inverted optical microscope (Figure I.11), the incident light beam with intensity I_0 is first partially reflected at the substrate/solution interface as I_1, while the rest is transmitted through the solution and partially reflected at the solution/colloidal probe interface. This second reflected beam passes back through the solution/substrate interface with proper refraction and intensity I_2. The two reflected beams interfere with each other, giving rise to a pattern of concentric fringes, also called Newton's rings, with intensity maxima (I_{max}) and minima (I_{min}). In the simplest approximation, we can assume the incident and reflected beams to be parallel to the optical axis. In this case, the relation between intensity distribution I and the probe-substrate separation h is given by:

$$I(h,\lambda) = I_{min} + I_{max} + 2\sqrt{I_{min}I_{max}}\cos\left[\frac{4\pi n h}{\lambda} + \Phi\right],$$

where n is the refractive index of the solution, and λ the wavelength of the light source. Φ stands for the phase shift of the light upon reflection at the probe surface (169).

The probe-substrate separation h can be determined by simple analysis of the fringe pattern (169) (Figure I.12), from the radial position of a selected extremum, j, in the intensity profile through:

$$h_{min}^{(l)} = \frac{\lambda l}{2n} - R + \sqrt{R^2 - r_j^2} \text{ , if } j \text{ is a minimum, and}$$

$$h_{max}^{(l)} = \frac{\lambda(2l+1)}{4n} - R + \sqrt{R^2 - r_j^2} \text{ , if } j \text{ is a maximum,}$$

where R is the radius of colloidal probe (that can be determined from the bright field image of the colloidal probe), l is the fringe order and r_j the radial position of the extremum j.
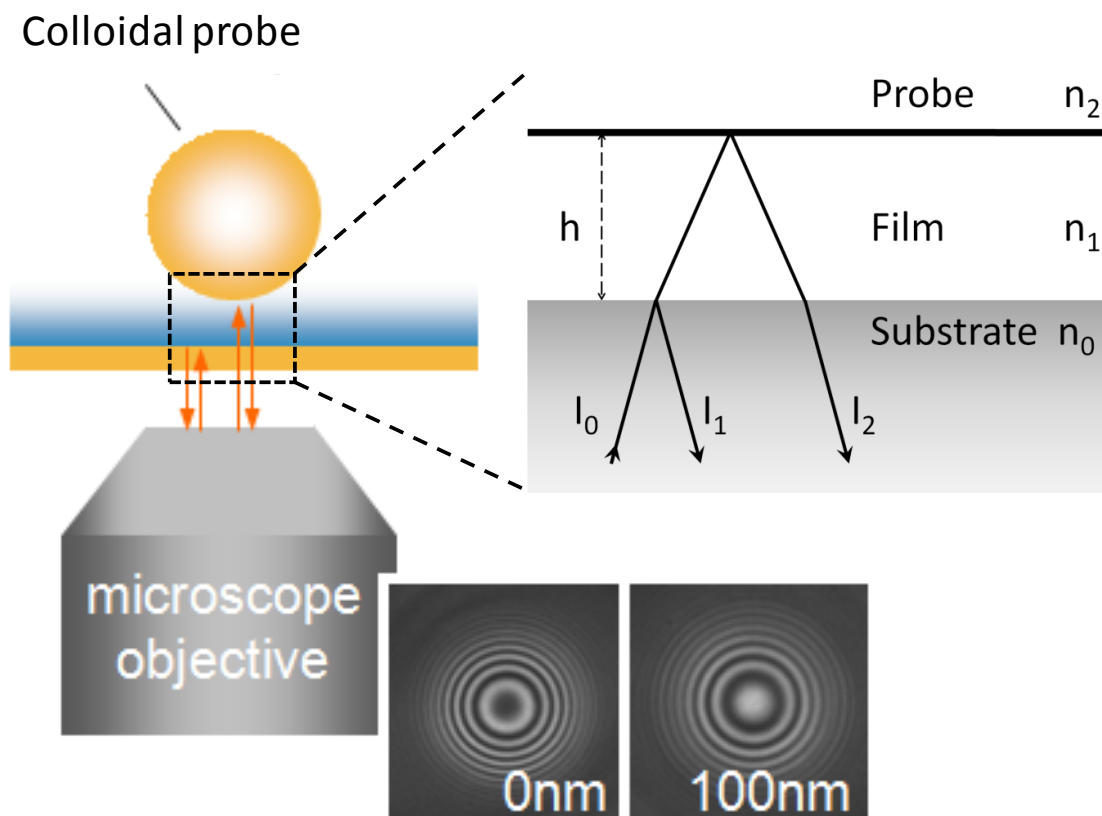
Colloidal probe

Figure I.11 Schematic of the RICM setup and the interference principle. The incident light beam (intensity I_0) is reflected at two interfaces. The two reflected beams interfere with each other. With a spherical colloidal probe and a flat substrate, a pattern of concentric fringes (Newton´s rings) arises from the distance-dependent constructive/destructive interference.
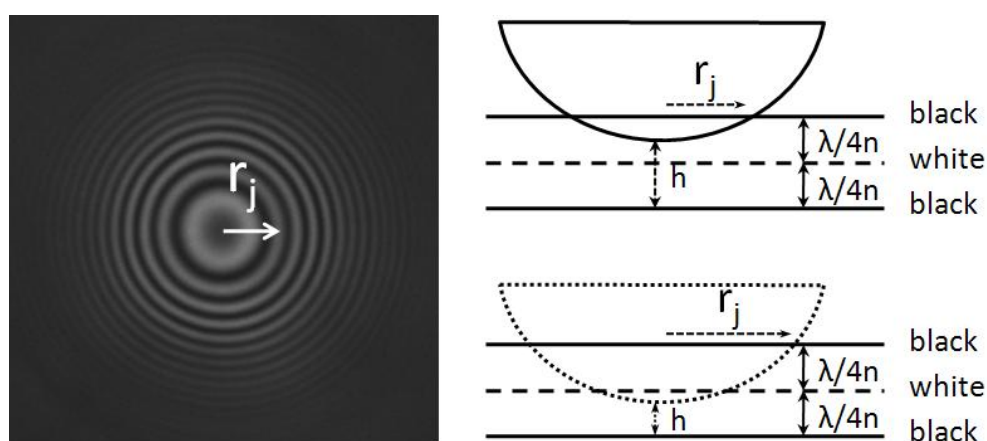
Figure I.12 Rationale of the RICM fringe pattern forming. When the colloidal bead changes its height h above the substrate, the radial positions of the fringes change. For instance, the radius of the first dark fringe r_j increases if the bead approaches the

substrate, as illustrated schematically on the right. The solid/dashed line represents heights at which a fringe looks dark/bright.

From this interference pattern, the distance between sphere and substrate can be extracted with a resolution of a few nanometers (169). The limitation of ambiguities in distance determination that is intrinsic to the periodicity of interferometric responses can be overcome by dual or triple wavelength RICM. This can extend the maximum accessible probe-substrate distance to one micrometer and more.

In this thesis work, the suspended colloidal probe is separated from the substrate by a HA brush, and thus the separation distance between the probe and the substrate is an effective measure of HA brush thickness (see **Chapter III**). RICM is particularly well suited to determine the thickness of very hydrated and soft films, for which the thickness characterization by techniques such as QCM-D and ellipsometry is difficult. RICM is a label-free technique and thus does not require chemical modification of the HA film. It should be kept in mind that the interactions between the probe and the film (*e.g.* gravitational forces or electrostatic repulsion) will affect the effective thickness measured by RICM.

I.3.3   Theoretical method: Polymer physics theory

The morphology of HA brushes and matrices is determined by the molecular properties of HA. Polymer physics theory can help understanding the mechanisms underlying the assembly of polymer brushes (such as the HA brush) and how these are affected by different conditions such as solvent quality change or cross-linking between polymer chains.

Polymers such as HA are large molecules and continuously affected by thermal fluctuation in liquid solution, and thus it is difficult to mathematically describe a system composed of polymers by any deterministic method. In contrast, theories in polymer physics field are powerful to study polymers, including their fluctuations, mechanical properties and morphological features (173-175). The general idea of polymer physics theory is to consider a polymer as many segments and use statistical approaches to describe the collective behaviour of the segments under given conditions and constraints. The simplest model of a polymer is the freely-jointed (ideal) chain, which assumes fixed-length segments to be linearly connected and all bond and torsion angles equiprobable while having no additional interactions between chain segments. Models of increasing complexity consider also the interactions between polymer segments in

various ways (175, 176). Moving beyond the level of individual polymers, polymer physics can also make predictions about the self-organization of polymer chains, for example, in the case of polymers densely grafted on a surface. The next paragraphs introduce some basic concepts of polymer physics theory that are relevant to the work in this thesis.

I.3.3.i.a   *Polymer brush*

In the experimental system of interest, polymers (*i.e.* HA) are end-grafted to a solid substrate. Polymer chains grafted onto a planar solid substrate can adopt two distinct conformations (Figure I.13), provided that only the polymer end is attached to the surface. The preferable conformation depends on the magnitude of the size of the polymer in solution compared to the mean distance s between adjacent anchor points. The polymer size in solution is adequately described by the radius of gyration R_g, which defines the mean distance of the polymer segments from the polymer´s centre of mass. If s is greater than R_g, a so-called 'mushroom' like conformation is adopted. In this case, the conformation of each polymer chain is not much different from that of a free isolated chain in solution, and consequently the thickness of this mushroom film is about R_g. When s is smaller than R_g, then the inter-polymer repulsion leads to stretching of the polymers away from the surface. This conformation is termed a polymer 'brush'. Thus, by decreasing the distance between grafting points, polymer chains transit from the mushroom to the brush regime.
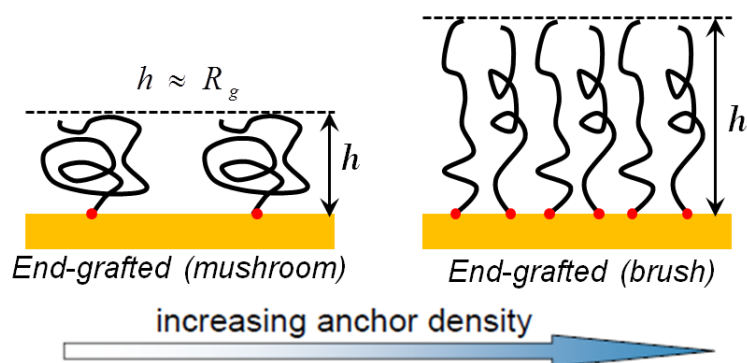
Figure I.13 Morphology of flexible polymer chains attached to solid flat substrate.

I.3.3.i.b   *Polyelectrolyte brush*

Of particular importance for the morphology of brushes are the interactions between polymer chains, where the degree of repulsion will determine how strong the polymers are stretched. A special case of relevance here is the repulsion through charges. HA is a

charged polymer, that is, a polyelectrolyte (PE). The behaviour of PE brushes depends on the charge density along the polymer chain and the ionic strength of the environmental solution, in addition to the grafting density. Three distinct regimes can be distinguished for strong polyelectrolytes (177-179) (Figure I.14), where strong refers to the scenario in which the degree of charging of the chargeable groups on the PE is not affected by ionic strength.
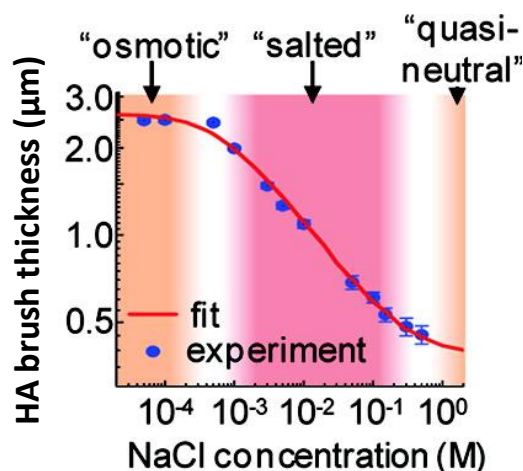
Figure I.14 Effect of ionic strength on the morphology of PE brush. Experimental data (blue dots) and theoretical fit (red line) of the thickness of a brush formed by HA (M_w = 1.08 ± 0.05 MDa, contour length ~ 2.86 μm) were obtained at different NaCl solution concentrations (*i.e.* ionic strengths), as describe elsewhere (20). The three canonical brush regimes – osmotic, salted and quasi-neutral – can be identified and are indicated with the coloured background. Image modified from ref. (20).

When the concentration of counterions inside the PE brush is higher than the ion concentration in the surrounding bulk solution, the osmotic pressure of the counterions will dominate the chain stretching. In this osmotic regime, the equilibrium brush thickness is determined by the balance between the elastic pressure generated by chain stretching and the counterion osmotic pressure, and independent of the ionic strength of the solution. When the ionic strength of the bulk solution becomes larger than the concentration of counterions within the brush, the brush thickness will decrease upon addition of salt because the electrostatic repulsions between chains become increasingly screened. This regime is called the salted brush. In quasi-neutral regime, the screening of electrostatic interactions approaches saturation. Here, the intrinsic excluded volume of the polymer backbone dominates the brush thickness and the ionic strength dependence is again weak (*i.e.* the brush thickness attains a plateau).

I.3.3.i.c   Cross-linked brush

Cross-linking has been widely used to produce synthetic HA matrices (116-118, 121). It also plays an important role in native HA matrices. For instance, HA was confirmed to be cross-linked by interacting with TSG-6 (26), a protein that is expressed during inflammation (36). More generally, the (reversible) cross-linking of flexible polymers is also important in other biological systems. A case in point is the nuclear pore permeability barrier, where intrinsically disordered proteins (so-called FG domains) fill the channels of nuclear pore complexes (NPCs) and regulate the transport of macromolecules into the nucleus of cells. Interestingly, FG domains are end-grafted to the channel walls of the NPC and thus likely to form a brush. In contrast to HA being cross-linked by external linkers, the FG domains can crosslink via phenylalanine-glycine dipeptides (FG motifs) along each chain (180). To date, a theory that rationalises the effect of reversible cross-links on the morphology of polymer brushes is lacking. In **Chapter IV** we develop a first analytical theory of reversibly cross-linked brushes that is based on mean field theory.

I.3.3.i.d   Mean field theory

A polymer brush is a stochastic many-body system, which can be mathematically described by mean field theory. This theory approximates the effects of all other individuals on any given individual by a single averaged effect (a field), and thus reduces a many-body problem to a one-body problem. Mean field theory has been remarkably successful in predicting morphological features of polymer brushes, such as the effect of solvent quality or ionic strength (178, 179, 181, 182). Mean field theory often provides analytical expressions and thus enables the correlation of parameters to be easily accessed, in contrast to other simulation methods (183, 184). Mean field theory is employed in this thesis to study the morphology of a polymer brush as it is affected by changes in ionic strength (**Chapter III**), solvent quality or cross-linking (**Chapter IV**). Some basic concepts used in mean field theory and pioneering work is introduced in the next paragraphs as a background for the theoretical approach developed in **Chapter IV**.
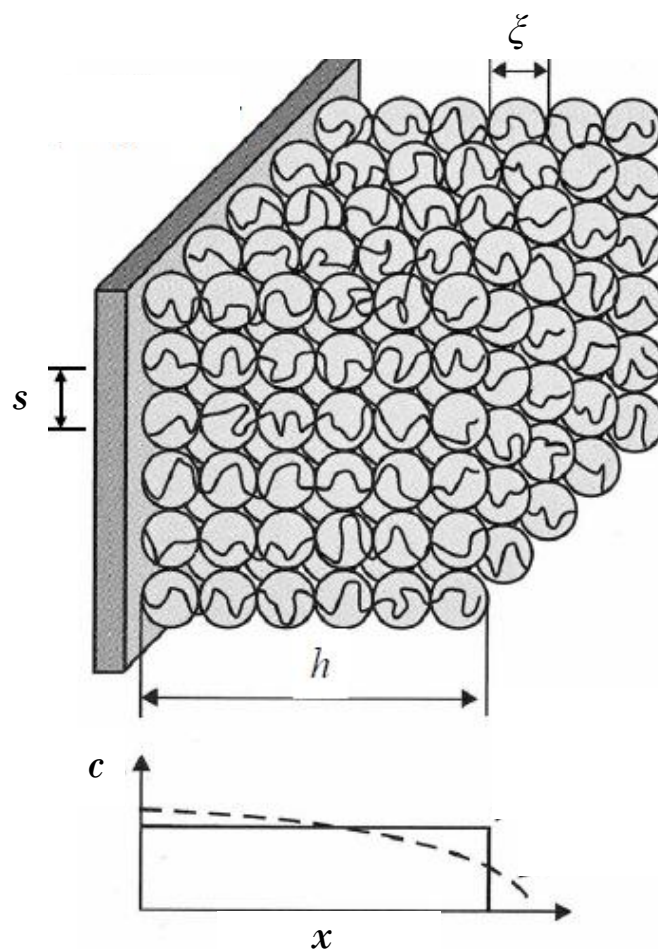
Figure I.15 Illustration of the scaling concept and blob model of a polymer brush and its density profile. The bottom curves represent the profiles of density c as a function of the distance away from grafting surface x. Alexander-de Gennes model assumes a box profile (solid line); the improved calculations by SCFT predict a parabolic density profile (dashed line) instead. Image modified from ref. (175).

Consider a brush on a flat surface formed by polymers each containing N statistical monomer units of length a in good solvent. Pioneering work by Alexander and de Gennes (185) gave a first theoretical description of brush morphology. This theory exploited the concept of blobs. Polymer chains can be seen as a series of virtual blobs (as shown in Figure I.15). Each blob is thought to have a free energy of kT, implying that the thermal motion is predominant within each blob whereas the external forces become predominant at length scales above the blob size ξ. Such a separation of length scales facilitates the understanding of polymer behaviour. According to Alexander-de Gennes theory, the average distance between neighbouring anchor points s on a planar surface dictates the size of the blobs (i.e. $\xi = s$). The equilibrium brush thickness h is

given by the balanced energy considering both the interaction energy (excluded volume interactions) between the statistical segments and the energy of elastic stretching of the chain (175). This simple model assumes that the free ends of the (monodisperse) chains are all located at the same distance h away from the grafting surface, which implies all chains are stretched equally. The profile of segment density c as a function of the distance away from the surface x can then be described by a step-function (box profile, Figure I.15). In their scaling theory, the equilibrium brush thickness h is then given by

$$h \propto \sigma^{1/3} aN,$$

where $\sigma = (a/s)^2$ is the grafting density and the equation is accurate to within a numerical prefactor of order unity.

Later work based on self-consistent mean field theory (SCFT) provided a more reasonable density profile of polymer brushes (186-189). This approach takes advantage of the fact that local fluctuations around monomers can be neglected to a first approximation for a sufficiently stretched brush. Instead of assuming the free ends of the chain to be positioned exclusively at the brush edge, the distribution was determined self-consistently by this approach. A key prediction of SCFT is that the chain segment density profile for brushes in good solvent is parabolic (Figure I.15). The SCFT provides a brush thickness approximation, given by

$$h = \left(\frac{8}{\pi^2}\right)^{1/3} \sigma^{1/3} aN.$$

As can be seen, the simple Alexander-de Gennes model despite its crude assumption about the chain end positions predicts the brush thickness correctly except for the lacking numerical prefactor. In the presence of cross-linking, the interaction free energy of chains in the brush comprises not only the excluded volume interactions between segments, but also the contribution from the association between pairs of stickers. By adding this sticking term into the SCFT, the morphology of cross-linked polymer brushes can also be self-consistently determined and correlated with experimental systems (see **Chapter IV**). We have chosen to use FG domain brushes for a first comparison, because data were available in the lab. However, future extension of the theory could also be applied to HA brushes.

II Micromechanical properties of native HA-rich tissue: the COC matrix

The research work presented in this chapter is in press in *Biophysical Journal* as:

Micromechanical analysis of the hyaluronan-rich matrix surrounding the oocyte reveals a uniquely soft and elastic composition

Xinyue Chen,[1,2] Rita Bonfiglio,[3] Suneale Banerji,[4] David G. Jackson,[4] Antonietta Salustri,[3] and Ralf P. Richter[1,2,5]

[1] CIC biomaGUNE, San Sebastian, Spain; [2] Max-Planck-Institute for Intelligent Systems, Stuttgart, Germany; [3] University of Rome Tor Vergata, Department of Biomedicine and Prevention, Faculty of Medicine, Rome, Italy; [4] MRC Human Immunology Unit, Weatherall Institute of Molecular Medicine, University of Oxford, Oxford, UK; [5] University Grenoble Alpes - CNRS, Laboratory of Interdisciplinary Physics (LIPhy), Grenoble, France.

My contribution: I co-designed research (together with Antonietta Salustri and Ralf P. Richter). With biological samples (including the COCs and essential protein reagents) prepared by others, I performed all AFM/optical microscopy measurements and analysed the data. I improved the data analysis method and interpreted the data (together with Ralf P. Richter). I prepared all figures and wrote the first draft of the article, as well as contributed to subsequent corrections to complete the article for publication.

Abstract: The cumulus cell-oocyte complex (COC) matrix is an extended coat that forms around the oocyte a few hours before ovulation and plays vital roles in oocyte biology. Here we have analyzed the micromechanical response of mouse COC matrix by colloidal probe atomic force microscopy (AFM). We found that COC matrix is elastic insofar as it does not flow and its original shape is restored after force release. At the same time, COC matrix is extremely soft. Specifically, the most compliant parts of *in vivo* and *in vitro* expanded COC matrices yielded values for the Young's modulus of 0.5 ± 0.1 Pa and 1.6 ± 0.3 Pa, respectively, suggesting both high porosity and a large mesh size (≥ 100 nm). In addition, the elastic modulus increased progressively with indentation. Furthermore, using optical microscopy to correlate these mechanical properties with ultra-structure, we discover that the COC is surrounded by a thick matrix shell that is essentially devoid of cumulus cells and enhanced upon COC expansion *in vivo*. We propose that the pronounced non-linear elastic behaviour of COC matrix is a consequence of structural heterogeneity and serves important functions in biological processes, such as oocyte transport in the oviduct and sperm penetration.

II.1   INTRODUCTION

Cumulus cells are a distinct population of somatic cells surrounding the oocyte in mature ovarian follicles (53). In response to the hormone surge that ultimately triggers ovulation, they produce a unique oocyte-embedding matrix. This process, known as cumulus expansion, involves the rapid synthesis of hyaluronan (HA) (85), a polysaccharide of the glycosaminoglycan family, and in concert, the cross-linking of HA polymers with a complex of several distinct proteins and proteoglycans (28, 83, 190-193). The resulting matrix, termed the cumulus cell-oocyte complex (COC) matrix, contains not only the oocyte but also a large number of cumulus cells, and is essential for successful ovulation and *in vivo* fertilization. In particular, the COC matrix has been proposed to modulate cumulus cell and sperm intracellular signalling (53), and it is known to facilitate the transport of COCs along the oviduct (99) and to play important roles in the attraction (83, 103), capacitation (104) and selection (105) of sperm. Consequentially, the quality of cumulus expansion has also been a criterion for the selection of oocytes towards *in vitro* fertilization (IVF) for many years (194). Intact COCs can also be isolated from the follicle and stimulated to synthesize hyaluronan rich matrix during *in vitro* maturation (IVM) of mammalian oocytes. Although the *in vitro* synthesized matrix is apparently similar to that formed *in vivo*, it has been suggested that it could be deficient of some components provided within the ovarian follicle by neighboring cells, thereby establishing a different microenvironment for the oocyte (53).

It is now well established that the mechanical properties of extracellular matrix (ECM) have profound effects on the cells that they surround, and critically affect basic cellular processes such as proliferation, motility (45) and differentiation (46), in addition to pathologies such as tumour progression (48). Thus, it is reasonable to hypothesize that the mechanical properties of the COC matrix also contribute to the control of oocyte behaviour. The functional importance of COC matrix softness is strikingly illustrated, for example, in videos of oocyte pickup by the mammalian oviduct where a perturbed and stiffened matrix was found to impair transport (51). Moreover, the mechanical properties of the ECM are ultimately determined by the properties of the constituent molecules and their interactions. Salient morphological features of the COC matrix are extreme hydration, a highly dynamic nature and a low degree of order, and these make it difficult to study the ultrastructure of the COC matrix directly with conventional methods such as optical or electron microscopy. In this

regard, the characterization of mechanical properties can indirectly provide valuable information about matrix morphology and ultrastructure. Currently, however, only very limited information about the mechanical properties of the COC matrix is available. Whereas its elasticity has been documented on the basis of a macroscopic stretching assay (195) and an oviduct transport assay (196) developed many years ago, we are still lacking knowledge about the local mechanical properties and the mechanical heterogeneity of the COC matrix.

Several methods to probe the local mechanical properties of tissues, extracellular matrix and cells have emerged over the last two decades, including particle tracking microrheology (197, 198), optical force probe microscopy (124) and atomic force microscopy (AFM) (147, 149, 150, 152, 199, 200). The ability to probe a large range of magnitudes in elastic modulus (from Pa to GPa (29, 151)) and length scale (from nm to μm (149, 152)) makes AFM particularly versatile (157). In colloidal probe AFM, this is achieved by using hard spheres of desired size as indentation probes attached to AFM cantilevers of appropriate softness.

In the present study, we analyze the micromechanical response of mouse COC matrix using colloidal probe AFM. We identify the COC matrix as a biological material that displays a unique combination of elasticity and extreme softness. Secondly, using quantitative compressibility analysis we reveal the COC matrix to be mechanically heterogeneous. Finally, by combining AFM with optical microscopy we show this unusual heterogeneity stems from an additional and previously undescribed thick outer matrix layer that is completely devoid of cumulus cells. We discuss the implications of our findings for the nanoscale morphology and potential biological functions of the COC matrix.

II.2   MATERIALS AND METHODS

II.2.1   Materials

Oligo-ethylene glycol (OEG) was prepared as a solution comprising a 1 mM mixture of OEG thiol (386.5 Da) and biotinylated OEG thiol (788 Da; both Polypure, Norway) at a molar ratio of 99:1 in synthesis grade ethanol, and stored in the dark at 4 °C. Lyophilized streptavidin (SAv; Sigma-Aldrich) was dissolved in ultrapure water and stored as aliquots at a concentration of 1 mg/mL at -20 °C. Lyophilized bovine serum

albumin (BSA; Sigma-Aldrich) was freshly dissolved in ultrapure water and used at a concentration of 10 mg/mL for all passivation purposes.

A 'sample preparation buffer' comprising 10 mM HEPES and 150 mM NaCl at pH 7.4 was used for the preparation of COC-capturing substrates. Throughout the AFM measurements, COCs were maintained in 'culture medium' consisting of Minimum Essential Medium (MEM) with Earle's salts, buffered at pH 7.3 with 20 mM HEPES and supplemented with 50 μg/ml gentamycin, 0.3 mM sodium pyruvate, 1 mg/ml BSA and 1 mM 8-bromoadenosine 3',5'-cyclic monophosphate (8-Br-cAMP), a membrane-permeable cyclic AMP analogue that stabilizes the expanded cumulus matrix (201).

Polystyrene microspheres with 91.0 ± 1.3 μm diameter (Polysciences, Germany) were washed first in ethanol and then in ultrapure water, 5 times each, dried in a vacuum oven at 40 °C for 3 h, and stored at 4 °C.

II.2.2   Cloning and purification of biotinylated and soluble CD44

The full CD44 ectodomain sequence terminating at Proline 267 was amplified from human CD44S cDNA using the high fidelity polymerase pfu Ultra AD (Agilent) together with the forward primer hCD44 -14 BamHI F 5' GCG_GGATCC_GAAGGGGTAGGCACGATGGCCAGG and the reverse primer hCD44 801 10H* XhoI R 5' GCGC_CTCGAG_*TTA*GTG ATGGTGATGGTGATGGTGATGGTGATGCCACTCGATTTTCTGTGCCTCGAAG ATGTCATTCAGGCCGGATCTAGGAATTTGGGGTGTCCTTATAGG which encodes a target site for biotin ligase and a ten histidine tag. The amplified fragment was cloned into a variant of the pHR Sin vector (202) carrying an internal ribosome entry site (IRES) upstream of a gene encoding emerald GFP and introduced into HEK 293T by transfection. Culture supernatants containing virus-like particles were then used to transduce CHO K1 cells together with the lentiviral packaging and envelope plasmids pMD.G and p8.91 using Genejuice (Merck, Darmstadt, Germany) and selected for GFP expression by flow cytometry. Secreted CD44 His-tagged protein was subsequently purified from culture supernatants using a His Trap column (GE Healthcare) prior to biotinylation using a BirA-500 kit (Avidity, CO, USA) according to the manufacturer's instructions and removal of free biotin by size exclusion chromatography. The purified CD44 protein with C-terminal biotin tag (b-CD44) was stored at 0.5 mg/mL in phosphate buffered saline (PBS) at -20 °C until use for the preparation of COC-capturing substrates.

II.2.3   Preparation of colloidal probe AFM cantilevers

Tipless V-shaped Si_3N_4 cantilevers with a nominal spring constant of 0.06 N/m (NP-OW, Veeco Probes, USA) were treated for 30 min with UV/ozone (UV/Ozone ProCleaner, Bioforce Nanoscience, USA). Polystyrene microspheres were dispersed on a cleaned and UV/ozone treated glass cover slip, and attached to the cantilever by a UV-cured adhesive (NOA 61, Thorlabs, Germany). Positioning and attachment were aided by a micromanipulator (Patchstar; Scientifica, UK) and an optical microscope (Axio Observer; Zeiss, Germany). The real cantilever spring constant was determined as 0.076 ± 0.004 N/m using the thermal noise method (146) from an average over three cantilevers with colloidal probes attached. Before use, the colloidal probe AFM cantilever together with the chip and chip holder were immersed in BSA for 20 min, for surface passivation. Excess BSA was removed by washing with sample preparation buffer.

II.2.4   Preparation of substrates

Glass cover slips (1.5 mm, 24 x 24 mm^2, Menzel Gläser, Germany) were gently wiped with lint-free tissue (Kimtech Science, USA), immersed for 3 h in freshly prepared piranha solution composed of concentrated H_2SO_4 (95% - 98%, Scharlab, Spain) and H_2O_2 (50%, Scharlab, Spain) in a 3:1 volume ratio, thoroughly rinsed with ultrapure water, blow-dried with N_2 gas and stored in sealed petri dishes. For gold (Au) coating, clean glass cover slips underwent 10 min plasma cleaning in the vacuum chamber of a magnetron sputter system (ATC 1800 UHV, AJA International, USA) before deposition of a 0.5 nm adhesive titanium (Ti) interlayer followed by a 5 nm Au layer. All substrates were UV/ozone treated for 30 min prior to further use.

To generate COC-capturing substrates, a previously established protocol (26, 141) for the orientated immobilization of biotin-tagged molecules was applied. The Au coated cover slips were first immersed in OEG solution overnight, rinsed with ethanol and ultrapure water, blow-dried with N_2 gas, and attached, using a two-component glue (Twinsil; Picodent, Germany), to a titanium holder that was custom-designed for operation with a combined atomic force/optical microscopy setup. The surface coated with the biotinylated OEG monolayer was then incubated with 20 μg/mL SAv for 30 min, followed by 5 μg/mL b-CD44 for 30 min. Excess proteins in the solution phase were removed by rinsing after each incubation step, and protein-coated surfaces were kept wet throughout the preparation and measurement procedures.

II.2.5 *In vivo* and *in vitro* expansion of COCs

In vivo and *in vitro* expansion of mouse COCs was induced as described previously (85). Briefly, adult female Swiss CD1 mice were primed by intraperitoneal injection of 5 IU pregnant mare serum gonadotropin (PMSG), to promote the formation of multiple antral follicles, and, 44 to 48 h later, received a 5 IU intraperitoneal injection of human chorionic gonadotropin (hCG) to induce COC expansion and ovulation. *In vivo* expanded COCs were then isolated from oviducts soon after ovulation (14 hrs from hCG injection), and transferred with a glass micropipette to tubes in ice containing 100 µl of culture medium, and immediately frozen at -80 °C.

To induce *in vitro* expansion, female mice were sacrificed 44 to 48 h after PMSG injection and COCs isolated from the ovaries. Approximately 10 COCs were cultured under oil in a 20 µl drop of culture medium containing 1 mM 8-Br-cAMP and supplemented with 5% fetal calf serum (FCS) for 15 h at 37 °C in 5% CO_2. At the end of culture, *in vitro* expanded COCs were collected and stored as described for *in vivo* expanded COCs.

II.2.6 Immobilization of COCs

COCs were thawed on ice for approximately 1 h before transfer to COC-capturing substrate. Visual inspection under the microscope revealed thawed *in vivo* expanded COCs to be comparable in appearance to those freshly isolated from the oviduct. In particular, the spatial extension of the cumulus cell cloud was not visibly altered by the freeze-thawing cycle and remained virtually unchanged for several hours following thawing. The matrix did not dissociate and the mechanical response of the matrix to gentle stretching with a pair of tweezers also remained comparable, indicating that the freeze-thawing cycle did not affect the matrix morphology appreciably.

200 µL micropipette tips modified to enlarge the aperture diameter, to ensure COC uptake and release with minimal stress, and passivated with BSA, to reduce COC adhesion, were used for the transfer. The tips were gently manipulated (with monitoring through a phase contrast microscope), to facilitate isolation of individual oocytes with their cumulus matrix from the original multi-oocyte clusters and their subsequent immobilization at desired positions on the COC-capturing substrate. Care was taken to keep the COCs fully immersed in solution during the immobilization process, and 100 µL measurement solution was added after COC immobilization. AFM measurements were performed at room temperature and typically lasted 2 to 5 h. Immobilized COCs

were found to be stable during this time, *i.e.* the spatial arrangement of the oocyte and the cumulus cells did not change appreciably. Matrix deformation under gentle stretching with tweezers was qualitatively similar at room temperature and at 37 °C, suggesting that the mechanical properties do not change appreciably over this temperature range.

II.2.7   Force measurements by colloidal probe atomic force microscopy

AFM measurements were performed with a NanoWizard II (JPK Instruments, Germany) installed on an optical microscope (Axio Observer; Zeiss, Germany). The AFM was equipped with a CellHesion module providing a z-piezo actuation range of 100 μm. The approach speed was 20 μm/s unless stated otherwise. The cantilever sensitivity was determined prior to each measurement, from the hard-wall-contact regime of force curves obtained on a cleaned and BSA-passivated glass cover slip in sample preparation buffer. COC-capturing substrates bearing COCs were then mounted and probed in measurement solution. Reference force curves were acquired at locations devoid of COCs, to define the z location of the substrate and to test for contaminants on the colloidal probe. Only probes that showed minimal interactions (*i.e.* less than 1 μm interaction range) prior to hard-wall contact were used for further analysis. Force curves on the COC were acquired at desired positions, with a lateral resolution of a few μm (determined by the accuracy of the microscope's manual *xy* translation stage) and an accuracy in the distance from the glass substrate of approximately 10 μm (determined from the repeatability in z positioning by the stepper motor of the AFM head). At least three force curves were collected per position.

Data were corrected for linear thermal drifts in the cantilever deflection, and force *vs.* distance curves were computed using established methods (157) implemented in JPK Data Processing Software. Fits of contact mechanics models such as the Hertz model (*vide infra*) to force curves were also performed with the JPK Data Processing Software, with the measured forces around the contact point $\delta = 0$ averaged and offset to zero.

II.3   RESULTS

II.3.1   Immobilization of the COC matrix and experimental setup

The experimental setup used to characterize the local response of COC matrix to compression is schematically shown in Figure II.1*A*. The AFM cantilever was used with a colloidal probe (*i.e.* a microsphere) of 90 μm diameter. Such large probes were necessary to provide the required sensitivity for the assays. In initial tests, we noted that the COCs did not adhere efficiently to plain glass or plastic substrates - a critical requirement for reproducible AFM measurements. Hence, we prepared a streptavidin functionalized substrate which was coated with soluble biotin tagged ectodomains of the hyaluronan receptor CD44 (Figure II.1*A*, *inset*) to allow more stable tethering via hyaluronan in the COC matrix (23). The streptavidin monolayer thus serves as a 'molecular breadboard' (141) on which CD44 is immobilized via its carboxyl terminus with its ligand binding domain arranged in the same orientation as the intact receptor in the cell membrane. As shown in Figure II.1*B*, when a COC approaches the CD44 functionalized substrate, it adhered rapidly and the immobilized COC adopted a stable morphology within a few seconds. This immobilization method worked for COCs expanded *in vivo* as well as *in vitro*. We compared these two types of matrix to assess if the *in vitro* expansion conditions affect COC matrix mechanics compared to the *in vivo* scenario. Importantly, COCs did not adhere in the absence of CD44, indicating that the immobilization occurs specifically via hyaluronan. Inspection by optical microscopy revealed that cumulus cells in the COC that were located adjacent to the substrate remained immobile under the influence of gentle pipette-induced flow, indicating firm adhesion of the COC matrix. By comparison, more distantly located cumulus cells were transiently displaced, indicating that the matrix was easily deformed.
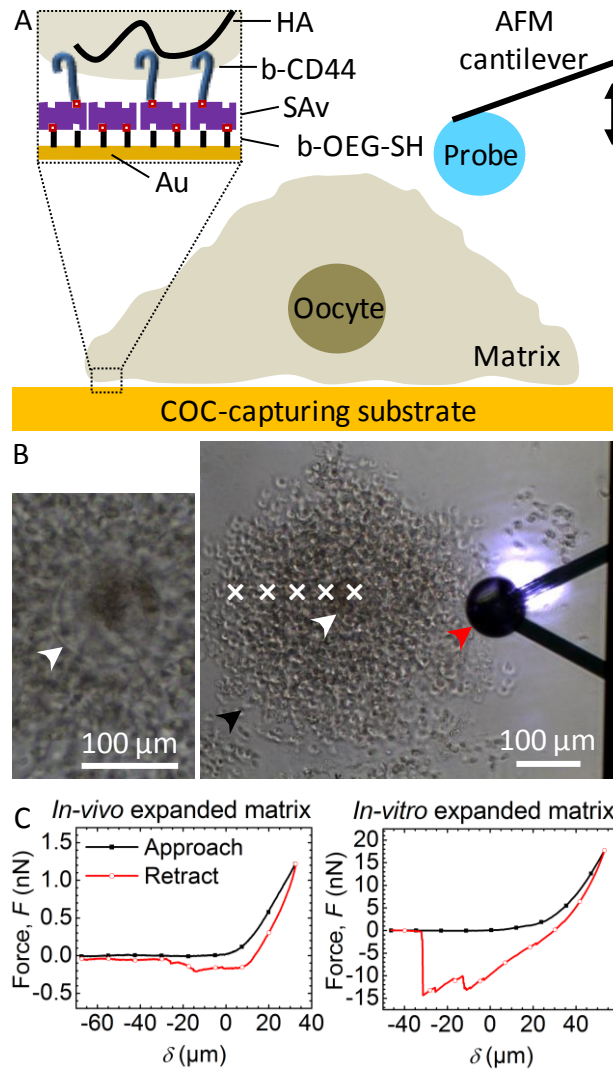
Figure II.1 (A) Scheme of the AFM force-indentation measurement setup. The inset illustrates the assembly of the COC-capturing surface. (B) Representative optical micrograph of the measurement setup (right). The red arrowhead marks the colloidal probe, attached to the V-shaped AFM cantilever and the chip (right; the shiny spot on the upper cantilever arm is the laser detecting cantilever deflection). Cumulus cells in the COC matrix (one is marked with a black arrowhead) and the oocyte (white arrowhead) are also visible. Force curves were acquired at locations labelled with white crosses, starting above the oocyte centre and interspaced by 50 μm. The left micrograph provides a magnified view of an oocyte, where the zona pellucida surrounding the oocyte, marked by a white arrowhead, can be identified. (C) Representative curves of force vs. distance from contact point δ, acquired upon approach to (black line with solid square symbols) and retraction from (red line with open circle symbols) in-vivo (left) and in-vitro (right) expanded COC matrices. δ was set to 0 at the contact point at approach, and positive distances correspond to sample indentation.

Representative force curves obtained upon indentation of an *in-vivo*, as well as an *in-vitro* expanded COC at a location on top of the oocyte are shown in Figure II.1*C*. The approach curve shows an extended baseline, where the colloidal probe was not in contact with the sample, followed by a monotonic increase in force reflecting the response of the COC matrix to compression. The length of the baseline was chosen to extend at least 40 μm to enable reliable determination of the contact point ($\delta = 0$), which was operationally defined as the position in the approach curve at which the force exceeded the baseline level by 50 pN. This threshold force is slightly above the instrument noise level.

Attractive features (*i.e.* negative force) were not observed in the approach curves, but they were always present in the retract curves. This reveals that some residual adhesion between the colloidal probe and the COC occurs despite passivation of the probe with BSA. It also implies that probe-sample adhesion must increase gradually in the course of the indentation process. The magnitude of the adhesion forces varied. *In-vivo* expanded COCs typically showed an adhesion of a few 100 pN, occasionally rising to values in the low nN range, while *in-vitro* expanded COCs displayed values in the range of 5 to 10 nN, or in some cases only a few 100 pN. The exact shape of the retract curves also varied from one measurement to the next, even on the same spot, and yielded multiple unbinding peaks. This indicates that the detachment of the matrix from the colloidal probe occurs stochastically in steps, and suggests that the COC matrix may be heterogeneous on the scale of the interaction area. Adhesion frequently persisted a few tens of μm beyond the contact point (Figure II.1*C*), indicating that the COC matrix can be stretched significantly. The overall shape and position of the COC matrix were not visibly affected during indentation or stretching with the colloidal AFM probe, as observed by optical microscopy. This confirmed that the COC matrix is stably immobilized thus enabling repeated and controlled indentations at well-defined positions.

II.3.2   COC matrix is an elastic material

To investigate the mechanical response of the COC matrix to applied force, we indented the matrix atop oocytes repeatedly and at various loading rates (Figure II.2). The shapes of approach curves obtained during the first and subsequent indentations at the same position on the COC matrix were virtually identical, for COCs expanded *in vivo* (Figure II.2*A*) as well as *in vitro* (Figure II.2*B*). Moreover, the distances of the

contact point from the glass substrate also remained unchanged. This indicates that the matrix fully recovers its original shape when the compressive force is released. In other words, COC deformation is elastic and not plastic.
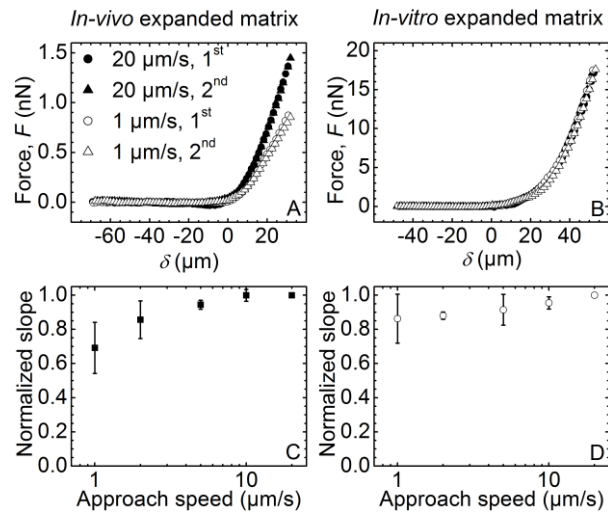
Figure II.2 Effects of compressive forces on indentation of COC matrix: elastic *vs.* plastic and viscous deformation. (*A-B*) Representative curves of force *vs.* distance from contact point δ, measured on COCs expanded *in vivo* (*A*) and *in vitro* (*B*). The first and second approach curves obtained at a previously unperturbed position on the COC are shown for two selected approach speeds (1 µm/s and 20 µm/s, as indicated). (*C-D*) Slopes measured between δ = 25 and 30 µm in series of force *vs.* distance curves acquired at fixed positions with varied approach speed, normalized by the slope at 20 µm/s. Data represent the mean ± standard deviation from measurements on 3 COCs each, expanded *in vivo* (*C*) and *in vitro* (*D*).

The force responses of *in vivo* expanded COC matrices were sensitive to the loading rate. For example, applying a more rapid rate of compression led to a marked increase in the force required to generate a given indentation (Figure II.2*A*). To analyze this dependence, the slopes of the force *vs.* distance curves at a selected indentation depth (25 µm < δ < 30 µm) were computed. As shown in Figure II.2*C*, the value was significantly lower at 1 µm/s (the lowest rate measured) compared to 20 µm/s (the highest rate measured). This suggests that there is a viscous component to the mechanical response. Interestingly, a plateau is observed at higher loading rates, indicating a transition from a viscoelastic to a purely elastic behavior around 5 µm/s. COC matrices expanded *in vitro* showed no significant loading rate dependence (Figure II.2*D*), indicating that this matrix remains purely elastic across the measured range.

II.3.3   Quantification of COC matrix elasticity

The Young´s modulus E of the COC matrix was determined from force (F) *vs.* indentation ($\delta > 0$) curves using the Hertz indentation model (158)

$$F = \frac{4}{3}\frac{E}{1-\mu^2}\sqrt{R\delta^3} \; ,$$ (Eq. 1)

where R represents the radius of spherical probe (45 µm) and µ is Poisson's ratio (159). Most materials have Poisson's ratio values ranging between 0 and 0.5 (160), and we fixed µ = 0.5 for simplicity. This implies that E will be underestimated by at most 25% depending on the exact value of µ. The simplified form of the Hertz model given in Eq. 1 assumes E to be much smaller than the Young's modulus of the probe (in the GPa range for polystyrene (151)), and R to be much smaller than the effective radius of the probed sample. Both conditions are met in our experiments (*vide infra*).

The Hertz model provided satisfactory fits when the first 10 µm of indentation were considered for analysis Figure II.3*A*, *solid line*). The resulting Young's modulus of matrix expanded *in vivo* was extremely low; an average from measurements atop the oocyte in 3 COCs gave $E = 0.5 \pm 0.1$ Pa. *In vitro* expanded COC matrices possessed values for Young's modulus ($E = 1.6 \pm 0.3$ Pa) that were several fold higher. Extrapolation of the fit (Figure II.3*A*, *dotted line*), however, revealed that the Hertz model does not adequately describe the experimental data at larger indentations. We considered several effects to explain this discrepancy.

First, the Hertz model requires the indentation depth to be small compared to the sample thickness (158). This is the case in our experiments (*vide infra*). Second, the maximal indentation depth in our experiment approached the radius of the indenter ($\delta \sim R$) whereas the Hertz model is strictly valid only for $\delta \ll R$. However, comparison with an improved model by Sneddon (203) shows that the Hertz model overestimates the force at a given indentation and fixed Young's modulus, the opposite to what is observed in the experiment (Figure II.3*A*). Moreover, the discrepancy between the two models remains below 10% for all $\delta < R$ (Supporting Figure II.S1), implying that the Hertz model provides a reasonable approximation even at the largest measured indentations. Third, the Hertz model assumes zero probe-sample adhesion. The absence of negative forces in the approach curves (Figure II.1*C*) indicated that adhesion was indeed virtually absent at small indentations in our experiments. The negative forces in the retract curves (Figure II.1*C*) revealed that adhesion develops gradually upon indentation, and this would affect the shape of the approach curve at larger indentations

in a way that is not properly accounted for in the Hertz model. However, a reduction in the force would be expected, again opposite to what is seen in Figure II.3*A*, and adhesive interactions therefore also cannot explain the discrepancy between the Hertz model and experiment.
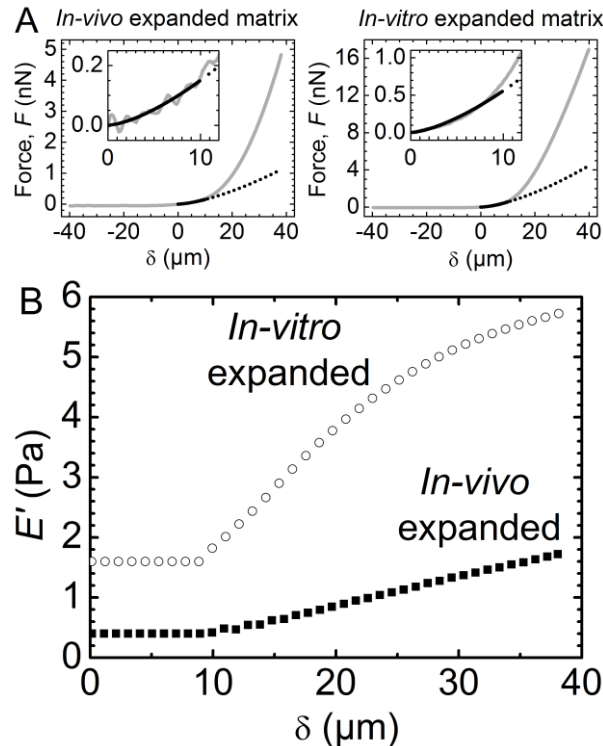
Figure II.3 Quantification of COC matrix elasticity. (*A*) Representative curves of force *vs.* distance from contact point δ, acquired on top of the oocyte centre of *in-vivo* (*left*) and *in-vitro* (*right*) expanded matrix (*grey solid lines*), fitted to the Hertz model over $0 \leq \delta \leq 10$ µm (*black solid line*) that yields values for Young´s modulus of 0.4 and 1.6 Pa, respectively. The *black dotted line* is an extrapolation of the fit, illustrating that the Hertz model does not reproduce data yielding large indentation values accurately, and that the matrix effectively stiffens upon compression. Data over $0 \leq \delta \leq 12$ µm are magnified (*insets*), to illustrate the quality of the fits. (*B*) Effective elastic moduli *E'* for a COC expanded *in vivo* (*solid squares*) and *in vitro* (*open circles*). The force curves in (*A*) were downsampled to reduce scatter and then used for analysis. For $0 \leq \delta \leq 10$ µm, *E'* was determined through a fit with Eq. 1; for $\delta > 10$ µm, *E'* was calculated with Eq. 2.

Ultimately, the Hertz model makes the important assumption that the probed material is isotropic and linearly elastic. The enhanced increase in the compression force with indentation observed in the experiment (Figure II.3*A*) thus would indicate that COC matrix effectively stiffens upon compression. We sought to obtain a more detailed

characterization of the matrix mechanical properties as a function of indentation. To this end, we define the elastic modulus E' by considering only the force F' at a given indentation depth $\delta = \delta' > 0$, but not the shape of the force curve between the contact point ($\delta = 0$) and δ', for the Hertz model analysis. From Eq. 1, we find

$$E' = \frac{3}{4}\left(1 - \mu^2\right)\frac{F'}{\sqrt{R\delta'^3}}\,. \tag{Eq. 2}$$

E' provides a simple quantification of matrix elasticity. For small indentations, *i.e.* in the linear elastic regime where the Hertz model reproduces the experimental data well, it is identical to the Young's modulus E. For large indentations, where the Hertz model deviates from the experimental data ($\delta > 10$ μm in our case), it represents a measure of non-linear elasticity. We note that the way in which non-linear effects influence the shape of the force *vs.* distance curves may depend in complex ways on the shape and size of the employed probe, as well as the internal organization of the matrix. In addition, the force curves at large compression are also likely to be affected by probe-sample adhesion (Supporting Figure II.S2). Therefore, we consider E' an effective measure of matrix elasticity in the non-linear elastic regime.

Figure II.3*B* shows the result of this analysis on representative force curves acquired in the central region above the oocytes. E' was a few fold higher for *in-vitro* expanded matrix (*open circles*) than for *in-vivo* expanded matrix (*solid squares*) irrespective of the indentation, and increased by a few fold over the accessible indentation range of 40 μm. Nonlinear effects were appreciable and more pronounced for *in-vitro* expanded matrix.

II.3.4 Quantification of COC matrix extension

Because the HA-rich matrix is not directly visible by optical microscopy, the distribution of cumulus cells is commonly used as an indirect measure for COC matrix extension. In our assay, the contact point determined through indentation measurements provided an alternative measure for matrix extension. Interestingly, our finding that these two measures differ indicates that the COC features an extended outer matrix layer that is essentially free of cumulus cells – a novel and unexpected feature that has not been described previously. Specifically, we defined the 'mechanical height', H_{mech}, as the distance between the point of contact on the COC and the glass surface, which was determined from the combined motion of the AFM's z piezo and stepper motor to an accuracy of approximately 10 μm. The 'optical height', H_{opt}, on the other hand was determined as the objective travel required for moving the optical focus from the glass

substrate to the outermost cumulus cells (multiplied by $n_{liquid}/n_{air} = 1.334$, to correct for the effect of the refractive index change between aqueous solution and air on the focusing). We estimate a resolution of 30 μm for this parameter, based on the accuracy of the focusing itself and the manual readout of the focus travel position. This is much less than the dimensions of the COC and thus provided measurements with good accuracy.
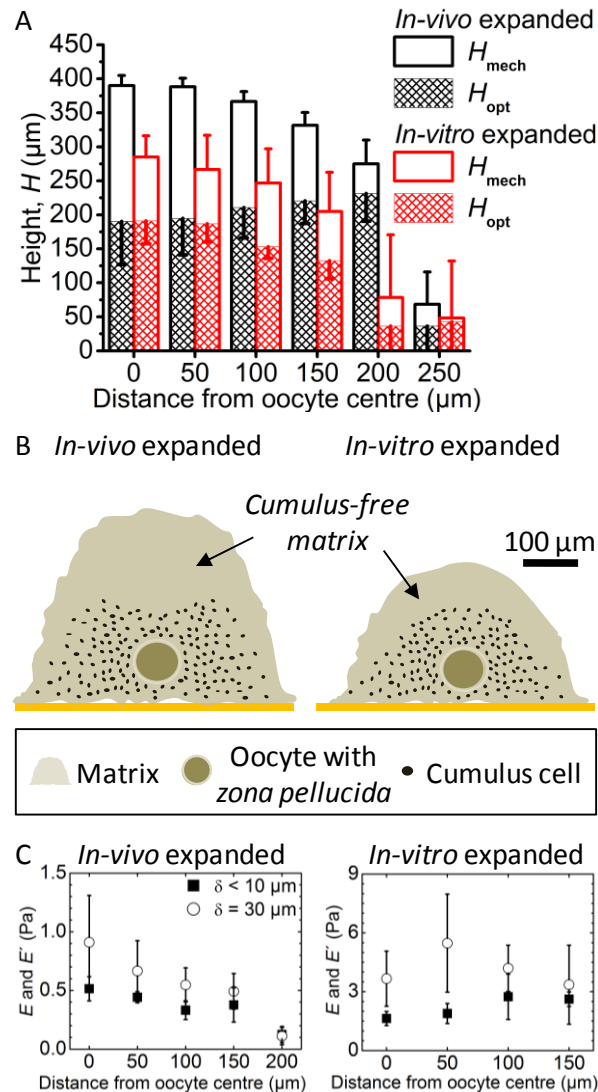
Figure II.4 Determination of COC dimensions. (*A*) Heights, H_{mech} (determined mechanically from the contact point) and H_{opt} (determined optically from the location of the topmost cumulus cells), as a function of the distance from the oocyte centre. Data represent mean and standard deviations from measurements on 3 COCs; error bars are drawn along one direction only to facilitate visualization. (*B*) Illustration of the approximate dimensions of the COC matrix and the location of cumulus cells within it, as determined from the spatial mapping of H_{mech} and H_{opt}. The height of the oocyte

above the substrate was determined optically. Oocyte and cumulus cell sizes are drawn to scale. (*C*) Elasticity of COCs expanded *in vivo* (*left*) and *in vitro* (*right*) as a function of distance from the oocyte centre. Young's moduli in the linear elastic regime (*solid squares*) as determined through a fit with Eq. 1 for $\delta < 10$ μm; elastic moduli at $\delta = 30$ μm (*open circles*) were calculated with Eq. 2. Data represent the mean ± standard deviation from measurements on 3 individual COCs, except at 200 μm where only 2 of 3 *in-vivo* expanded COCs had a matrix and were analyzed.

Figure II.4*A* shows that the part of the matrix containing the oocyte and the cumulus cells is approximately 200 μm thick, independent of the method used for matrix expansion. Remarkably, the optically invisible cell-free coat contributes appreciably to the total coat extension. For *in-vivo* expanded matrix, it adds another 200 μm to the total thickness. For *in-vitro* expansion, the cell-free coat remains appreciable but its thickness reduces by 50%, indicating that factors in the follicle that are not present *in vitro* might play an important role in the formation of this part of the matrix.

To map the dimensions of the COC matrix laterally, H_{mech} and H_{opt} were measured as a function of the distance from the oocyte centre. These results are also shown in Figure II.4*A*, and summarized in Figure II.4*B* in which the results of the correlative analysis of micromechanical and optical data are reflected in schemes that depict the extensions of the cumulus-containing and the cumulus-free parts of matrix, the oocyte and the cumulus cells drawn to scale. The sharp drops in H_{mech} and H_{opt} between 200 and 250 μm distance for *in-vivo* expanded matrix, and between 150 and 200 μm distance for *in-vitro* expanded matrix, indicate that the lateral extension of the coat is not diffuse but clearly delimited and that the cell-free coat lining the immobilized COC matrix laterally is very thin. Moreover, we found no significant cumulus free layer separating the substrate from the cumulus-containing matrix. At first, the asymmetric distribution of the cell-free coat – thick on the substrate-distal face, thin on the sides and virtually absent on the substrate-proximal face of the COC – was surprising, as we expected the unperturbed COC matrix to have roughly spherical symmetry. We reasoned that COC immobilization somehow entails deformation of the cumulus-free matrix in the vicinity of the substrate. Apparently, the multivalent binding between HA in the matrix and CD44 on the substrate (Figure II.1*A*, *inset*), possibly in conjunction with the gravitational forces exerted by the COC as a whole, are sufficiently strong to promote collapse of the extremely soft substrate-proximal matrix. We also noticed that H_{opt}

measured across the oocyte (200 μm) was smaller than the lateral extension of the cumulus-containing matrix (400 to 500 μm for *in-vivo* expanded matrix, and 300 to 400 μm for *in-vitro* expanded matrix), and that the lateral diameter of the *zona pellucida* in immobilized COCs (~110 μm; Figure II.1*B*, *left*) was larger than what is typically observed in free-floating COCs (~80 μm (204)). This suggests that immobilization also deforms the cumulus-containing part of the matrix as well as the oocyte-surrounding *zona pellucida*, though only moderately and to a much lesser extent than the cumulus-free substrate-proximal parts. On the other hand, the thickness of the cumulus-free substrate-distal part of the matrix (indicated by the length of the open bars in Figure II.4*A*) was essentially constant within 150 μm from the oocyte center for *in-vitro* expanded matrices and within 100 μm for *in-vivo* expanded matrices, suggesting that this part of the matrix is largely unperturbed by the immobilization although its apparent thickness could possibly be modified slightly by lateral matrix stretching upon immobilization or by gravity acting on the cells.

To test the homogeneity of the COC matrix, we analyzed force curves taken between 0 and 150 μm from the oocyte centre (as well as 200 μm for *in-vivo* expanded matrix), *i.e.* distances for which a matrix was clearly present (Figure II.4*A*), at a selected loading rate (20 µm/s). Figure II.4*C* shows that both the Young's modulus in the linear elastic regime ($\delta < 10$ μm; *solid squares*) and the effective modulus in the nonlinear elastic regime at a selected indentation ($\delta = 30$ μm; *open circles*) are virtually constant across the COC matrix, for matrices expanded *in vivo* as well as *in vitro*. This suggests that the matrix is homogeneous, and that the presumably stiffer oocyte does not affect the measurements appreciably, consistent with expectations (205) based on the small indentation depths used compared to total matrix thickness ($< 20\%$). The decrease in E and E' at 200 μm for *in-vivo* expanded matrix (Figure II.4*C*, *left*) appears to be an outlier. Figure II.4*A* shows that the COC thickness decreases rapidly beyond 200 μm from the oocyte center. The measurements at the COC periphery are thus most likely performed on a strongly tilted COC-solution interface, and we propose that this effectively reduces the elastic modulus.

II.4   DISCUSSION

We have determined the most compliant parts of mouse COC matrix to have a Young's modulus below 1 Pa, and the effective elastic modulus to remain at a level of a few Pa across the range of strains tested (up to about 10%; Figure II.3). Considering all

possible systematic errors described above, we estimate the modulus values to be accurate to within a factor of two. To our knowledge, this is the lowest elastic modulus thus far determined for any mammalian tissue (206). By comparison, brain which is typically considered one of the softest tissues, has a value for Young's modulus that is approximately two orders of magnitudes higher than that of COC matrix (122). The hyaluronan-rich glycocalyx lining the blood vessel endothelium is also considered very soft, and a Young's modulus in the range of a few 100 Pa has been reported on bovine lung microvascular endothelial cells (123). Among the larger animal kingdom, even the mostly acellular mesoglea of the jellyfish has local elastic modulus values that range between a few 10 Pa and a few 100 Pa (198). Furthermore, as reported by Velegol and Lanni (207), collagen gels formed *in vitro* at 0.5 mg/mL are predominantly elastic with local elastic modulus values in the range of 1 Pa, we ourselves found films reconstituted from hyaluronan and the matrix proteoglycan aggrecan (at 4 mg/mL total concentration) to exhibit a Young's modulus of a few 10 Pa (29), and others reported predominantly elastic macroscopic hydrogels containing chemically cross-linked hyaluronan with values of Young's modulus below 100 Pa (117, 118, 129), thus demonstrating that materials reconstituted from matrix molecules can also be very soft. Taken together, these comparisons illustrate that COC matrix is extremely soft, and most likely the predominantly elastic biological material with the lowest elastic modulus known to date.

To our knowledge, only a single study has hitherto reported a quantitative analysis of COC elasticity. Dunn and Picologlou (195) stretched entire COCs by between 15 and 400% of the extension at rest, and found a linear elastic response over the entire stretching range, with a Young's modulus of 150 Pa. In marked contrast, the value for Young's modulus that we report in the present work is 2 to 3 orders of magnitude smaller and our data showed that the COC matrix stiffens appreciably even at a few per cent compression (Figure II.3). The discrepancy suggests that the two measurements provide distinct information about COC matrix mechanics. On one hand, our AFM-based micromechanical method is particularly sensitive to the cumulus-free soft outer shell of the COC. In the macromechanical approach of Dunn and Picologlou, on the other hand, the deformation of the inner and more rigid cumulus-containing part is monitored and the cumulus-free shell is largely neglected. The two methods thus are complementary, providing information about distinct parts of the COC matrix. We note that Dunn and Picologlou studied rabbit COCs that were expanded *in vivo* but extracted before ovulation, whereas our COCs were isolated from mice and were either expanded

in vivo and extracted after ovulation, or expanded *in vitro*. The differences in the animal source and COC preparation might also contribute to the distinct results observed by us and others. Future studies combining our micromechanical testing with frozen-cut COC sections should reveal valuable details about the mechanical heterogeneity of the COC matrix and the micromechanics of the inner parts of the COC matrix.

Previous studies have suggested that the COC matrix is a mesh-like network (109), that is, effectively a cross-linked hydrogel. Here, we found that even the softest and peripheral parts of COC matrix are predominantly elastic (Figure II.2). This extends previous findings and indicates that the COC matrix is stably cross-linked throughout. It has previously been demonstrated that hyaluronan together with the proteins TSG-6 (191) and pentraxin 3 (PTX3) (83) as well as the proteoglycan inter-α-inhibitor (IαI) (190, 192) are essential for the stabilization of COC matrix, and sufficient to form a cross-linked hydrogel (28). The exact molecular nature of the cross-links, however, remains unknown. The elasticity of the COC matrix in our assays reveals that the cross-links are sufficiently stable to resist breakage on the time scale of seconds and minutes. The measured Young's modulus can provide a first estimate of the mesh size of the COC matrix. Specifically, for a homogeneous polymer meshwork that is dominated by cross-links, the so-called correlation length ξ (a statistical measure of the distance between segments on neighboring chains, or the effective mesh size) can be extracted approximately from $G \approx kT/\xi^3$, where G represents the so-called plateau shear modulus, and $kT = 4.1 \times 10^{-21}$ J is the thermal energy (175). From $E = 2G(1 + \mu)$ and $E < 1$ Pa, we can estimate that the effective mesh size is on the order of a few 100 nm, *i.e.* the softest parts of the COC matrix are likely to be very sparsely cross-linked. This value is comparable to the correlation length reported for chondrocyte pericellular matrix (PCM) based on optical force probe and particle exclusion assays (124). The PCM, like the COC matrix, is rich in hyaluronan. However, the PCM's overall topology must be distinct from the COC matrix because its mechanical stability is not provided by cross-links but by the tethering of long hyaluronan chains to the cell wall (124).

Interestingly, the mechanical response of *in-vivo* expanded COCs contains an appreciable viscous contribution at low (< 5 µm/s) but not at high (> 5 µm/s) approach speeds (Figure II.2*C*). The drainage of liquid through the hydrogel pores during compression is a possible source of viscosity. Can poroelasticity explain our experimental observation? In a scaling approximation, the time scale associated with the

liquid movement (the poroelastic time) is $t_p \approx L^2/D_p$, where L is the length scale associated with the indentation ($L^2 \approx R\delta$ for a spherical indenter (208)) and D_p is the poroelastic diffusion constant ($D_p \approx E_d\xi^2/\eta$, where E_d is the drained elastic modulus of the hydrogel matrix and η is the viscosity of the draining solution) (209). With the above scaling approximation for the correlation length ξ and $E_d = 2G_d(1+\mu)$, this gives $t_p \approx R\delta\eta/\{E_d^{1/3}[2kT(1+\mu)]^{2/3}\}$. The drained elastic modulus is a lower limit of the measured value of Young's modulus ($E_d \leq E < 1$ Pa), and with $\eta \geq \eta_{water} \approx 1$ mPa·s and $\mu \leq 0.5$ we find $t_p \gtrsim 0.8$ s × δ/μm. For comparison, the experimental compression time is $t_c \approx \delta/v_c$. Thus, $t_p/t_c \gtrsim 0.8$ at the lowest approach speed ($v_c = 1$ μm/s), indicating that t_p and t_c may well be comparable and that the appreciable viscous responses at lower speeds arise from liquid drainage through the COC matrix. At the highest speed (20 μm/s), however, t_p is much larger than t_c, such that draining becomes negligible. The values of Young's modulus determined at higher speeds, therefore, represent the elasticity of the un-drained matrix.

The clear segregation into a cumulus cell-containing inner part and a cumulus cell-free outer shell (Figure II.4), as well as its marked stiffening in response to stress (Figure II.3), indicate that the COC matrix is not a homogeneous structure. Specifically, the mechanical properties of COC matrix suggest a heterogeneous network structure in which mesh size increases with distance from the oocyte perimeter. Future studies that measure the permeability of the COC matrix directly with probes of different size should be useful in defining the sieving properties and the fine structure of the COC matrix in more detail. In particular, it will be interesting to test if the COC matrix exhibits a gradient of mesh size distribution similar to what was reported for the chondrocyte PCM (124) despite the distinct topologies of these two hyaluronan meshworks.

What are the functional implications of the COC matrix' mechanical properties and ultrastructure? An essential step in the reproductive process is the transport of the ovulated COC along the ciliated oviduct, and pickup and transport of the COC are tightly regulated by an interplay of mechanical and adhesive cues (51). It is clear that the COC matrix, and in particular the outer cumulus cell-free layer, is extremely deformable. Matrix size and shape can vary in a large range upon applied force, but the original shape is fully restored once the mechanical perturbation is released (Figure II.2*A-B*). This should ensure the COC's structural and functional integrity throughout its transport through the narrow oviduct. Moreover, the large size and the extreme softness

of the COC matrix' outer shell might be a crucial ingredient for efficient capture and subsequent transport by the beating cilia that line the oviduct. Additionally, it is increasingly apparent that biological hydrogels function as selective diffusion barriers, where both the physical constraints imposed by the hydrogel's mesh size and specific interactions with the hydrogel's scaffold regulate macromolecular transport (210). In this regard, it is possible that the heterogeneity of the COC matrix provides spatio-temporal control over storage and access to signaling molecules and enzymes that are of critical importance for proper oocyte development and fertilization. Given the large mesh size of the HA matrix, physical constraints are probably of minor importance for the distribution of such proteins. However, signaling proteins are known to bind to matrix components such as the glycosaminoglycan chains on the proteoglycan versican, and heterogeneities in the biochemical environment may thus produce strong effects.

In this study, we have defined for the first time a thick and soft matrix coat surrounding the COC that is essentially free of cumulus cells (Figure II.4) – an unexpected feature that has not been reported previously. Remarkably, the coat is much less pronounced around *in-vitro* expanded matrix, indicating that the *in vivo* environment provides unique cues that enable the formation of the cell free coat. Likely antral granulosa cells, lining the antrum of the preovulatory follicle, contribute to this difference. Indeed, these cells produce hyaluronan which likely becomes incorporated in the cumulus matrix (85). In addition, granulosa cells produce the proteoglycan versican, and versican binding to hyaluronan may well enhance the swelling of the outer coat (211). At this point, we can only speculate about the biological role of the cumulus cell-free coat. Early *in vitro* work (212) indicated that sperm recognize the interfacial zone of COC matrix and respond by changes in their orientation and in the beating pattern of their flagella. Moreover, a subpopulation of weakly motile sperm would not be capable of penetrating into the matrix. This raises the possibility that the additional coat discovered here is not only important for capture and transport of the ovum through the oviduct, but that it also plays a role in the selection, capture and guidance of sperm during fertilization. Clearly, there is a potential for comparative studies of sperm interaction with *in-vivo* and *in-vitro* expanded COCs to provide further understanding of the initiation of sperm penetration and to improve the efficiency of *in-vitro* fertilization procedures. Moreover, comparative micromechanical studies of *in-vivo* and *in-vitro* expanded COCs may help optimize oocyte IVM, a technique widely applied for the breeding of agriculturally important species and proposed as an alternative treatment in

human assisted reproduction technology to circumvent the drawbacks of standard ovarian stimulation regimens (213).

II.5   CONCLUSION

We have successfully quantified the micromechanical response of COC matrix to compression by colloidal probe AFM. Owing to the nature of the COC matrix, it was necessary for us to develop a tailored immobilization procedure and to adapt the size of the colloidal probe. The matrix was confirmed to be elastic rather than plastic or viscous. Salient features of the COC compressive mechanics are an extreme degree of softness and a marked tendency to stiffen under stress. Through the combination of mechanical and optical analysis, we could identify the presence of a thick cumulus free coat that is particularly pronounced around *in-vivo* expanded matrix. The COC matrix heterogeneity and the unique combination of elasticity and extreme softness may be functionally important, in particular for the maintenance of COC integrity during transport through the oviduct and for the proper selection, capture and guidance of sperm. The methods we have established should also be valuable for characterization of hyaluronan-rich matrices in a wide range of other cells and tissues.

II.6   SUPPORTING MATERIAL
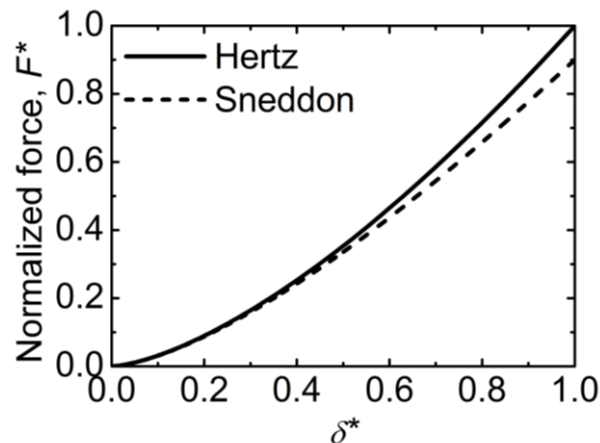
Figure II.S1 Comparison of the Hertz model (*solid line*) (158) with the Sneddon model (*dashed line*) (203). The latter is more accurate at large indentation, because it properly considers sample deformation (214). Predictions are shown in terms of normalized force, $F^* = F/(4R^2E/3(1-\mu^2))$, *vs.* normalized indentation, $\delta^* = \delta/R > 0$. At any given indentation and fixed Young's modulus, the Hertz model overestimates the force, and

this effect increases with δ approaching R. However, the discrepancy between the two models remains small, i.e. below 10%, for all $\delta \leq R$.
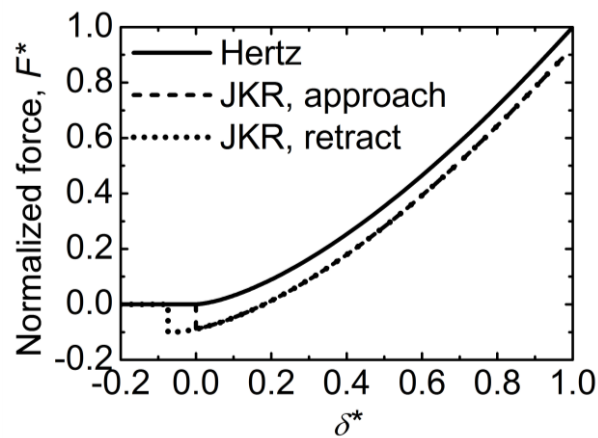
Figure II.S2 Comparison of the Hertz model (*solid line*; approach and retract curves are identical) with the Johnson-Kendall-Roberts (JKR) model (approach curve - *dashed line*, retract curve - *dotted line*) (157) which includes the effect of adhesion forces (215). Predictions are shown in terms of normalized force F^* *vs.* normalized distance from contact point at approach δ^*, assuming a normalized adhesion force of $F^*_{ad} = 0.1$. In the presence of adhesion, a jump in the force curve at negative indentation is expected. This feature was found in the experimental retract curves but not in the approach curves (Fig. 1*C*), indicating that adhesion established gradually as the colloidal probe indented the sample. The Hertz model therefore is expected to provide a reliable measure of the Young's modulus at small indentations (where adhesion is weak) and to underestimate the elastic modulus E' at large indentations (where adhesion is sizeable). The magnitude of the adhesion force observed in our experimental retract curves was typically smaller than the magnitude of the compression force at largest indentation. Based on a numerical comparison of Hertz model and JKR model, one can show that, under this condition, E' is underestimated by less than 43%.

III Mechanical and structural properties of *in-vitro* reconstituted HA brushes

The research work presented in this chapter is in preparation as a manuscript, for submission to a peer reviewed journal, as:

Effect of calcium ions and pH on the morphology and mechanical properties of hyaluronan brushes

Xinyue Chen,[1,2] and Ralf P. Richter[1,2,3]

[1] CIC biomaGUNE, San Sebastian, Spain; [2] Max-Planck-Institute for Intelligent Systems, Stuttgart, Germany; [3] University Grenoble Alpes - CNRS, Laboratory of Interdisciplinary Physics (LIPhy), Grenoble, France.

My contribution: I co-designed research (together with Ralf P. Richter) and performed all experiments (in particular RICM and QCM-D measurements). I analysed and interpreted the data (together with Ralf P. Richter). I prepared all figures and wrote the first draft of the manuscript, as well as contributed to subsequent revisions.

Abstract: Hyaluronan (HA) is a linear, unbranched polysaccharide composed of repeated disaccharide units. Playing as one of the chief components in peri- and extracellular matrices, HA contributes significantly to many basic cellular processes. Typically, the biological activity of HA is supported by the physico-chemical properties of the supramolecular assemblies that it makes. To understand more comprehensively the response of the supramolecular organization of HA polymers to changes in their aqueous environment, we study the effects of Ca^{2+} concentration and pH on the morphology and viscoelasticity of films of end-grafted HA polymers on planar supports (HA brushes), as a well-defined *in vitro* model system of HA-rich matrices, by reflection interference contrast microscopy (RICM) and quartz crystal microbalance with dissipation monitoring (QCM-D). Our results reveal that both the thickness and softness of HA brushes decrease significantly with Ca^{2+} concentration but do not change with pH within the physiological ranges of these parameters. By studying a large range of Ca^{2+} concentrations, we discovered that the effect of Ca^{2+} on HA brush thickness is virtually identical to the effect of Na^+ at 10-fold higher concentrations. Moreover, the thickness and softness of HA brushes decreases appreciably upon protonation of HA at pH values below 6. Importantly, effects of pH and calcium ions are fully reversible over large parameter ranges. These findings are relevant for understanding the supramolecular organization and dynamics of HA-rich matrices in biological systems and potentially will also benefit the rational design of synthetic HA-rich materials with tailored properties.

III.1 INTRODUCTION

As a chief component of extracellular matrix (ECM), hyaluronan (HA) is ubiquitous in the extracellular space of vertebrates and plays various biological roles. It is a linear, unbranched polysaccharide composed of identical disaccharide units containing glucuronic acid and N-acetylglucosamine (11). Each disaccharide, which is 1.0 nm long (13), carries one chargeable carboxylic group. The pK_a of polymeric HA is approximately 3, which implies that HA is negatively charged at physiological pH (14).

Cells use HA synthases (HASs) in the plasma membrane to synthesize HA and extrude it into the extracellular space (18). HA molecules thus produced can reach a very high molecular weight, up to millions of Daltons (11). HA can either be released into the extracellular space, or remain grafted to the cell surface via HASs (18) or otherwise attached through HA receptors, such as CD44 (23), to form so-called pericellular coats (PCCs). HA-rich PCCs fulfil crucial functions in basic cellular processes such as proliferation and migration (31), intercellular adhesion (32), and mechanosensing (54). To modulate these functions, the morphology and physical properties of HA-rich PCCs are remodelled by changes in the extracellular environment. HA-binding proteins, for example, can induce condensation and rigidification (by cross-linking, such as with the inflammation-associated protein TSG-6 (26)) or swelling of HA-rich matrices (by intercalation of swollen proteoglycans such as aggrecan (29, 33)). On a more basic level, the physico-chemical properties of the aqueous solution such as pH and ionic strength also affect the properties of the HA and the assemblies that it forms. This is not only relevant for the function of HA-rich matrices around cells and in biological tissues, where changes in salt concentration and pH have been found to modulate HA-related functions (216-219). Over the past decade, artificial HA-rich matrices (116) and surface coatings (220) have also become popular in bioengineering research. A good knowledge of the effect of pH and salts on the ultra-structure and mechanical properties of HA-rich matrices is thus also important for technological applications. Previous studies focussing on HA solutions have shown that besides monovalent cations such as sodium (221, 222), divalent calcium ions and pH also modulate the molecular structure and viscoelasticity of HA (126-128, 223-226). In biological and synthetic materials, however, HA is confined by cross-linking (in hydrogels) or by grafting or adsorption (in interfacial films), and there is still very

limited information about the impact of environmental conditions such as pH and salts on such supramolecular HA assemblies.

Here, we study the effect of environmental conditions on films of HA polymers that are grafted via their reducing end to a planar rigid support (Figure III.1*A*). These films are less complex than native PCCs yet they reproduce salient features such as the confinement of HA to a surface, the density of HA in PCCs and the typical thickness of PCCs. Moreover, they are well defined in that the molecular weight and arrangement of HA are tightly controlled. This enables highly quantitative studies and correlation with polymer physics theory that would not be possible with native PCCs. If the surface density of HA is high enough, then repulsion between neighbouring HA chains induces their stretching away from the surface and the films thus formed are adequately described as regular polyelectrolyte brushes. In previous work, we quantified the mechanical properties of such HA brushes at physiological ionic strength and pH (130), and also how the monovalent salt NaCl affects HA brush morphology and mechanical properties (20). The latter study, in particular, revealed how the strong charge and the intrinsic stiffness of HA lead to brush properties that are distinct from those observed for synthetic polyelectrolytes. In the present study, we employ two surface-sensitive analysis techniques, reflection interference contrast microscopy (RICM) and quartz crystal microbalance with dissipation monitoring (QCM-D), to quantify the effects of calcium ions and pH on the thickness and softness of HA brushes systematically over an extensive parameter range, that is, calcium concentrations between 1 μM and 1 M, and pH values between 1.0 and 9.0. The study sheds light on the effect of calcium and pH on the supramolecular organization and physical properties of surface-confined HA chains and highlights HA to be exquisitely responsive to these stimuli, both in terms of the magnitude and the reversibility of the response.

III.2 EXPERIMENTAL SECTION

III.2.1 Materials

The oligo-ethylene glycol (OEG) solution was a mixture of 99% of 1 mM OEG thiol (M_w 386.5 Da) and 1% of 1 mM biotinylated OEG thiol (788 Da; both from Polypure, Oslo, Norway) in synthesis grade ethanol, stored in the dark at 4 °C. Lyophilized streptavidin (SAv; 60 kDa; Sigma-Aldrich) was dissolved in ultrapure water. The stock solution at 1 mg/mL was stored as aliquots at -20 °C. Before each measurement, the

SAv stock solution was centrifuged at 10,000 rpm and 4 °C for 10 min. Lyophilized hyaluronan, biotinylated at its reducing end (b-HA) and with well-defined molecular masses of 280 ± 14 kDa (Select-HA B250) and 58 ± 3 kDa (Select-HA B50), as well as nonbiotinylated HA of 237 ± 12 kDa (Select-HA 250), were purchased from Hyalose (Oklahoma City, USA). HA was suspended in ultrapure water at 1 mg/mL (HA) or 0.5 mg/mL (b-HA), gently shaken at 4 °C for 2 h for reconstitution, stored at -20 °C, and used within one week after thawing.

All buffer and salt solutions were prepared in ultrapure water (resistance 18.2 MΩ/cm), and degassed before use. The sample preparation buffer contained 10 mM HEPES and 150 mM NaCl at pH 7.4. NaCl and $CaCl_2 \cdot 2H_2O$ were from Sigma Aldrich. Potassium phosphate solutions with pH values ranging from 9.0 to 5.0 were prepared by mixing desired ratios of stock solutions, 100 mM KH_2PO_4 (Sigma Aldrich) and 50 mM K_2HPO_4 (Fluka, Germany), prior to use. The potassium phosphate solution with pH 5.0 was further titrated by concentrated HCl (37%, reagent grade; Scharlab, Spain) to obtain solutions with pH values down to 1.0.

Polystyrene microspheres with 23.7 ± 1.5 μm diameter (Polysciences, Hirschberg, Germany) were washed in ethanol and ultrapure water, and stored at 4 °C in ultrapure water.

III.2.2 Preparation of substrates

Glass cover slips (#1.5, 24 × 24 mm^2; Menzel Gläser, Germany) were gently wiped by lint-free tissue (Kimtech Science, Surrey, UK) and blow-cleaned with N_2 gas before immersion in freshly prepared piranha solution composed of concentrated H_2SO_4 (95% to 98%; Scharlab, Spain) and H_2O_2 (50%; Scharlab, Spain) at a volume ratio of 3:1 for 3 h, thoroughly rinsed with ultrapure water, blow-dried with N_2 gas and stored in sealed petri dishes. To obtain gold (Au) coated substrates, clean glass cover slips underwent 10 min plasma cleaning in the vacuum chamber of the magnetron sputter system (ATC 1800 UHV; AJA International, Scituate, MA) before deposition of an adhesive titanium (Ti; 0.5 nm) and a 5 nm Au layer. The layer thickness was determined from the deposition rate which was calibrated by spectroscopic ellipsometry on reference silicon wafers. Au-coated QCM-D sensors (QSX301; Biolin Scientific, Västra Frölunda, Sweden) were rinsed with ethanol and ultrapure water and blow-dried with N_2 gas. UV-ozone treatment (ProCleaner; Bioforce Nanoscience, Ames, IA) was applied for 30 min to all substrates prior to their further use.

III.2.3 Preparation of HA brushes

Cleaned gold-coated substrates were immersed in OEG solution overnight, rinsed by ethanol and ultrapure water, blow-dried with N_2 gas, installed in fluidic devices for QCM-D and RICM, and covered with sample preparation buffer. The surfaces were then sequentially exposed to SAv (20 µg/mL for 30 min) and b-HA (5 µg/mL for QCM-D and 20 µg/mL for RICM, both for 2 h) in sample preparation buffer, with each incubation step followed by abundant rinsing to remove excess molecules from the solution phase.

III.2.4 Quartz crystal microbalance with dissipation monitoring

QCM-D measures the changes in resonance frequency, Δf, and dissipation, ΔD, of a sensor crystal upon molecular binding and reorganization events on its surface. The QCM-D response is sensitive to the mass (including hydrodynamically coupled water) and the mechanical properties of the surface-bound layer. Measurements were performed with a Q-Sense E4 system (Biolin Scientific) in flow mode (5 to 20 µL/min, adjusted with a syringe pump; KD Scientific, Holliston, MA) at a working temperature of 24 °C on Au-coated QCM-D sensors with an OEG monolayer. Changes in frequency (Δf_i) and dissipation (ΔD_i) were collected at 6 overtones (i = 3, 5, 7, 9, 11, 13, corresponding to resonance frequencies of $f_i \approx$ 15, 25, 35, 45, 55, 65 MHz); for simplicity, only selected overtones (i = 3, 7, 11) are presented. As controls, measurements were also performed on surfaces covered by SAv, with or without 10 µg/mL of non-biotinylated HA in the ambient solution.

III.2.5 Reflection interference contrast microscopy

For RICM, we used fluidic chambers in the form of cylindrical open cuvettes (5 mm diameter) made from a tailored Teflon holder and a glass cover slip at the bottom, glued together with two-component glue (Twinsil; Picodent, Germany). Cuvettes were used with a liquid volume of 50 µL. Samples were injected and the solution rapidly homogenized with a pipette. Samples were removed from the solution phase by repeated dilution and aspiration of the cuvette content until a concentration reduction of at least 10^5 fold was reached. Care was taken to keep the glass cover slip wet throughout all solution exchanges. A separate cuvette was used to test for the effect of each salt ($CaCl_2$ or NaCl) concentration or pH on HA brush thickness. Polystyrene microspheres for RICM analysis were added 15 min after incubation of a given test solution.

Interferographs were obtained with an inverted microscope (Axio Observer Z1; Zeiss, Oberkochen, Germany) in epi-illumination reflection mode, using a XBO xenon short-arc lamp as light source, an antiflex oil immersion objective (EC Plan Neofluar Antiflex 63×/1.25; Zeiss) and a filter cube with two crossed polarizers (AHF Analysentechnik, Germany).(169) The reflected light passed through a custom-built beam splitter unit(130) with band pass filters which in combination with two CCD cameras (ORCA-ER; Hamamatsu Photonics, France) permitted simultaneous acquisition of interferographs at wavelengths $\lambda = 630$ nm, 546 nm and 490 nm. The opening of the aperture diaphragm was reduced to its minimum throughout all measurements.

To quantify the distance between the polystyrene sphere and the substrate surface, we adapted a previously established algorithm implemented in Matlab (130). Briefly, the method is based on the determination of the position of extrema in the radial intensity profile of interferographs (169), and has an estimated accuracy of $\pm$ 5 nm. The method was here adapted to account for the presence of the metallic coating and the OEG and SAv layers, and the revised method includes reference measurements on bare Au-coated substrates, and on substrates coated with OEG and SAv monolayers (see Supplementary Methods and Figure III.S1). Unless otherwise stated, 10 polystyrene beads were analyzed per sample, and mean distances $\pm$ standard deviation were used for further analysis.

III.3   RESULTS

III.3.1   Assembly of HA brushes

Hyaluronan brushes were formed, as schematically shown in Figure III.1*A*, by grafting of HA with well-defined molecular weight (280 $\pm$ 14 kDa) via a biotin at the reducing end to a monolayer of streptavidin supported by a biotinylated thiol-OEG-monolayer on gold. This approach has been established previously (26, 144). Quartz crystal microbalance with dissipation monitoring (QCM-D) was used to follow the main assembly steps (Figure III.1*B*). To a first approximation, a decrease in frequency shift Δf indicates an increase in the surface-bound mass (including hydrodynamically coupled water), whereas the dissipation shift ΔD reflects the softness of the surface-associated film (144).

The frequency and dissipation shifts upon SAv injection (Figure III.1B, 40 to 70 min; final shifts $\Delta f_3/3$ = -24 ± 1 Hz and ΔD_3 = 0.2 ± 0.2 10^{-6}) were in good agreement with previous studies (26), and confirm the formation of a dense and stably anchored SAv monolayer. Subsequent incubation with biotinylated HA (Figure III.1B, 90 to 210 min) led to an additional decrease in the normalized frequency shift ($\Delta f_3/3$ = -9 ± 1 Hz) and a large increase in dissipation (ΔD_3 = 9 ± 1 × 10^{-6}). The latter observation, together with significant spreading of the responses between different overtones, is consistent with the formation of a highly hydrated and soft film, as expected for HA brushes (29). The rate of frequency and dissipation changes gradually decreased with progressing b-HA incubation time and virtually stabilized after 2 h; these responses are consistent with the formation of a polyelectrolyte brush, where the HA film increasingly hampers penetration and surface-binding of new molecules as it becomes denser. HA molecules were also stably grafted as demonstrated by the lack of response upon rinsing with buffer (Figure III.1B; beyond 210 min).
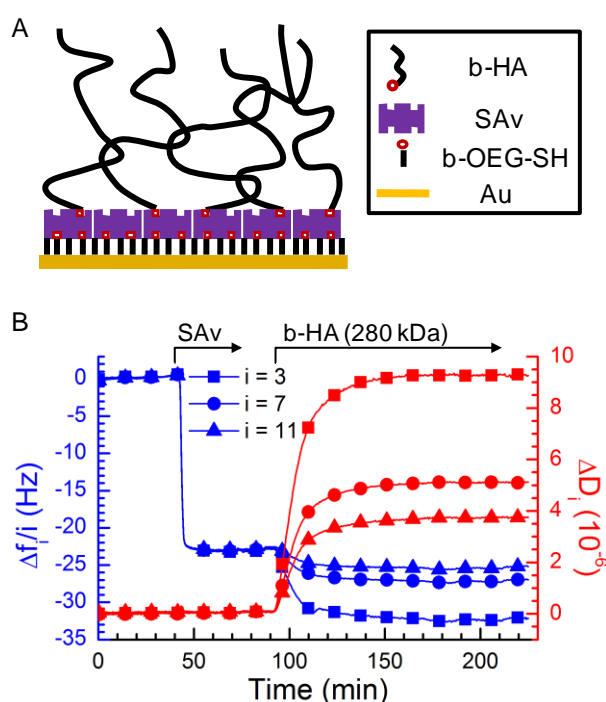
Figure III.1 (A) Schematic of the build up of HA brushes (not to scale). (B) Assembly of an HA brush; a biotinylated OEG monolayer on gold was formed *ex situ* and all subsequent assembly steps were followed by QCM-D. Normalized frequency shifts ($\Delta f_i/i$) and dissipation shifts (ΔD_i) at overtones i = 3, 7, 11 are presented. The start and duration of incubation of each sample (20 µg/mL SAv and 5 µg/mL b-HA) are indicated

by arrows on top; during remaining times, the surface was exposed to sample preparation buffer (10 mM HEPES, 150 mM NaCl, pH 7.4).

III.3.2 HA film thickness, response to NaCl, and grafting density

Colloidal probe reflection interference contrast microscopy (RICM) was used to quantify the thickness of the HA film. The method measures the distance between a colloidal sphere and a planar transparent substrate (169), with a resolution of a few nanometers by the analysis of interference patterns arising from partial reflection of light at the interfaces between the planar SAv-covered substrate and the solution, and between the solution and the colloidal probe. Analogous to previous work by us and others (144, 227), we used triple wavelength RICM to unambiguously resolve the thickness over a range of 1 μm, but we here refined the analysis method to account for the presence of the semi-transparent gold coating and the OEG and SAv layers (see Supplementary Methods and Figure III.S1).

The mean thickness of the HA film in sample preparation buffer (i.e. with physiological ionic strength and pH) was 207 nm. The standard deviation across 10 colloidal probes randomly positioned on the same surface was typically $\pm$ 10 nm, and the standard deviation of the mean values of 5 measurements on independently prepared HA films was $\pm$ 5 nm. This demonstrates that the HA brushes are laterally homogeneous and that their preparation is reproducible. With a contour length of 1.0 nm per disaccharide (13) and a molecular mass of 401 Da (including the Na^+ counterion) per disaccharide, the contour length of 280 $\pm$ 14 kDa HA is $l_c = 698 \pm 35$ nm, and at physiological ionic strength, an unperturbed HA chain of this length is expected to form a random coil with a radius of gyration of $R_g \approx 40$ nm (228). The HA chains are thus significantly stretched compared to their dimensions in solution, confirming that a polyelectrolyte brush is effectively formed.

To further validate the integrity of the HA brush, we quantified the brush thickness as a function of NaCl concentration. We have previously reported a detailed analysis of such a dependence for brushes of HA with a distinct molecular weight (1083 kDa) (20), which serves as a benchmark for the present work. The distance H between polystyrene spheres floating on the HA brush and the SAv-coated substrate was again used as an approximate measure of the brush thickness, and the results are shown in Figure III.2*A* (*red line with solid circles*). Consistent with our previous findings (20), H decreased monotonically with increasing NaCl concentration. The shape of the curve was

qualitatively consistent with theoretical predictions for brushes of strongly charged polyelectrolytes (177-179). Specifically, at low ionic strength ([NaCl] ≤ 0.5 mM) the measured thickness varied only weakly, and this regime corresponds to the "osmotic brush" regime (179) where the brush thickness is determined by the balance of the osmotic pressure of counterions trapped in the brush and the entropy of chain stretching (177). At higher ionic strengths (1 mM ≤ [NaCl] ≤ 1000 mM), salt screens the electrostatic interactions ("salted brush" regime) (179) and leads to a progressive decrease in brush thickness. At very high ionic strength, it is expected that the screening becomes so strong that the excluded volume repulsion of the uncharged polymer backbone (intrinsic excluded volume) dominates the brush behaviour and the dependence on ionic strength again weakens. This "quasi-neutral" brush regime is barely reached in the experiment presented here. We note that the slope for the salted brush regime in the log-log plot is -0.22, which deviates from the power of -1/3 expected by simple theory (177-179). We had previously demonstrated that the apparent attenuation of the salt dependence compared to the theoretical prediction is expected and due to two distinct effects (20): towards low ionic strength, HA brushes become strongly stretched (with H/l_c larger than 0.5) and the resistance to stretching thus becomes stronger than what is predicted according to the Gaussian chain approximation used in the theory; towards high ionic strength, on the other hand, the intrinsic excluded volume of the uncharged polymer backbone, which is positive for HA but not considered in the scaling theory, increasingly contributes to inter-chain repulsion and thus limits the screening effect of the salt.

In our previous work, we also showed that the combined effect of intrinsic excluded volume and electrostatic repulsion on HA brush morphology can be quantitatively reproduced in the limit of high ionic strength (NaCl ≥ 50 mM) with an analytical self-consistent mean-field theory (20). With this approach, we can estimate the grafting density of the HA brush studied here (Supporting Figure III.S2), and the root-mean-square (rms) distance between anchor points is $s \approx 47$ nm. From the HA molecular weight, the brush thickness and the grafting density, one can estimate the concentration of chargeable groups in the HA brush to match the concentration of added salt at around 0.8 mM NaCl. This value is consistent with the transition between the osmotic and salted brush regimes identified above.

Detailed inspection of the bead-substrate distances H in Figure III.2*A* reveals that these exceed the contour length of the HA chain without added salt or at very low NaCl

concentrations. Specifically, in ultrapure water, H exceeded l_c by approximately 260 nm. This result was unexpected and was not observed in the earlier study with HA brushes made from approximately 4 times larger HA chains (20). On the other hand, we found the bead-substrate distance on HA brushes made from smaller HA chains (58 ± 3 kDa) to be 579 ± 8 nm in ultrapure water, that is, the discrepancy with the contour length (145 ± 7 nm) is even larger than in the case of 280 kDa b-HA. Clearly, the polystyrene bead hovers at a certain distance above the HA brush and we propose that this is due to repulsive electrostatic interactions between the negatively charged polystyrene bead and an excess negative charge displayed by the HA brush. The grafting density of the HA brush is expected to increase with decreasing HA size in our assays, because the kinetic limitations associated with brush formation becomes less severe for shorter chains (229). The stretching of the HA chains and also the excess charge of the brush would increase with grafting density, and the thickness trends as a function of HA molecular weight would thus be consistent with such a scenario.

Our finding thus indicates that H can significantly overestimate the brush thickness in the limit of low ionic strength. A quantitative estimation of the magnitude of the discrepancy appears difficult, because we lack the surface charge density on the colloidal sphere. However, with increasing salt concentration, the charges are screened, and we thus expect that the error is progressively decreasing as salt is added. At the same time, the colloidal probe will exert some pressure on the brush due to gravitation and H may thus effectively underestimate the thickness of the unperturbed brush. However, the forces acting on the brushes are small, less than 4 pN considering that gravitational forces are offset by buoyancy, and we thus estimate this effect to be small (20).

III.3.3 Impact of calcium ions on HA films

III.3.3.i   Morphology

We used colloidal probe RICM to analyze the impact of $CaCl_2$ on HA film thickness (Figure III.2*A*, *black line with squares*). As for NaCl, the HA film thickness decreased monotonically with increasing $CaCl_2$ concentration, with the salt dependence being most pronounced at intermediate ionic strengths (0.1 mM ≤ [NaCl] ≤ 100 mM) and a trend towards plateaus at higher and lower ionic strengths. Over the entire range of $CaCl_2$ concentrations, the film thickness was reproducible to within a few nanometres across the measured surfaces, and the film thickness remained well above the rms

distance between grafting points. This reveals that the HA polymers retain their hydrated and stretched, brush-like conformation even at the highest $CaCl_2$ concentration.

Closer inspection revealed a high degree of similarity in the responses of HA brushes to the two salts. The curves for $CaCl_2$ and NaCl could be virtually overlaid on a single master curve through a simple re-scaling of the $CaCl_2$ concentration by a factor of 10 (Figure III.2*B*). This indicates that the effect of calcium ions on the interaction between HA chains in the brush, and apparently also the repulsion between the HA brush and the colloidal probe in the limit of low ionic strength, is equivalent to the effect of sodium ions at 10-fold higher concentration. Considering that the two anions have different valency, this simple scaling is remarkable and not trivial.
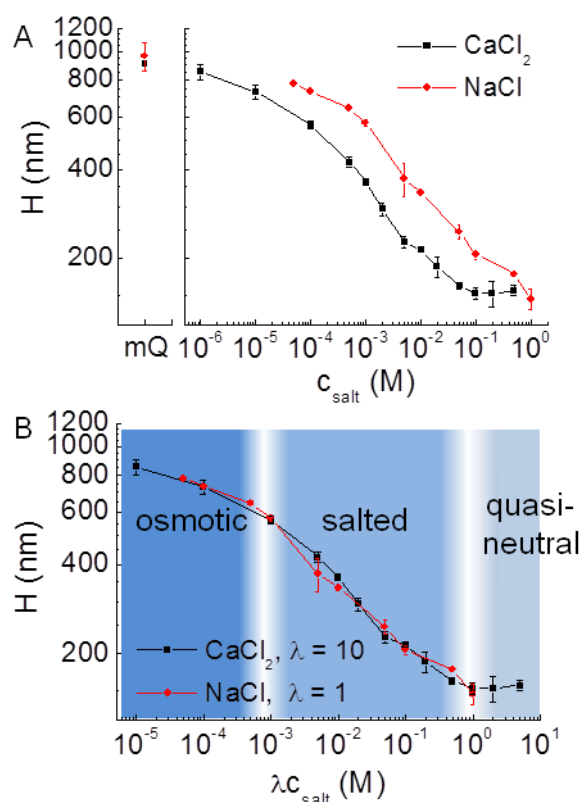
Figure III.2 Effect of sodium and calcium ions on HA brush thickness. (*A*) The distance *H* of colloidal probes (polystyrene beads, around 24 µm diameter, hovering on top of HA brushes due to gravitation) from the SAv-coated substrate was quantified by RICM and is a measure of the HA film thickness. HA brushes were prepared as shown in Figure III.1*B*, and data represent means and standard deviations from two independent experiments. Next to $CaCl_2$ (*black squares*), results for NaCl (*red circles*) are also shown, together with results in ultrapure water without added salt (mQ). (*B*) Both data sets superpose when the salt concentration is re-scaled, by multiplication with

$\lambda = 1$ for NaCl and $\lambda = 10$ for CaCl$_2$. The three canonical brush regimes – osmotic, salted and quasi-neutral – can be identified and are indicated with the coloured background.

III.3.3.ii   Visco-elastic properties

The effect of Ca^{2+} on the visco-elastic properties of HA brushes was characterized by QCM-D. To this end, frequency and dissipation shifts upon variation of the ambient CaCl$_2$ concentration were monitored on HA brushes (Supporting Figure III.S3*A*) as well as reference surfaces (bare SAv without HA; Supporting Figure III.S3*B*). By subtracting the responses on the reference surfaces from those on the HA brushes, the effect of the HA brush could be discriminated from the effects of the ions on the density and viscosity of the solution phase, to which the QCM-D is also sensitive. These data are shown in Figure III.3*A-B*. In addition, we also examined over the full range of CaCl$_2$ concentrations if non-biotinylated HA polymers (237 $\pm$ 12 kDa, at 10 μg/mL) bind to the reference surface (Supporting Figure III.S3*C*), and these effects are shown as insets in Figure III.3*A-B*. Figure III.3*C* shows the ratio of dissipation and frequency shifts $\Delta D_i/(-\Delta f_i/i)$. This parameter is related to the mechanical properties of the surface-confined films. For very thin films, this parameter is proportional to the elastic compliance, a measure of film softness (161). The HA films studied here are too thick for this proportionality to hold, and the parameter should thus be considered an effective and relative measure of HA brush softness. Overall, the film softness decreased with increasing calcium concentration, a trend that is expected as the salt-induced contraction of the HA brush (Figure III.2) makes the film denser. The dependence is monotonous except for a shallow local minimum around 2 mM CaCl$_2$. At this salt concentration, we also found HA to show minor yet significant non-specific interaction with the SAv substrate which was not present at lower and higher ionic strengths (Figure III.3*A*, *inset*). The local minimum in the softness parameter, therefore, most likely is the consequence of a slight perturbation of the HA brush morphology by binding of a fraction of the HA chains to the SAv substrate in addition to the biotin anchorage. It is also notable that the softness parameter (Figure III.3*C*) does not show the pronounced sigmoidal dependence on the calcium concentration that we had observed for the HA brush thickness (Figure III.2). In particular, the rapid decrease in softness in the low ionic strength regime (osmotic brush) suggests that the mechanical properties of the HA

brush are sensitive to ionic strength in the osmotic brush regime even though the thickness remains roughly unchanged.

We also note that the effect of calcium on the HA brushes was fully reversibly for most of the calcium concentrations investigated, that is, QCM-D responses in ultrapure water before and after exposure to each calcium concentration were comparable (Supporting Figure III.S3*A*). Exceptions in this regard were the highest calcium concentrations (≥ 100 mM), for which a fraction of the frequency and dissipation shifts was not recovered upon rinsing in ultrapure water, as shown in detail in Supporting Figure III.S4. Apparently, very high calcium concentrations can promote irreversible (though minor) changes to the HA brush.
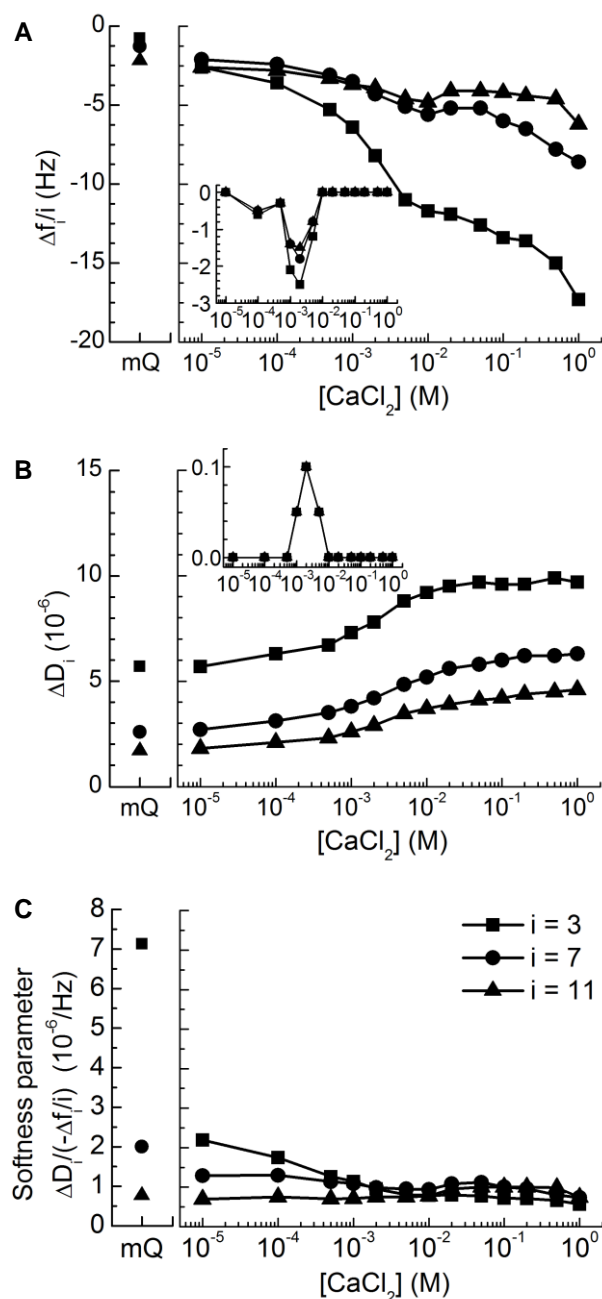
Figure III.3 Effect of calcium ions on HA brush rigidity, characterized by QCM-D. Normalized frequency shifts ($\Delta f_i/i$; A), dissipation shifts (ΔD_i; B) and softness parameter ($\Delta D_i/(-\Delta f_i/i)$; C) are displayed for selected overtones ($i = 3$, 7 and 11, as indicated in C). HA brushes were prepared as in Figure III.1*B*, and data represent responses at equilibrium of the HA film compared to a reference SAv monolayer film as a function of the $CaCl_2$ concentration in ultrapure water (see Supporting Figure III.S3 for details; data in ultrapure water without added salt are also shown, as mQ). Responses upon exposure of non-biotinylated HA (10 μg/mL) to the SAv monolayer are shown for comparison in the *insets* in *A* and *B*; these show minor non-specific binding at

intermediate $CaCl_2$ concentrations and correlate with transient minima in the frequency shifts for the HA brush. The softness parameter indicates HA brush stiffening with $CaCl_2$ concentration.

III.3.4 Impact of pH on HA films

III.3.4.i   Morphology

The effect of pH on the thickness of HA brushes was again characterized by RICM (Figure III.4*A*). We used potassium phosphate as buffering agent throughout, to avoid any effects due to variations in cation species or concentration. Phosphate buffer has pK_a values of 2.1, 7.2 and 12.3 (230), and we found the buffering capacity at a concentration of 100 mM K^+ to be satisfactory over the tested pH range (1.0 to 9.0).

Over a broad range around neutral pH ($6.0 \leq pH \leq 9.0$), *H* remained virtually constant at 216 ± 7 nm. This value matches the results for 100 mM NaCl (206 ± 7 nm; Figure III.2), indicating that potassium and sodium have very similar effects on the HA brush. The mean *H* decreased by roughly two-fold between pH 6.0 to pH 3.0, and then remained roughly constant down to pH 1.0. The carboxyl groups in HA have a pK_a around 3 (14), and the reduction in film thickness is thus likely due to the protonation of carboxyl groups and loss of the polyelectrolyte character of the HA chains.

It is notable that the standard deviations in *H* increased markedly at pH values ≤ 5 (Figure III.4*A*). This indicates that the HA film loses its homogeneity under strongly acidic conditions, and instead forms a film that is heterogeneous on a scale comparable to or larger than the size of the colloidal probe. Circumstantial evidence for the presence of microscale heterogeneities also comes from interferographs taken on HA films in the absence of a colloidal probe. These revealed a distinctive pattern at pH 1.5 that was not (or only faintly) visible at pH values larger than 3 (Figure III.4*B*). The contrast and spatial resolution of the interferographs are too low to assign a specific structure. However, the fact that we observe heterogeneities indicates that protonated HA becomes sticky, and we tentatively propose that the patterns arise from the clustering of sticky HA polymers into microdomains as schematically indicated in Figure III.4*C*. The formation of microphases is indeed predicted by theory (231, 232) and was experimentally observed for other polymer brushes (180).
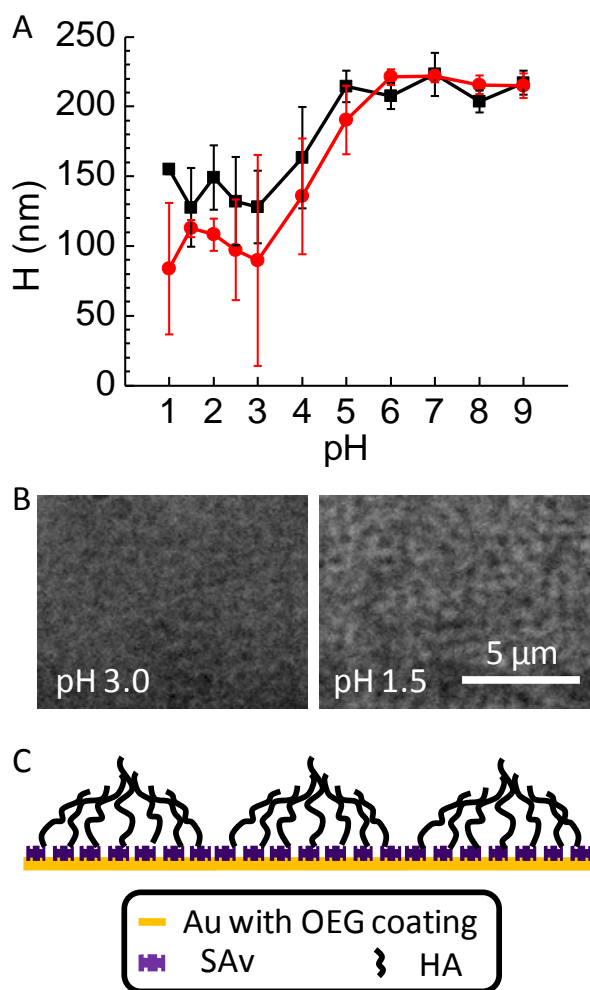
Figure III.4 (*A*) Effect of pH on HA film thickness, quantified by RICM analogous to Figure III.2. Two independent experiments are shown, with means and standard deviations from measurements at 10 different positions per sample. (*B*) Representative interferographs (w/o colloidal probe) of patterns on a substrate with HA film in the presence of pH 3 (*left*) and pH 1.5 (*right*). The contrast of both images was adjusted consistently, and interferographs acquired at pH > 3 were comparable to what is shown here for pH 3. Interferographs at pH 1.5 reveal a distinctive pattern, that is not (or only faintly) visible at pH ≥ 3. (*C*) Schematic of the hypothesised microphase formation in end-grafted HA films at low pH (not to scale).

III.3.4.ii   Visco-elastic properties

QCM-D was again used to study the influence of pH on HA film softness (Figures III.S5 and 5) following the method used for the characterization of the effect of $CaCl_2$ solutions (Figures III.S3 and 3). The softness parameter (Figure III.5*C*) was not sensitive to pH between pH 6.0 and 9.0, but decreased substantially at lower pH values.

The most rigid films (i.e. with the smallest softness parameter) occurred at pH 2.5. At the lowest pH values (≤ 2.0) the HA films became again somewhat softer but clearly remained more rigid than at neutral pH. The effect of pH changes on HA brushes was fully reversible over the large range of pH variations studied, indicating that pH can be used for the reversible switching of HA brush properties. Notably, we did not find any indications for the degradation of HA upon exposure to pH down to 1.0, in contrast to some earlier reports studying HA in the solution phase (225, 226, 233).

It is notable that HA polymers also showed rather strong non-specific binding to the SAv-coated substrate for pH values ranging between 2.5 and 4.0, whereas no such binding was detectable at lower and higher pH values (Figure III.5*A-B*, *insets*). The electrostatic potential of SAv is positive below pH 6 (234), and attractive electrostatic interactions between the (partially) de-protonated HA and the acidic SAv may well be responsible for the selective non-specific binding of HA between pH 2.5 and 4.0. Moreover, it is likely that the transient minimum in the softness parameter at pH 2.5 arises from a combination of reduced inter-HA-chain repulsion (due to HA protonation) and HA-substrate attraction, whereas the values measured at pH 1.0 and 1.5 may well represent the genuine softness of the fully protonated HA brush (in the absence of attractive HA-substrate interactions).
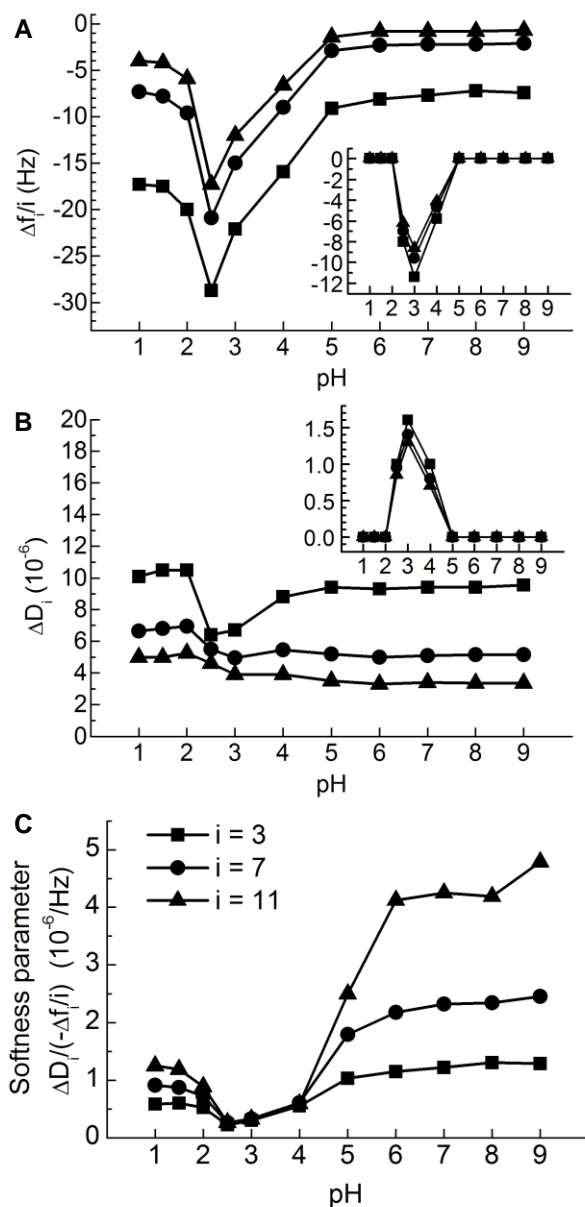
Figure III.5 Effect of pH on HA brush rigidity, characterized by QCM-D. Data are displayed analogous to Figure III.3, in potassium phosphate buffer (containing 100 mM potassium) at various pH. The *insets* in *A* and *B* show strong non-specific binding of non-biotinylated HA at pH 4.0, 3.0 and 2.5. The softness parameter indicates that HA brush stiffening is most pronounced at these pH values.

III.4 DISCUSSION

On the qualitative level, the results of our systematic analysis of the response of HA brushes to calcium ions and pH are largely in line with the known properties of HA in the solution phase. In particular, the response of HA brushes to sodium and calcium ions (Figure III.2) confirms that HA around neutral pH behaves as a strongly charged

and semi-flexible polyelectrolyte in good solvent (we here refer to strongly charged as all chargeable groups being charged irrespective of the ionic strength of the medium, and to semi-flexible as the statistical polymer segment length being much larger than the size of the chemical monomer). Moreover, a 'putty' gel state has been reported for HA solutions around pH 2.5 (225, 235, 236), and the collapse of HA brushes at low pH (Figure III.4*A*), accompanied by microphase formation (Figure III.4*B-C*) and film rigidification (Figure III.5), would be consistent with a transition from repulsive to attractive inter- and intra-chain interactions upon HA protonation.

On the quantitative level, a striking observation that to the best of our knowledge has not previously been reported is that divalent calcium ions affect the HA brush thickness in much the same way as monovalent sodium ions do at tenfold higher concentrations. Can we explain such a similar behaviour? It is well known that divalent ions are more effective than monovalent ions in screening electrostatic interactions, and thus not surprising that calcium ions have the same effect at a lower concentration than sodium ions. However, it remains unclear why the factor of potentiation is around 10, and the divalent ions may well affect the measured brush thickness (Figure III.2*B*) by distinct mechanisms in the different brush regimes. First, divalent counterions can decrease the surface potential more dramatically compared to monovalent ions (237), or may even decrease the surface charge more effectively by counterion condensation. This would result in a decrease in the electrostatic repulsion between the HA brush and the surface of the polystyrene bead, which we have seen to be important at low ionic strength. Second, for a polyelectrolyte brush in the osmotic regime, the brush morphology has been predicted to be sensitive to the valency of added ions (238): ions with multiple charges can substitute several monovalent ions, thus reducing the number of mobile counterions that is necessary to compensate the polymer charge within the brush and thereby diminishing the osmotic pressure of the counterion gas. Specifically, with calcium and sodium having valencies of $z_{Ca} = 2$ and $z_{Na} = 1$, respectively, the brush thickness would be expected to decrease by a factor of $\sqrt{z_{Ca}/z_{Na}} \approx 1.4$ for divalent counterions compared to monovalent counterions at the same molar ion concentration (239). Our experimental data at 0.1 mM and 0.5 mM added salt showed a decrease in H by 1.3 and 1.5, respectively, which is in reasonably good agreement with the theoretical prediction. Third, the thickness of a polyelectrolyte brush is expected to scale with the Debye screening length κ^{-1} as $H \sim \kappa^{-2/3}$ in the salted regime if the thickness changes

were solely driven by electrostatic screening by free ions in the solution phase (239). The Debye length scales as $\kappa^{-1} \sim 0.304\sqrt{[\text{NaCl}]}$ and as $\kappa^{-1} \sim 0.176\sqrt{[\text{CaCl}_2]}$,(237) and consequently, a reduction in thickness by a factor of $(0.304/0.176)^{2/3} \approx 1.4$ would be expected when replacing NaCl by CaCl$_2$ at a given salt concentration. Inspection of Figure III.2*A* reveals that the factor is significantly larger in our experiments (1.6 ± 0.1 between 1 and 50 mM salt). Equivalently, the scaling predicts that CaCl$_2$ has the same screening effect as NaCl at a concentration that is increased by a factor of $(0.304/0.176)^2 \approx 3.0$. This is clearly smaller than the factor of 10 obtained in our experiments, indicating that additional effects must also play a role. Possible mechanisms are a reduced polymer charge due to condensation of calcium ions on the HA chains, and potentially also the bridging of carboxylic groups on HA owing to the bivalency of the calcium ions (240). Taken together, the mechanisms underlying the tenfold potentiation of calcium over sodium ions with regard to brush thickness variations remains to be further elucidated. Future comparative studies with different divalent ions, and possibly also monovalent and trivalent ions, may help resolving this question.

On one hand, the results of the present study are relevant for rationalizing the basic physical properties of HA-rich matrices in biological systems. We learn that protonation of carboxyl groups affects HA brush morphology and mechanical properties only at pH values below 6.0 and is thus unlikely to be relevant under physiological conditions. The presence of a few mM calcium ions in the extracellular space, on the other hand, should impact the properties of HA-rich matrices appreciably already via simple physical effects related to the screening of charges. Naturally, the situation in native HA-rich matrices will be more complex, for example, because HA-binding and other proteins also contribute to defining matrix assembly and dynamic reorganization, and their function may also be modulated by calcium ions. However, the simplified yet well-defined model system studied here provides an idea of the magnitude of effects that can occur and provides a reference for studies with more complex systems.

On the other hand, our results provide information that should be useful for the rational design of HA-based materials with tailored properties. Here, HA brushes appear particularly attractive for the development of stimuli-responsive surface coatings: it combines a large dynamic range – such as a fivefold thickness change in response to ions (Figure III.2) and a twofold thickness change in response to pH (Figure III.4) –

with a high degree of reversibility in the morphological changes, thus allowing for strong and repeatable switching by external stimuli. Changes in thickness can be exploited directly as a readout, or as a mechanical actuator, for sensing applications. Associated changes in brush concentration and hence physical properties such as viscoelasticity (Figures III.3 and 5) or permeability could also be exploited for applications. An important parameter defining permeability is the correlation length ξ, a statistical measure of the distance between segments on neighbouring chains (175). In homogeneous meshworks of flexible polymers, the correlation length is an effective measure for the mesh size, and in good solvent it is predicted to decrease with polymer concentration c with a power of -3/4 (174). For a given HA brush (i.e. at constant grafting density), we have thus $\xi \sim c^{-3/4} \sim H^{-3/4}$ to a first approximation, and a fivefold reduction in brush thickness would thus entail a more than threefold reduction in the size of particles that can effectively permeate the HA film.

III.5 CONCLUSIONS

In this work, we have systematically analyzed the variations in thickness (by colloidal probe RICM) and softness (by QCM-D) of HA brushes over a broad range of Ca^{2+} concentrations and pH. Within the physiologically relevant ranges of these two parameters, we found the softness and thickness of HA brushes to be exquisitely sensitive to Ca^{2+} concentrations but essentially insensitive to pH. More broadly, we discovered that the effect of divalent calcium ions on HA brush thickness is virtually identical to the effect of monovalent sodium ions at 10-fold higher concentrations, and that HA brushes collapse upon protonation below pH 6.0. Our findings are relevant for understanding the supramolecular organization and dynamics of HA-rich matrices in biological systems and potentially will also benefit the rational design of synthetic HA-rich materials with tailored properties.

III.6 SUPPORTING MATERIAL

III.6.1 Refinement of the colloidal probe RICM analysis for coated glass substrates

In previous work (130), we found an algorithm that is based on the quantification of the radial position of intensity extrema in colloidal probe interferographs (130, 169) to work well for quantifying the thickness of HA brushes formed on bare glass. In the present work, HA brushes were formed on glass that was coated with a thin metal film.

In the following, we show that the established method can also be applied on metal-coated glass with a simple modification.

We follow textbook knowledge (241) to describe the interference of light following transmission and reflection at multiple interfaces (Figure III.S1A). For two parallel interfaces – formed by medium 0, an interlayer of medium 1, and medium 2 – the total reflectance R, which determines the reflected intensity $I_{reflection}$ for a given intensity $I_{incidence}$ of the incident light, is given by

$$R = I_{reflection} / I_{incidence} = |r_{012}|^2, \tag{Eq. 1}$$

where r_{012} presents the total effective reflection coefficient. This coefficient takes all light beams reflected back into medium 0 into account (Figure III.S1A) and is given by

$$r_{012} = r_{01} + t_{01}t_{10}r_{12}e^{-i2\beta} + t_{01}t_{10}r_{10}r_{12}e^{-i4\beta} + t_{01}t_{10}r_{10}^2 r_{12} e^{-i6\beta} + \cdots, \tag{Eq. 2}$$
$$= r_{01} + [r_{01} + r_{12}\exp(-i2\beta)] / [1 + r_{01}r_{12}\exp(-i2\beta)]$$

where r_{xy} and t_{xy} are the local reflection and transmission coefficients at the interface between media x and y. The phase variation between two contiguous outcoming beams is constant. Assuming to a first approximation that light is incident perpendicular to the substrate, it is expressed as

$$\beta = 2\pi\tilde{n}_1 d / \lambda, \tag{Eq. 3}$$

where $\tilde{n}_1$ and d are the complex refractive index and the thickness of the interlayer, and λ is the wavelength of the incident light. Both reflection and transmission coefficients are then easily determined as

$$r_{xy} = (\tilde{n}_x - \tilde{n}_y)/(\tilde{n}_x + \tilde{n}_y) \text{ and } t_{xy} = 1 - r_{xy}. \tag{Eq. 4}$$

The complex refractive index, expressed as

$$\tilde{n} = n - i \cdot 2\pi k / \lambda, \tag{Eq. 5}$$

considers the refractive index n and the extinction coefficient k, and thus is appropriate for fully transparent layers (such as glass or the solution) as well as light-absorbing layers (such as Au).

The case of two interlayers can be reduced to the case of one interlayer (Figure III.S1B), that is, the effective reflection coefficient r_{123} of a system consisting of media 1, 2 and 3 can first be determined by the approach described above, and then integrated with medium 0 by treating the two interlayers (made of media 1 and 2) as a single layer with effective optical properties. The total effective reflection coefficient is then

$$r_{0123} = r_{01} + [r_{01} + r_{123} \exp(-i2\beta)]/[1 + r_{01}r_{123} \exp(-i2\beta)].$$

(Eq. 6)

This method can be further expanded for more interlayers.

To reproduce our experimental setup, we simulated the reflectance of a system consisting of a glass substrate, followed by a metal film (0.5 nm Ti adhesion layer + 5 nm Au), a hydrated organic film (8 nm, representing the OEG and SAv monolayers), a buffer layer of variable thickness (representing the space between the planar coated substrate and a given position on the surface of the colloidal probe; due to its strong hydration, the refractive index of the HA film can be considered equivalent to that of buffer to a good approximation) and a polystyrene medium (representing the colloidal probe). The optical properties used for the different media are provided in Table III.S1 and the results are shown in Figure III.S1C.

The data in Figure III.S1C illustrate the periodic dependence of the reflectivity on the probe-substrate distance. Importantly, the sinusoidal shape of the curve is not appreciably distorted by the metal film, alone (*red curve*) or in conjunction with the organic film (*blue curve*), as compared to the bare glass (*black curve*), and the length of the period (λ / 2 n_{buffer}) also remains unchanged. The position of the extrema, on the other hand, is sensibly affected.

Table III.S1 Refractive indices and extinction coefficients used in the simulation of reflectance.

	Glass	Ti	Au	Organic film	Buffer	Polystyrene
n	1.514	1.771	1.017	1.450	1.333	1.550
k	0	2.374	1.826	0	0	0

These theoretical predictions justify our approach to analyze the experimental RICM data. Specifically, we used the analysis approach previously established for bare glass (130) to determine (i) the effective probe-surface distance H_{ref} on a reference surface featuring the metal film, the OEG monolayer and the SAv monolayer, and (ii) the effective probe-surface distance H_{HA} on an identically prepared surface with grafted HA. The real probe-substrate distance was then obtained as $H = H_{HA} - H_{ref}$. The offset by H_{ref} fully accounts for the effect of the metal and organic films on the position of the extrema with respect to the probe-surface separation.

We note in passing that Figure III.S1C also shows that the maximal reflectance is enhanced with the metal film. This was indeed observed in the experiment and is an advantage as it enhances image contrast.

III.6.2 Supporting figures
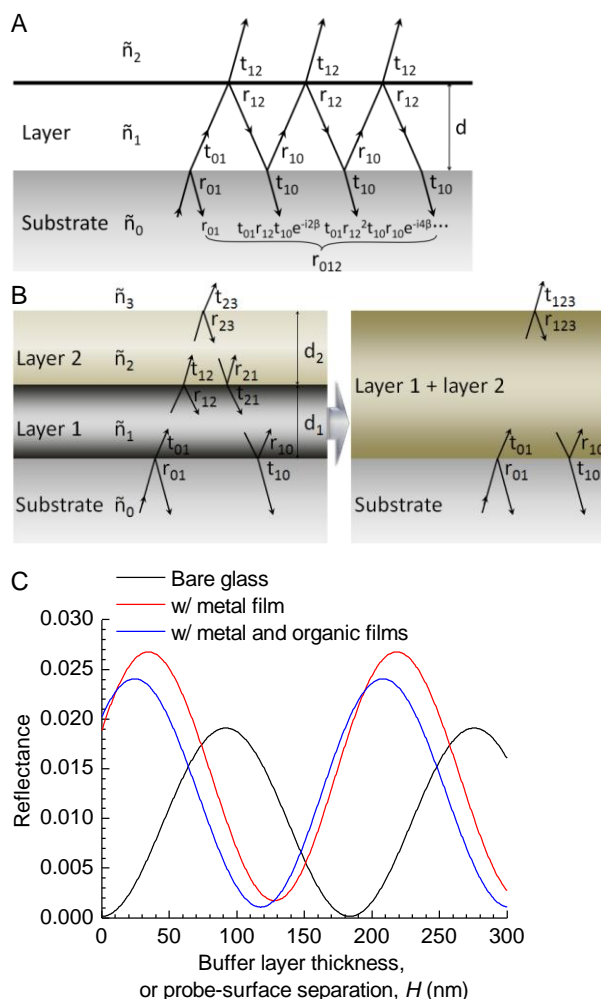
Figure III.S1 Impact of coatings on the glass substrate on RICM data analysis. (*A*) Schematic of the multiple reflections occurring at a single layer (medium 1) sandwiched between two other media (0 and 2). (*B*) Schematic of the light paths in a system with two layers and simplification to a single effective layer. (*C*) Simulated reflectance for a multilayer system consisting of a glass substrate, a buffer interlayer and polystyrene as a funcation of the buffer interlayer thickness H (for details see the text above and Table III.S1; λ= 490 nm). The glass was either bare (*black curve*), coated with a metal film (*red curve*), or coated with a metal film and an organic film (*blue curve*). In the experiment, the data would correspond to the reflectance at the centre of the colloidal probe as a function of the probe-surface separation H.
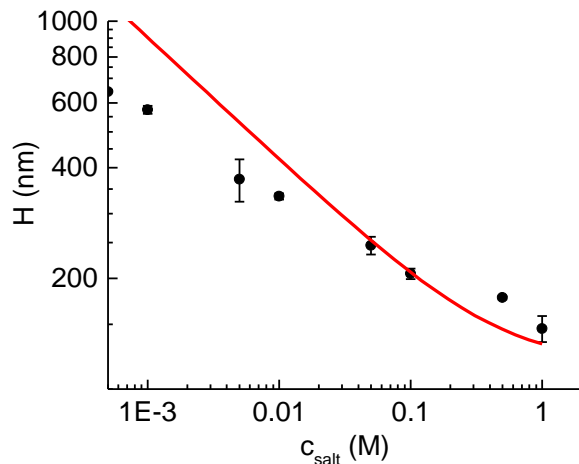
Figure III.S2 Estimation of grafting density. Unperturbed HA brush thickness measured at different NaCl concentration (*symbols*, extracted from Figure III.2) together with a fit (*line*, to data $\geq$ 50 mM NaCl) with a previously developed mean field theory (20). From the fit, a root-mean-square distance $s = 47$ nm between anchor points is estimated.

The mean field approach of treats HA as a semi-flexible polymer and the electrostatic repulsion between polyelectrolyte chains in the brush as an effective excluded volume, and has previously been found to describe HA brushes in NaCl solutions of sufficiently high ionic strength ($\geq$ 50 mM) well (20). Specifically, the thickness is predicted to depend on ionic strength as $H = (8/\pi^2)^{1/3} (pv/bs^2)^{1/3} l_c$, where l_c is the polymer contour length, b the monomer unit length, p characterizes the intrinsic chain stiffness, and v is the effective excluded volume. At high ionic strength, $v = v_0 + \alpha^2 / (4c_{NaCl})$, where α is the fraction charge per monomer unit and $v_0 = Ab^3$ the 'bare' excluded volume in the absence of charge repulsion (A is a numerical pre-factor, and depends on the monomer shape and the solvent quality). For the fitting, we used $p = 14$, $b = 1$ nm, $A = 0.9$ and $\alpha = 1$ (established in ref. (20)), $l_c = 698$ nm (equivalent to 280 kDa HA), and s was the only adjustable parameter.
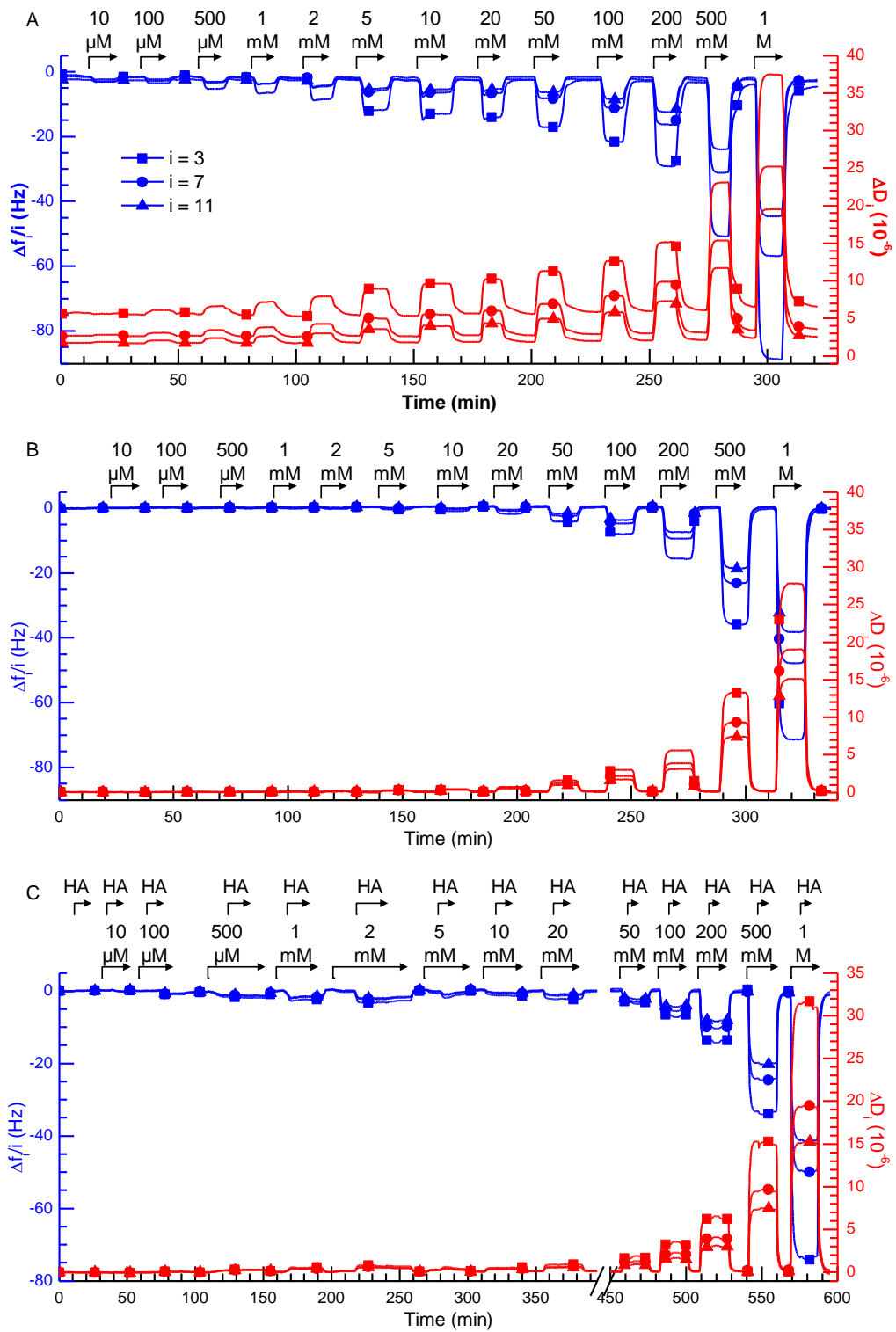
Figure III.S3 Effect of calcium ions on HA brushes, characterized by QCM-D. Representative time-resolved data for an HA brush (prepared as in Figure III.1*B*; *A*), a reference surface (SAv monolayer without HA; *B*), and non-specific binding of non-biotinylated HA to the reference surface (*C*). Shifts in normalized frequency, $\Delta f_i/i$, and in dissipation, ΔD_i, relative to a SAv monolayer in ultrapure water are displayed for overtones $i = 3$, 7 and 11 (as indicated in *A*). The start and duration of incubation of $CaCl_2$ (at various concentrations, as displayed) or HA (at 10 µg/mL) are indicated by arrows on top; during remaining times, surfaces were exposed to ultrapure water. The QCM-D responses upon incubation of $CaCl_2$ solution in *B* do not reflect any changes on the surface but result from changes in viscosity and/or density of the solution owing to the added $CaCl_2$. The frequency and dissipation shifts displayed in Figure III.3*A-B* were obtained by subtracting data in *B* from *A*, and essentially reflect the HA film alone.
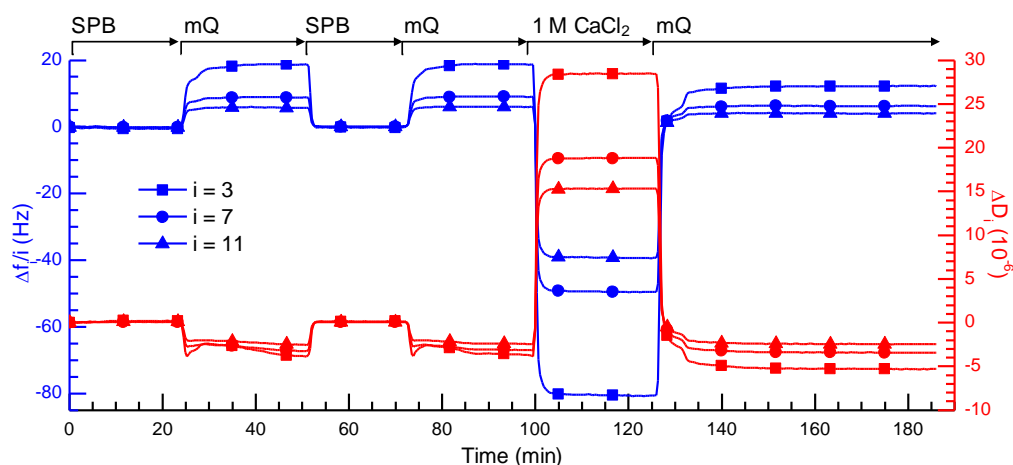
Figure III.S4 Reversibility of calcium effect on HA brushes. An HA brush was prepared as in Figure III.1*B*, and time-resolved QCM-D data at overtones $i = 3$, 7 and 11 for the response to various solutions (indicated by arrows on top) are shown. The transition from sample preparation buffer (SPB) to ultrapure water (mQ) is fully reversible, but 1 M $CaCl_2$ in ultrapure water has a minor irreversible effect on the HA brush.
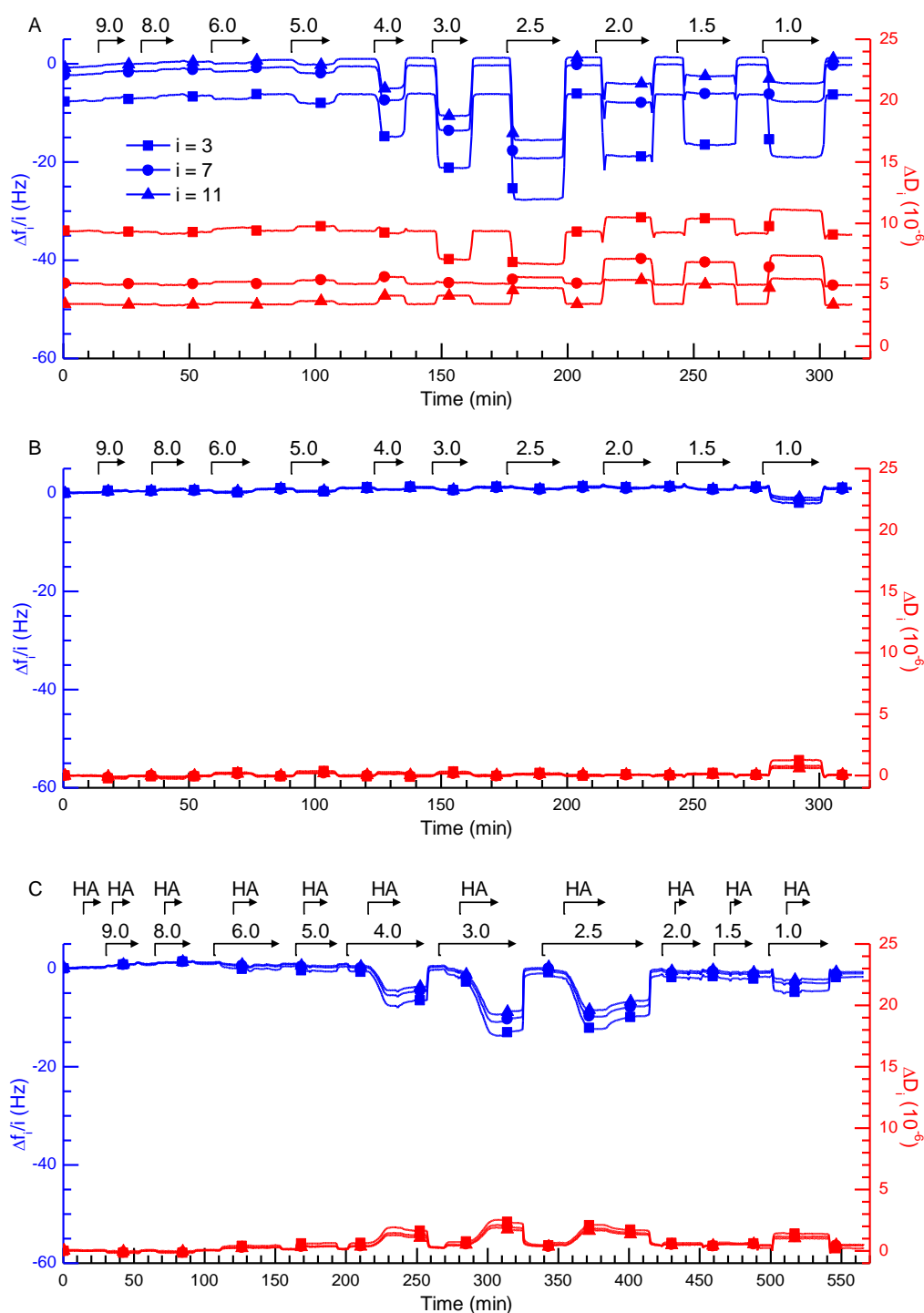
Figure III.S5 Effect of pH on HA brushes, characterized by QCM-D. Representative time-resolved data for an HA brush (prepared as in Figure III.1*B*; *A*), a reference surface (SAv monolayer without HA; *B*), and non-specific binding of non-biotinylated HA to the reference surface (*C*). Overtones $i = 3$, 7 and 11 are shown, as indicated in *A*. The start and duration of incubation of potassium phosphate buffer (containing 200 mM potassium at various pH, as displayed) or HA (at 10 µg/mL) are indicated by arrows on top; during remaining times, surfaces were exposed to potassium phosphate buffer at pH

7.0. The QCM-D responses upon incubation of solutions with different pH in *B* do not reflect any changes on the surface but result from changes in viscosity and/or density of the solution owing to the presence of added salt. The frequency and dissipation shifts displayed in Figure III.5*A-B* were obtained by subtracting data in *B* from *A*, and essentially reflect the HA film alone.

IV Theoretically predicted morphology of cross-linked polymer brushes

The research work presented in this chapter is in preparation as a manuscript, for submission to a peer reviewed journal, as:

Morphology and function of the nuclear pore permeability barrier – a case study of cross-linked polymer brushes

Xinyue Chen,[1,2,*] Raphael Zahn,[1,*] Steffen Frey,[3,7] Dirk Görlich,[3] Oleg V. Borisov,[4,5] and Ralf P. Richter[1,2,6]

[1] CIC biomaGUNE, San Sebastian, Spain; [2] Max-Planck-Institute for Intelligent Systems, Stuttgart, Germany; [3] Department of Cellular Logistics, Max Planck Institute for Biophysical Chemistry, Göttingen, Germany; [4] CNRS, UMR 5254, IPREM Institut des Sciences Analytiques et de Physico-Chimie pour l'Environnement et les Matériaux, Université de Pau & Pays de l'Adour, Pau, France ; [5] Saint-Petersburg State Polytechnic University, St. Petersburg, Russia; [6] University Grenoble Alpes - CNRS, Laboratory of Interdisciplinary Physics (LIPhy), Grenoble, France; [7] Current address: NanoTag Biotechnologies, Göttingen, Germany.
[*] These authors contributed equally.

My contribution: I co-designed research (together with Raphael Zahn, Oleg V. Borisov and Ralf P. Richter). I contributed to developing the theoretical approach (together with Oleg V. Borisov and Ralf P. Richter), and performed all computational work. I analyzed the computational data and correlated theoretical results with experiments (together with Raphael Zahn, Oleg V. Borisov and Ralf P. Richter). I prepared the figures and wrote the first draft of the manuscript except for the parts pertaining to the experimental system and data. I contributed to the revisions of the manuscript.

Abstract: The permeability barrier of nuclear pore complexes (NPCs) controls bulk macromolecular exchange between the cytoplasm and the nucleus of eukaryotic cells. It consists of flexible protein domains ('FG domains') that are grafted to the pore walls and rich in phenylalanine-glycine (FG) motifs. FG motifs act as 'stickers' and promote binding of nuclear transport receptors (NTRs) and inter-FG-domain cross-linking. To understand the functional implications of inter-FG-domain cross-linking and shed light on the physical mechanisms behind NPC permselectivity, we have combined quantitative experiments on planar cross-linked brushes made from regular neo FG domains as a well-defined nanoscale model of the permeability barrier with a self-consistent mean-field theory that predicts brush thickness and density profile as a function of the density and strength of reversible stickers. By correlating theory and experiments, we estimate that the strength of individual inter-FG-motif interactions is relatively weak ($K_d \gtrsim 10\,\text{mM}$), and that a relatively small fraction of FG motifs ($\lesssim 25\%$) is simultaneously engaged in cross-linking at physiological FG motif concentrations. Moreover, we find that not only the FG motifs but also the spacer regions between FG motifs make sizeable contributions to the overall cohesiveness of FG domains. Based on these new insights, we propose a refined model for nuclear pore permselectivity in which the (individual) inter-FG-motif and NTR•FG motif interactions all are of low affinity, enabling dynamic reorganization of the permeability barrier and rapid NTR translocation, whereas the multivalency of the (collective) NTR•FG domain and inter-FG-domain interactions promotes the formation of a cohesive meshwork with a small mesh size (for size selectivity) and the selective entry (and thus translocation) of NTRs.

IV.1 INTRODUCTION

Nuclear pore complexes (NPCs) are large membrane-spanning protein structures that are embedded in the nuclear envelope and regulate bulk macromolecular transport into and out of the nucleus (242-246). Their functional key component is a central 30 to 50 nm wide channel that is filled with NPC protein (nucleoporin) domains that are rich in phenylalanine-glycine (FG; single letter code is used throughout) dipeptide motifs (FG domains). FG domains bind nuclear transport receptors (NTRs) and act as a permeability barrier allowing small molecules (up to approximately 40 kDa or 5 nm in diameter) to translocate freely between cytosol and nucleus while the passage of larger molecules is delayed or blocked unless they are bound to NTRs (246-249).

FG domains are natively unfolded (250-252), and thus lack a defined three-dimensional structure and can be considered as flexible polymers. The FG domains are grafted at a high density to the NPC channel walls (251, 253), and – from a polymer physics point of view – their assembly may hence be qualified a polymer brush (187). However, FG domains are not devoid of intramolecular and intermolecular interactions. They interact attractively with each other, and this cohesiveness promotes the formation and determines the properties of FG domain phases (180, 254-257), and is also essential for the formation of a functional permeability barrier (256, 258). FG motifs contribute to these interactions (180, 256), and with each FG domain carrying many FG motifs, these interactions are intrinsically multivalent. At the same time, FG domains also interact with nuclear transport receptors, and this interaction facilitates their passage through the NPC. This interaction is also multivalent and involves multiple FG motifs on FG domains and FG motif binding sites on the NTR (259-263). Adding to the complexity, there are different types of FG motifs (FG, FxFG and GLFG being the most common ones), and FG domains differ in prevalent FG motif types, FG domain size, abundance of FG motifs relative to FG domain size, as well as in the distribution of FG motifs along the peptide chains and the composition of the spacer regions between FG motifs (264). How the variety in FG domain primary structure, and the associated variety in inter-FG-domain and NTR•FG domain interactions collectively define the function of the permeability barrier remains controversial (265), and there remains uncertainty about the morphology of the permeability barrier (255, 256, 266, 267).

Physical models have been helpful for understanding the mechanisms underlying the assembly and function of the nuclear pore permeability barrier. We and others have

recently shown, for example, that the binding of NTRs into FG domain films, and the ensuing film thickness changes, can be effectively reproduced by models that completely ignore all chemical and structural heterogeneity and instead consider the FG domains as homogeneous, flexible polymers and the NTRs as featureless spheres (268, 269). Homopolymer models also effectively explain how cohesiveness of FG domains enhances the rate of FG domain supramolecular assembly, and how it may determine the size selectivity of FG domain assemblies (180) and the viscoelastic properties of the nuclear pore permeability barrier (270) or FG domain films (167). These findings imply that the exact chemical make-up and structure of FG domains and NTRs may not be critical for controlling the assembly, physical properties and permselectivity of the nuclear pore permeability barrier.

By their nature, however, FG motifs are discrete interaction sites along FG domains (and so are their corresponding binding sites on the NTR surface). To capture this level of complexity, we here consider FG domains as flexible polymers that are endowed with a set of discrete 'stickers' that can interact more strongly with each other than the rest of the otherwise homogeneous polymer chain. With such a model, we can resolve important questions that thus far have proven difficult to address: How do discrete stickers affect the morphology of FG domain assemblies, as compared to attractive interactions between homopolymers? How strong are individual inter-FG-motif interactions? And do all FG motifs in FG domain assemblies simultaneously engage in bonds?

Here, we address these questions by studying planar cross-linked brushes as a well-defined nanoscale model system of the nuclear pore permeability barrier that is tractable in quantitative experiments and in analytical theory. The experimental approach builds on previous work, were we produced films of end-grafted purified FG domains that are similar to the protein meshwork in NPCs, both in their thickness and in their FG motif density (180, 268, 271). However, instead of the native FG domains with their complex amino acid composition we here employ artificial polypeptide chains that are made of a 16-fold repetition of a 19 amino acid sequence containing an FG motif ('sticker'; FSFG, GLFG, GSFG, or SSSG as control) along with 15 other amino acids ('spacer'). The 16 stickers per neo FG domain together have a quantifiable effect on brush rigidity and thickness, and because the polymer is regular we can deduce the properties of individual interactions from the collective response, even if the individual interaction per se is too weak to be measured directly. Specifically, our sequence was inspired by the C-terminal

part (amino acids 298 to 600) of the FG domain of the nucleoporin Nsp1 from *S. cerevisiae* which features almost exclusively FSFG motifs along with spacers of regular length (15 amino acids).

To rationalize how the reversible association of discrete 'stickers' into cross-links affects the morphology of brushes, we combine the self-consistent mean-field theory of polymer brushes (182) with the mean-field theory of thermo-reversible gelation of associative polymers (272). The new analytical theory reveals that the effect of weak stickers on the brush thickness and density profile can be effectively described by the simpler and well known case of a homopolymer brush at reduced solvent quality (182), whereas a distinct behavior that has no classical counterpart emerges for strong stickers, with the brushes adopting a more box-like density profile.

Importantly, the correlation of theory and experiment provides quantitative estimates of fundamental interaction parameters that have so far been difficult to access, that is, (i) the relative effects of FG motifs vs. spacer regions on the cohesiveness of FG domains, (ii) the strength of individual inter-FG-motif interactions, and (iii) the fraction of FG motifs that are on average engaged in bonds. To assess the functional implications of our findings, we compare the strength of individual inter-FG-motif interactions with the strength and kinetics of individual NTR•FG motif interactions (259), and consider the interplay of multivalent inter-FG-domain and NTR•FG domain interactions. We propose a model in which the individual inter-FG-motif and NTR•FG motif interactions define the dynamics (rate of reorganization and NTR translocation), and the collective inter-FG-domain and NTR•FG domain interactions the morphology (compactness and NTR uptake), of the permeability barrier.

IV.2   MATERIALS AND METHODS

IV.2.1   FG domains and buffer

We used three artificially designed regular FG domains which were largely identical in sequence, but had distinct FG motifs. Specifically, they consisted of an N-terminal H_{14} tag (MSKHHHHSGHHHTGHHHHSGSHHHTG), followed by a TEV cleavage site (ENLYFQGSA), 16 repetitions of the sequence STPA**XXXX**ASNNNSTNNGT and a C-terminal cysteine (SC). The letters XXXX define the FG motif and the name of the neo FG domains: FSFG (molecular mass M_W = 34.1 kDa), GLFG (33.1 kDa) and GSFG (32.7 kDa). As a reference, we used a fourth polypeptide with an SSSG sequence

instead of the FG motif (32.2 kDa). All polypeptides were purified as described earlier (180, 271, 273, 274) and stored at a concentration of 10 mg/mL in 50 mM Tris pH 8.0 and 6 M guanidine hydrochloride (GuHCl) at -80 °C. Prior to use, the polypeptides were diluted in working buffer (10 mM Hepes, pH 7.4, 150 mM NaCl) to desired concentrations. The residual concentration of GuHCl in the final solution was kept below 60 mM in all measurements.

IV.2.2 In situ combination of spectroscopic ellipsometry (SE) and quartz crystal microbalance with dissipation monitoring (QCM-D)

The formation of FG domain films was simultaneously followed by SE and QCM-D on the same surface and in a liquid environment (275). To this end, we used a custom-built cuvette-like open fluid cell, placed in a Q-Sense E1 system (Biolin Scientific AB, Västra Frölunda, Sweden; providing QCM-D data) and mounted on a spectroscopic rotating-compensator ellipsometer (M2000V, J. A. Woollam Co., Lincoln, NE; providing SE data), as described in detail elsewhere (276).

In the SE measurements, ellipsometric angles (Δ and ψ) were acquired over a wavelength range of $\lambda = 380$ to 1000 nm at $70°$ angle of incidence and ~ 5 s time resolution. In the QCM-D measurements, frequency and dissipation shifts (Δf_i and ΔD_i) were acquired for six overtones ($i = 3, 5, ..., 13$, corresponding to resonance frequencies $f_i \approx 15, 25, ..., 65$ MHz) with a time resolution of ~ 1 s. For analysis that does not require viscoelastic modelling, each overtone provided similar information, and we therefore present changes in dissipation, ΔD, and normalized frequency, $\Delta f = \Delta f_i/i$, for only one selected overtone ($i = 3$).

Prior to each measurement, the walls of the cuvette were passivated by incubation with a buffer solution containing 10 mg/mL of bovine serum albumin (BSA; Sigma) for 30 min. The cuvette was rinsed with buffer, ultrapure water and blow-dried with nitrogen gas. For the measurement, the cuvette was filled with ~ 2 mL working buffer, continuously stirred and held at a temperature of 23 °C. Samples were injected directly into the buffer-filled cuvette at desired concentrations. To remove samples, the cuvette content was diluted, by repeated addition of excess buffer and removal of excess liquid, until the concentration of soluble sample, estimated from the dilution rate, was below 10 ng/mL.

IV.2.3 Surface functionalization

All measurements were performed on silica-coated QCM-D sensors that are optimized for combined SE/QCM-D experiments (QSX335; Biolin Scientific AB). The sensors were cleaned by immersion in a 2 % sodium dodecyl sulfate solution for 30 min, rinsed with ultrapure water, blow-dried with nitrogen gas, and exposed to UV/ozone (BioForce Nanosciences, Ames, IA) for 30 min. We mounted the cleaned sensors in the combined SE/QCM-D and functionalized their surface with supported lipid bilayers (SLBs) exposing Ni^{2+} ions for the capture of His tagged molecules, as described previously (180, 271). Briefly, we used sonication to prepare small unilamellar lipid vesicles (SUVs) containing dioleoylphosphatidylcholine (DOPC; Avanti Polar Lipids, Alabaster, AL) and 3 mol-% of lipid analogs with headgroups comprising three Ni^{2+}-chelating nitrilotriacetic acid moieties (SOA-tris-NTA) (277). SLBs were spontaneously formed by injecting SUVs (at 50 µg/mL final concentration) with $NiCl_2$ (at 10 µM final concentration) into the buffer-filled SE/QCM-D fluid cell. Binding and spreading of SUVs eventually leading to SLB formation was monitored by SE and QCM-D and only SLBs of good quality (i.e. showing QCM-D frequency shifts, $\Delta f = 29 \pm 1$ Hz, and dissipation shifts, $\Delta D < 0.5 \times 10^{-6}$) were used for further measurements.

IV.2.4 FG domain film formation

We injected the FG domains directly into the SE/QCM-D cuvette equipped with an SLB-coated sensor. During sample injection and for a brief period (10 to 15 s) afterwards, the cuvette content was homogenized with a magnetic stirrer. FG domain film formation was then followed in still solution to ensure homogeneous binding across the sensor surface and thus to guarantee that SE and QCM-D (which have overlapping but not identical sensing areas) monitor the same process (276). During all other incubation and rinsing steps, the solution was stirred to maintain the cuvette content homogeneous.

IV.2.5 Quantification of FG domain grafting density and film thickness

We quantified FG domain surface densities by fitting the SE data to a model of multiple optically homogeneous layers implemented in the software CompleteEASE (J. A. Woollam Co.). The fitting method for the QSX335 sensor substrate is described in

detail in ref. (276). The FG domain film was treated as a transparent Cauchy film with an effective optical thickness d_{SE} and a wavelength-dependent refractive index $n(\lambda)$. FG domain grafting densities Γ where obtained through de Fejter's equation (278), i.e., $\Gamma = \frac{1}{M_W} \frac{d_{SE} \Delta n}{dn/dc}$, where Δn is the difference in refractive index between the FG domain film and the buffer solution (assumed to be wavelength independent) and M_W the FG domain molecular mass. We used $dn/dc = 0.18$ cm^3/g as refractive index increment, which is typical for proteins (275). The resolution in $\Gamma \times M_W$ was ~0.5 ng/cm^2. Among the optical mass-sensitive techniques, SE is particularly suited to quantify the areal mass density of organic films up to a few 10 nm thick, because mass determination is virtually insensitive to the distribution of material within the film (275).

We determined the thickness of FG domain films by fitting the QCM-D data to a continuum viscoelastic model, as described in detail previously (167). Briefly, we used the software QTM (279) (option "small load approximation" (162, 280)). The FG domain films were modeled as homogeneous viscoelastic films with a storage modulus (G') and a loss modulus (G'') that depend on frequency in the form of a power law. The film density was fixed based on the areal mass density (determined by SE) and partial specific volume of proteins, and the density of water. The semi-infinite bulk solution was assumed to be a Newtonian fluid with the density and viscosity of water. The specified errors represent a confidence level of one standard deviation (68 %). In previous studies (167, 180, 271), we found that the thickness results obtained by QCM-D for FG domain films are comparable to within the specified confidence levels to those obtained with another technique, atomic force microscopy, thus confirming that the thickness determination is robust.

Computation. A closed set of equations describing the morphology of cross-linked brushes was solved numerically for selected parameter sets (see below) using a custom-made algorithm implemented in Matlab (Mathworks, Natick, MA).

IV.3 THEORY

IV.3.1 Mean-field theory of cross-linked brushes

We consider a polymer brush formed by linear, flexible homopolymers with associating groups (i.e. stickers) grafted onto a planar, solid substrate and immersed in a solvent at temperature T. Each polymer chain is composed of N segments of length a. The root-mean-square (rms) distance between two adjacent anchor points is s. Each

polymer contains N_{st} stickers, and a pair-wise bond is considered formed when two stickers are found within a volume $2v_b$, where v_b is the 'sticker volume'. The free energy gain for the association of two isolated stickers into a pair is represented by $\varepsilon > 0$.

It is our aim to predict how the morphology of the polymer brush is affected by the association of stickers. To this end, we use the self-consistent mean-field theory developed by Zhulina et al. (182) to describe the polymer brush, and combine it with the mean-field theory of thermo-reversible gelation of associative polymers developed by Semenov and Rubinstein (272).

The Helmholtz free energy per chain in the brush can be presented as

$$E = s^2 \int_0^H [f_{int}(x) + f_{el}(x)] dx, \tag{1}$$

where $f_{int}(x)$ and $f_{el}(x)$ are the free energy of interactions and the contribution of conformational entropy of stretched chains per unit volume of the brush, respectively, x is the distance from the grafting surface, and H is the brush thickness.

The elastic free energy is specified under the strong stretching approximation employed by the theory (182) as

$$\frac{f_{el}(x)}{kT} = \frac{3}{2a^2 s^2} \int_x^H g(x') E(x, x') dx', \tag{2}$$

where k is the Boltzmann constant, $g(x')$ is the normalized distribution of the free ends of the chains, $E(x, x') = dx/dn$ is the local stretching function and $x(n)$ is the most probable position of the n-th segment of the chain (counted from the grafting point) provided that the chain end is located at x'.

The interaction free energy comprises two contributions,

$$f_{int}(x) \equiv f_{int}(c(x)) = f_{ev}(c(x)) + f_{st}(c(x)), \tag{3}$$

where $c(x)$ is the concentration of polymer segments and $f_{ev}(x)$ is the density of the excluded volume interactions which in the virial approximation can be presented as

$$\frac{f_{ev}(c(x))}{kT} = vc^2(x) + wc^3(x) + \cdots, \tag{4}$$

where v and w are the second and the third virial coefficients, respectively, and where we neglect all higher order terms in the following. $f_{st}(x)$ is the contribution to the free energy arising due to pair-wise association of stickers. The latter comprises the combinatorial entropy of choosing different pairs of stickers on polymer chains and the free energy gain upon association. As demonstrated in ref. (272), in a semi-dilute

polymer solution of concentration $c(x)$ the fraction of stickers associated into pairs can be found from

$$\frac{q(c(x))}{[1-q(c(x))]^2} = 2c(x)F_{st}v_b e^{\varepsilon/kT} = 2c(x)F_{st}\lambda, \tag{5}$$

and the corresponding contribution to the free energy is given by

$$\frac{f_{st}(c(x))}{kT} = F_{st}c(x)\left\{\frac{q(c(x))}{2} + \ln[1 - q(c(x))]\right\}, \tag{6}$$

where $F_{st} = N_{st}/N$ is the number of stickers per segment. The quantity $\lambda \equiv v_b e^{\varepsilon/kT}$ is an effective measure of the interaction strength between stickers. The nature of λ illustrates that both an interaction range (defined by the volume term v_b) and an interaction strength (defined by the energy term ε) are needed to describe the association of stickers. As a consequence, λ is expressed in units of volume, and we call it the 'attractive volume' of a sticker. λ must be positive and in the limiting case of $\lambda = 0$, we recover the properties of a brush without stickers. Taken together, the total density of the free energy of interactions in the brush is given from Eqs. [4] and [6] by

$$\frac{f_{int}(c(x))}{kT} = vc^2(x) + wc^3(x) + F_{st}c(x)\left\{\frac{q(c(x))}{2} + \ln[1 - q(c(x))]\right\}. \tag{7}$$

The self-consistent mean-field theory provides the expression for the chemical potential of segments in the brush as a function of the distance from the surface as (182)

$$\frac{\partial f_{int}(c(x))}{\partial c(x)}\frac{1}{kT} = \frac{3\pi^2}{8N^2a^2}(\Lambda - x^2). \tag{8}$$

This expression applies for any type of interaction in the brush provided that the chains obey Gaussian elasticity on all length scales. From Eqs. [5], [7] and [8] we obtain the relation

$$2vc(x) + 3wc^2(x) + F_{st}\ln[1 - q(c(x))] = \frac{3\pi^2}{8N^2a^2}(\Lambda - x^2), \tag{9}$$

which together with Eq. [5] constitutes a closed set of equations for the polymer density profile $c(x)$ and the fraction of closed stickers $q(x)$ as a function of the distance x from the grafting surface. The parameter Λ appearing in Eqs. [8] and [9] can be calculated using the condition of vanishing osmotic pressure

$$\Pi(x) = c(x)\frac{\partial f_{int}(c(x))}{\partial c(x)} - f_{int}(c(x)) = kT\left[vc^2(x) + 2wc^3(x) - F_{st}c(x)\frac{q(c(x))}{2}\right] \tag{10}$$

at the edge of the brush, that is at $x = H$. Hence, from the simultaneous solution of the set of two equations

$$vc^2(H) + 2wc^3(H) - F_{st}c(H)\frac{q(c(H))}{2} = 0 \text{ and} \tag{11.1}$$

$$\frac{q(H)}{[1-q(H)]^2} = 2c(H)F_{st}v_b e^{\varepsilon/kT} = 2c(H)F_{st}\lambda, \tag{11.2}$$

one obtains the values of polymer concentration $c(H)$ and the fraction of closed stickers $q(H)$ at the edge of the brush $x = H$ as a function of the set of interaction parameters v, w, F_{st} and $\lambda = v_b e^{\varepsilon/kT}$. Then, using Eq. [9] one obtains the following expression for Λ:

$$\Lambda = H^2 + \frac{8N^2 a^2}{3\pi^2}\{2vc(H) + 3wc^3(H) + F_{st}\ln[1 - q(H)]\}. \qquad [12]$$

In the absence of stickers ($F_{st} = 0$) and under good or θ-solvent conditions ($v \geq 0$), the polymer density vanishes at the brush edge, $c(H) = 0$ and $\Lambda = H^2$, whereas under poor solvent conditions ($v < 0$), vanishing of osmotic pressure requires a nonzero polymer concentration (or stepwise density drop) at the brush edge with $c(H) = -v/2w$ and

$$\Lambda = H^2 - \frac{2N^2 a^2}{3\pi^2}\frac{v^2}{w}. \qquad [13]$$

The overall brush thickness has to be determined from the normalization of the polymer density profile,

$$\langle c \rangle \equiv \frac{1}{H}\int_0^H c(x)\mathrm{d}x = \frac{N}{s^2 H}, \qquad [14]$$

where we also introduce the average segment concentration.

For the brush with stickers, it is easy to check from Eqs. [5] and [9] that the chemical potential of the polymer segments in the brush is a monotonous function of the polymer concentration $c(x)$ and that the polymer density vanishes at the edge of the brush, $c(H) = 0$ and $\Lambda = H^2$, if $v_{eff} \equiv v - v_{st} \geq 0$. Here, we have introduced the notation $v_{st} \equiv F_{st}^2 v_b e^{\varepsilon/kT} = F_{st}^2 \lambda$. An increase in either the fraction of stickers F_{st} or in the attractive sticker volume λ results in a decrease and eventually in the inversion of the sign of v_{eff}. At $v_{eff} < 0$, the polymer concentration and the fraction of closed stickers exhibits a discontinuity at the brush edge, $c(H) > 0$ and $q(H) > 0$, as follows from Eq. [12], $\Lambda < H^2$.

Remarkably, when the fraction of closed stickers is small throughout the brush ($q(x) \ll 1$), then $q(x) \approx 2c(x)F_{st}\lambda$ and the term in curly brackets in Eq. [7] reduces to $-c(x)F_{st}$ implying that the effect of stickers is equivalent to the renormalization $v \rightarrow v_{eff}$ of the second virial coefficient in a conventional homopolymer brush. That is, all structural properties of the brush with stickers can be obtained from those for the conventional homopolymer brush by simply replacing v by v_{eff}. This case has been considered in detail in ref. (182).

As a measure of the average degree of cross-linking in the brush we introduce the average fraction of closed stickers

$$\langle q \rangle = \frac{1}{H}\int_0^H q(x)\mathrm{d}x. \qquad [15]$$

Another property of interest is the free energy per chain in the brush. It can be calculated from Eqs. [1], [7] and [10] by making use of the fact that as long as the chains in the brush obey Gaussian elasticity, the local force balance leads to the relation between the density of the elastic free energy and the local osmotic pressure as $f_{\mathrm{el}}(x) = \Pi(x)/2$.

IV.3.2 Salient theoretical predictions for cross-linked brushes

To reveal salient theoretical predictions for cross-linked brushes, we consider two distinct solvent qualities, good solvent ($v = 0.5$) and θ solvent ($v = 0$), and used default values for N, s, w and v_{b} corresponding to *parameter set 1* in Table IV.1. For convenience, all relevant quantities in this section are normalized by appropriate powers of the segment length a without explicitly annotating this in text and figures. N and s were chosen such that, with v and w fixed, the chain stretching and the polymer concentration in the formed brushes are in line with the assumptions of the model over a large range of other parameters. Without loss of generality, we fix $v_{\mathrm{b}} = 0.5$, such that the attractive sticker volume λ can also be expressed in terms of the sticker strength ε (recall that $\lambda = v_{\mathrm{b}}\mathrm{e}^{\varepsilon/kT}$); this is convenient because the quantity ε (expressed in units of kT) is more intuitively accessible.

Table IV.1. Polymer brush and interaction parameters chosen for the computations.

Parameters	Values	
	Parameter set 1	*Parameter set 2*
N	1600	170.5
a	-	0.76 nm
s/a	8 (or varied)	6.65 (or varied)
v/a^3	0 (θ solvent) 0.5 (good solvent)	0.048
w/a^6	1/6	1/6
F_{st}	0.1 (or varied)	0.094
v_{b}/a^3	0.5	1
ε, λ	varied	varied
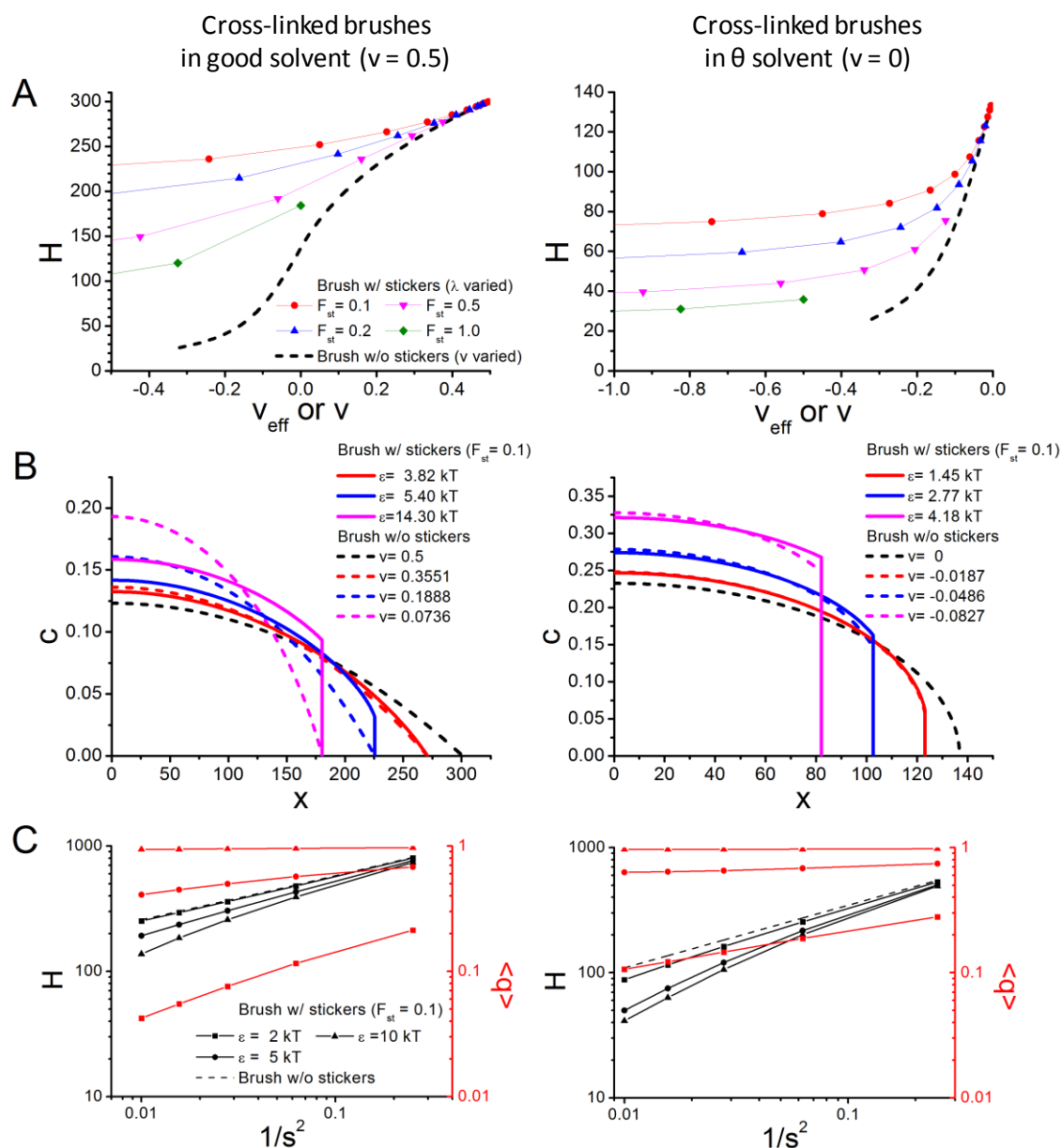
Figure IV.1 Theoretically predicted brush properties. (*A*) Brush thickness *H* vs. effective excluded volume, $v_{\text{eff}} = v - v_{\text{st}}(\lambda)$ (with varying λ) for brushes containing different fractions of stickers F_{st} (*symbols with solid lines*) in good solvent ($v = 0.5$; *left*) and θ solvent ($v = 0$; *right*). Other parameter settings are as listed in Table IV.1 (*parameter set 1*). For comparison, data for the equivalent brush without stickers as a function of excluded volume v are also shown (*dashed lines*). (*B*) Segment concentration *c vs.* distance from the grafting surface *x* at a selected fraction of stickers ($F_{\text{st}} = 0.1$). Profiles of brushes with stickers (where thickness decreases with attractive sticker volume $\lambda = v_{\text{b}}e^{\varepsilon/kT}$, expressed in ε with fixed $v_{\text{b}} = 0.5$; *solid lines*) are compared with brushes lacking stickers (where thickness decreases with solvent quality v; *dashed lines*). Matching colors indicate that ε and v, respectively, were selected such

that the brush thickness values coincide for the two different brush types. (*C*) Brush thickness *H* (*black*) and average fraction of stickers associated in pairs $\langle q \rangle$ (*red*) at a selected $F_{st} = 0.1$ and a set of selected λ (again expressed in ε) as a function of grafting density $1/s^2$ (*solid lines with symbols*); for comparison, the thickness of equivalent brushes without stickers is also shown (*dashed lines*).

IV.3.2.i   Thickness of cross-linked brushes

Figure IV.1*A* presents the dependence of the brush thickness on λ, plotted as *H* versus $v_{eff}(\lambda)$ (recall that $v_{eff} = v - v_{st}$ with $v_{st} = F_{st}^2 \lambda$) for different fractions of stickers F_{st} at $v = 0.5$ (*left panel*) and $v = 0$ (*right panel*). For comparison, the thickness of the corresponding 'reference' brush without stickers as a function of the second virial coefficient v is also shown (where the lower limit $v = -2w$ corresponds to the fully collapsed brush, i.e. $H = N/s^2 = 25$). For the sake of completeness, the dependencies of *H* on F_{st} and λ are also explicitly presented in Figure IV.S1.

As follows from Figure IV.1*A*, the thickness of the brush with stickers decreases as a function of the effective excluded volume parameter v_{eff} much weaker than the thickness of the reference brush as a function of v. Obviously, there is no universal dependence of *H* on v_{eff}, and for any given value of v_{eff} the brush thickness decreases upon an increase in the fraction of stickers F_{st}.

All curves in Figure IV.1*A* coincide though for small v_{st}. This corresponds to the regime where the fraction of stickers associated in bonds is small ($\langle q \rangle \ll 1$) and the effect of stickers on the brush structure can be effectively treated as a reduction of the solvent quality. As a control, we verified that the thickness computed in the absence of stickers ($v_{st} = 0$) is in line with expectations for homopolymer brushes (182): $H_0 = 136.8$ for $v = 0$ is in agreement with $H_0 = 4/\pi \, (w/2)^{1/4} s^{-1} N$ (eq [17] of ref. (182)); $H_0 = 300.8$ for $v = 0.5$ is slightly larger than $H_0 \approx 296$ obtained from the asymptotic expression $H_0 = 2/\pi^{2/3} \, (v/s^2)^{1/3} N$ (eq [21] of ref. (182)), which is valid in the limit of good solvent, that is, neglecting ternary and higher order interactions. The minor divergence in the case of good solvent is reasonable because Eq. [21] in ref. (182) was derived for the limit of $\beta = vs/\left(3 \cdot 2^{1/4} w^{3/4}\right) \gg 1$, whereas $\beta \approx 4.3$ in our case (cf. Table IV.1).

In the other extreme, when v_{eff} becomes very small, the thickness of the cross-linked brushes approaches a plateau. In this regime, the attractive sticker volume λ (or the

sticker strength ε) are so large that virtually all stickers are associated into bonds ($\langle q \rangle \approx 1$), and this condition defines the lower limit H_{min} for the thickness of a brush with a given number of stickers. From Figure IV.1A (and Supporting Figure IV.S1), it can be appreciated that for small F_{st}, H_{min} is relatively large. This is a consequence of the solubility of the spacer segments between stickers which keep the brush in a swollen state even if the stickers are bonding strongly.

IV.3.2.ii   Density profile of cross-linked brushes

Figure IV.1A (*left panel*) also reveals that the brush with stickers may need a negative effective excluded volume ($v_{eff} < 0$) to attain the same thickness as a partially swollen ($v > 0$) reference brush. Remarkably, brushes with and without stickers may thus have qualitatively different density profiles at the same (sufficiently small) thickness. To illustrate how the segment density profile evolves as cross-links become stronger, we fixed the number of stickers per segment to $F_{st} = 0.1$, and varied ε (and thus λ) such that brush thickness values $H = 0.90H_0$, $0.75H_0$ and $0.60H_0$ were obtained (Figure IV.1B, *colored solid lines*). As one can see, the segment density c decreases monotonously with distance from the grafting surface, and the brushes become more compact as the sticker association strength increases. The segment density vanishes smoothly at the brush periphery for the reference brushes and also for small ε (and λ) in good solvent (i.e. where $v_{eff} \geq 0$), whereas a discontinuous drop of density emerges as ε (and λ) become larger ($v_{eff} < 0$).

For comparison, density profiles for the sticker-free reference brush at specific values of v corresponding to the same thickness of the reference brushes as for the brushes with stickers are plotted as dashed lines. In accordance with our observation in Figure IV.1A, the comparison reveals that stickers produce a discontinuity in c at larger H than a decrease in solvent quality would (cf. Figure IV.1B, *left*). More generally it is clear that, for a given brush thickness, cross-links make the density profile more box-like than a reduction in solvent quality (Figure IV.1B), and a few strong cross-links make the profile more box-like than many weak cross-links (Supporting Figure IV.S2). The differences are pronounced when the cross-linked brushes are in good solvent (Figures IV.1B and S2, *left*), and only minor in θ solvent (Figures IV.1B and S2, *right*). As controls, profiles of the corresponding brushes without stickers are also shown in Figure IV.1B (*black solid lines*): the profile for $v = 0.5$ indeed shows the parabolic

shape ($c \sim 1 - x^2/H^2$) characteristic for brushes in good solvent, and the profile for $v = 0$ shows the expected $c \sim \sqrt{1 - x^2/H^2}$ dependence (182).

IV.3.2.iii   Effects of grafting density on sticker association and brush thickness

To assess how the grafting density affects the cross-linking of brushes, we calculated the brush thickness H and the average fraction of stickers associated into bonds $\langle q \rangle$ as a function of $1/s^2$ for selected values of λ (corresponding to $\varepsilon/kT = 2, 5,$ and 10 at $v_b = 0.5$), a fraction of stickers $F_{st} = 0.1$, and otherwise unchanged parameters (Figure IV.1C). It can be seen that $\langle q \rangle$ varies from around 10% at $\varepsilon = 2kT$ to almost 100% at $\varepsilon = 10kT$, i.e. the range $2kT \leq \varepsilon \leq 10kT$ covers almost the full spectrum of possible brush conformations. Both H (*black solid lines*) and $\langle q \rangle$ (*red solid lines*) increase monotonously with grafting density. The thickness of the equivalent brush without stickers is also shown in Figure IV.1C (*black dashed lines*) for comparison. From the log-log plot, one can appreciate that the dependence of brush thickness on grafting density obeys a power law relationship for brushes without stickers. The power is 0.5 for $v = 0$ and 0.356 for $v = 0.5$. These values are comparable to theoretical predictions of 1/2 for θ solvent and 1/3 for good solvent according to ref. (182), where the minor discrepancy for good solvent is again due to the fact that the parameter β is only a few fold larger than 1 in our case. With stickers, the power-law dependence is lost and a more complex behavior emerges. As expected, the thickness of the brush with stickers is smaller than that of the reference brush for any given grafting density. The relative difference, however, decreases with grafting density due to a concomitant increase in the strength of repulsive excluded volume interactions. The interplay of different interactions gives rise to apparent powers of the H versus $1/s^2$ dependency for the brush with stickers that are larger than for the equivalent brush without stickers.

IV.4   EXPERIMENTS

IV.4.1   Formation of synthetic FG domain brushes

The approach to form films of grafted FG domains and study their properties has been established previously (167, 180, 271, 281), and is schematically presented in Figure IV.2A. The different neo FG domains (FSFG, GLFG, GSFG, and the reference SSSG) were attached through their N-terminal histidine tag to Ni^{2+}-loaded NTA moieties on a supported lipid bilayer (SLB). Figure IV.2B-E demonstrate that all neo FG domain types bound stably (i.e. were not released upon rinsing in buffer), and that

the SLB also serves as an effective passivation layer: the FG domains could be fully eluted in 0.5 mM imidazole indicating that the His tag is the only moiety through which the FG domains bind to the surface thus providing a well-defined mode of attachment.

In our experiments, we used an in situ combination of SE and QCM-D to study the properties of the end-grafted FG domain films (276, 281). For this purpose, we simultaneously acquired, on the same sensor, the ellipsometric angles (Δ and ψ; optical signal) and the QCM-D frequency and dissipation shifts (Δf and ΔD; acoustic signal; Figure IV.2*B-E*, *bottom panels*). FG domain grafting densities (Figure IV.2*B-E*, *top panels*) were obtained through optical modeling of SE data, whereas the thickness of the corresponding films was obtained through viscoelastic modeling of QCM-D data (see Materials and Methods for details).

IV.4.2 Mechanical properties, thickness and concentration of synthetic FG domain brushes

The mechanical properties of FG domain films can be appreciated from Figure IV.3*A*, where the parameter $\Delta D/-\Delta f$, which can be computed from the QCM-D data without any fitting, is proportional to the elastic compliance to a first approximation, and thus a measure of film softness (161, 180). The graph demonstrates that all FG domain films become stiffer as the grafting density increases. This trend is expected, because the increase in grafting density entails an increase in the polymer concentration, and polymer meshworks tend to stiffen with concentration (175). Importantly, there are significant differences in stiffness as a function of FG motif type: at any given grafting density, SSSG films are softest and films become gradually stiffer from GSFG to GLFG to FSFG. This provides a first and robust indication about the differences in the cross-linking propensity of the synthetic FG domains, and identifies FSFG as being the most cohesive motif.
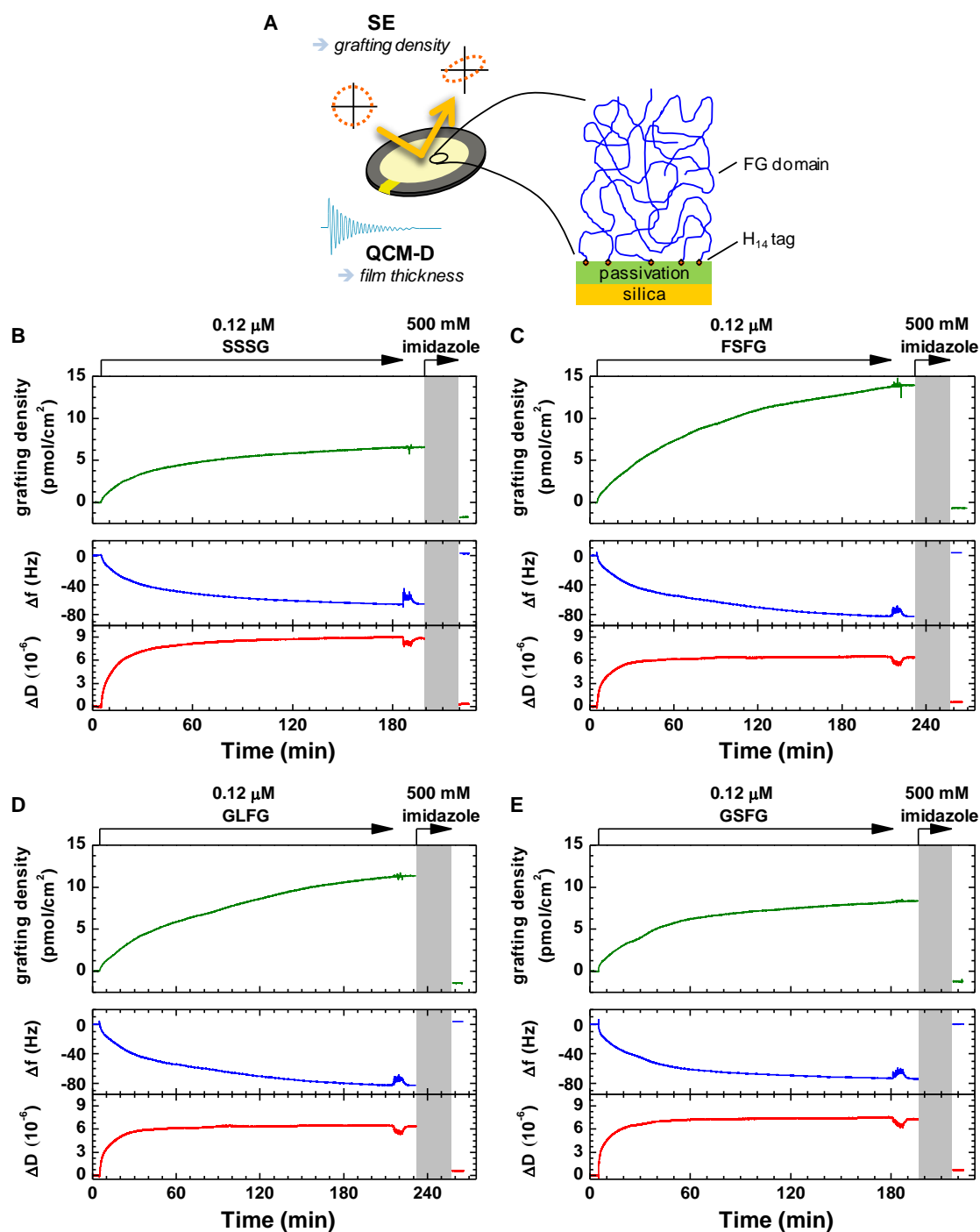
Figure IV.2 (*A*) Schematic illustration of the experimental approach and the FG domain film architecture. (*B-E*) FG domain film formation and properties. FG domain grafting densities (*upper graph*; obtained from SE data) are shown together with QCM-D frequency and dissipation shifts (Δf and ΔD; *lower graphs*). Arrows on top of each panel indicate the start and duration of incubation with different sample solutions, for SSSG (*B*), FSFG (*C*), GLFG (*D*) and GSFG (*E*) domains; during remaining times, the surface was exposed to working buffer. All FG domains remained stably bound upon rinsing in working buffer. Full elution after treatment with imidazole (*grey shaded area*,

not monitored) demonstrates that the FG domains bound specifically through their H_{14} tags. The perturbations in the SE and QCM-D signals right after the end of FG domain incubation are due to transient temperature fluctuations caused by solution exchange and do not represent changes of the FG domain films.
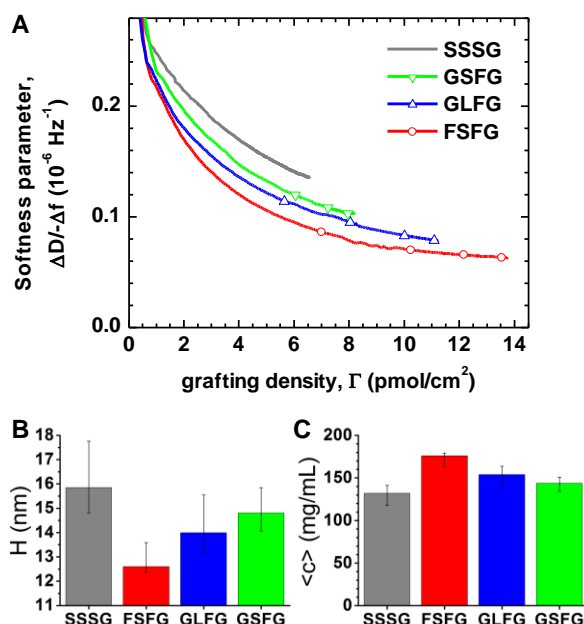
Figure IV.3 (*A*) FG motifs differentially stiffen the FG domain film. The parameter $\Delta D/-\Delta f$ (obtained from QCM-D data) is a measure of the films' softness (or elastic compliance) and plotted here as a function of grafting density Γ (determined from SE data). (*B*) Experimentally determined best-fit thickness H of different types of FG domain films determined by viscoelastic modeling of QCM-D data obtained at a grafting density of 6.5 pmol/cm^2. The error bars represent 1σ confidence intervals obtained from the fitting procedure. (*C*) Average FG domain concentration $\langle c \rangle = \Gamma M_W/H$, derived from *B*.

Figure IV.3*B* shows the thickness H of the four brushes at a selected grafting density ($\Gamma = 6.5$ pmol/cm^2), and Figure IV.3*C* shows the average concentration Γ/H in mg/mL. From SSSG to GSFG to GLFG to FSFG, the thickness gradually decreases, and the concentration increases. This is fully consistent with the stiffness trends, and thus provides confidence in the robustness of the thickness data despite the relatively large confidence intervals associated with the data fitting. The film thickness values exceed the rms distance between adjacent anchors ($s = 5.05$ nm at $\Gamma = 6.5$ pmol/cm^2) by 2.5 to 3 fold, indicating that the chains are partially stretched away from the grafting surface

and thus form a so-called polymer brush. Moreover, the FG domain concentrations are on the order of a few 100 mg/mL, and it can be readily calculated that this corresponds to FG motif concentrations between 65 and 85 mM depending on the FG domain type. These values are comparable in their order of magnitude to what we have previously reported for self-assembled films (180, 271, 281) and microgels (254) of native FG domains, and to the conditions that are likely to be present inside the nuclear pore. Therefore, the inter-FG-motif interactions with our artificial FG domains occur at close-to-physiological local protein and FG motif concentration levels.

IV.5   CORRELATING THEORY WITH EXPERIMENTS

Towards quantitative comparison with experiment, we performed calculations with *parameter set 2* in Table IV.1. In this section, we consider the segment size explicitly in all quantities, to facilitate correlation with the experiment. Specifically, segments were taken to be twice the size of an amino acid ($a = 0.76$ nm), mirroring the flexibility of unfolded polypeptide chains (282). $N = 170.5$ is half the number of amino acids per FG domain construct, and with 16 stickers per chain, we have $F_{st} = 0.094$. We fixed $w/a^6 = 1/6$, and the default rms distance between grafting points $s/a = $ 5.05 nm$/a = 6.65$ is equivalent to a grafting density of $\Gamma = 6.5$ pmol/cm^2.

Using these parameters, and the experimentally measured thickness of the SSSG reference brush at 6.5 pmol/cm^2 (Figure IV.3*B*), we can calculate the second virial coefficient $v/a^3 = 0.048$. This value should be considered an average effective excluded volume per segment, in the sense that it was derived by representing the reference polypeptide sequence as a homopolymer. We note here that the effective hydrodynamic thickness measured by QCM-D may not be fully equivalent to the thickness defined in the theory, and v should thus be considered an estimate that provides the correct order of magnitude. v/a is positive but clearly much smaller than 0.5 which would be expected for a fully solvated polymer. This indicates that there is a net attraction between the polymers even in the absence of authentic stickers, and that our experimental conditions are rather close to θ conditions.
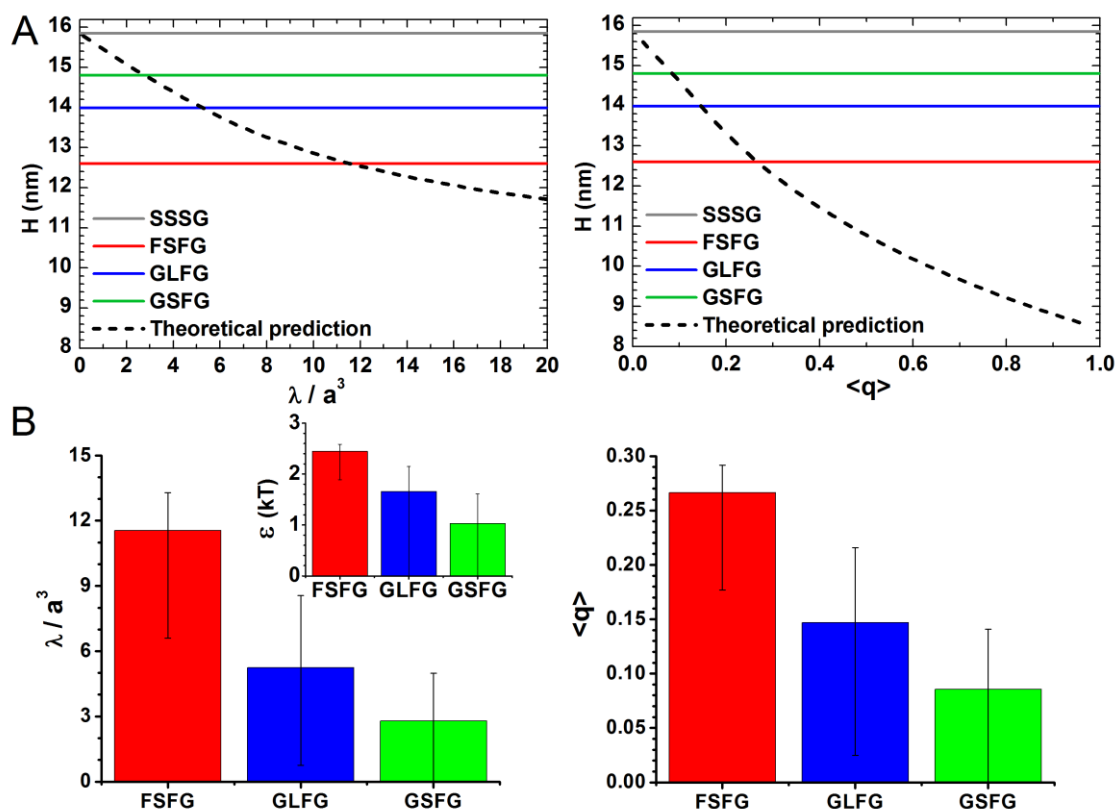
Figure IV.4 (*A*) Theoretical predictions (*dashed lines*) of brush thickness *H vs.* attractive sticker volume λ (*left*) and *vs.* the fraction of stickers engaged in bonds $\langle q \rangle$ (*right*) for a cross-linked brush at 6.5 pmol/cm^2 with parameters chosen to match the neo FG domains used in the experiments (cf. Table IV.1, *parameter set 2*). Horizontal lines represent the best-fit thickness of SSSG (*grey*), FSFG (*red*), GLFG (*blue*) and GSFG (*green*) domain films taken from Figure IV.3*B*. (*B*) λ/a^3 (*left*) and $\langle q \rangle$ (*right*) obtained by matching theory and experiment as illustrated in *A*. Error bars were determined from the confidence ranges in the experiment for the thickness of FSFG, GLFG and GSFG as shown in Figure IV.3*B*. The *inset* shows the sticker association energy ε obtained from λ, assuming $v_b/a^3 = 1.0$.

IV.5.1 Estimating the density and strength of cross-links

Figure IV.4*A* shows the theoretically predicted brush thickness (*dashed lines*) as functions of the attractive sticker volume λ (*left panel*) and the average fraction of stickers engaged in bonds $\langle q \rangle$ (*right panel*) together with the best-fit experimental thickness values for the four FG domain constructs (*horizontal lines*; cf. Figure IV.3*B*) at 6.5 pmol/cm^2. The correlation of experiment with theory thus provides estimates of λ and $\langle q \rangle$ for the FSFG, GLFG and GSFG domain brushes. These quantitative data,

117

summarized in Figure IV.4*B*, are a major result of this study. They reflect the expected trends, with FSFG having the largest attractive sticker volume and the largest number of bonds. A salient feature for all tested brushes is that only a minor fraction of stickers associate into bonds, whereas 75% and more of the stickers effectively remain free. We do not know the exact value of v_b, but if we consider that a sticker spans two segments (or four amino acids) and assume that the geometrical excluded volume of the sticker defines the volume for bond formation, then this would correspond to $v_b/a^3 = 1.0$. With this assumption, we obtain bond formation energies ε in the range of a few kT (Figure IV.4*B*, *left panel*, *inset*). In particular, the sticking energy of 2.4 kT for FSFG corresponds to an affinity $K_d = e^{-\varepsilon/kT} \times 1\,\text{M} \approx 90\,\text{mM}$. Moreover, the order of magnitude of the estimated v_b is very likely to be correct, and since $\lambda = v_b e^{\varepsilon/kT} = v_b/K_d \times 1\,\text{M}$ this implies that the affinity is also correct to within an order of magnitude. Therefore, we can conclude that individual inter-FG-motif interactions have an affinity above 10 mM and are thus rather weak compared to common biospecific interactions.
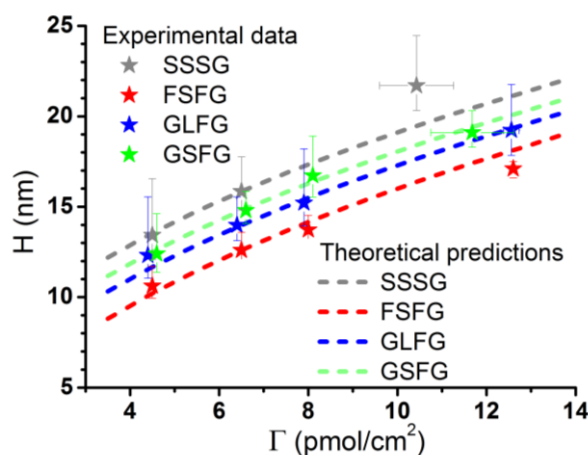
Figure IV.5 Theoretical predictions (*dashed lines*) and experimental results (*symbols*) for the thickness of brushes formed from different FG domains (as indicated in the graph) *vs.* grafting density Γ. Experimental data at 4.5, 6.5 and 8.0 pmol/cm^2, and at 12.5 pmol/cm^2 for FSFG, were obtained from combined QCM-D/SE measurements (Figure IV.3). To avoid overlap of the symbols and error bars, data at 4.5, 6.5 and 8.0 pmol/cm^2 were displaced along the *x* axis by small amounts. Experimental data at larger grafting densities for SSSG, GSFG and GLFG were obtained from separate QCM-D measurements, and the grafting density in this case was estimated by correlation of the Δ*f* value with extrapolated Δ*f* *vs.* Γ calibration curves obtained from the combined

SE/QCM-D measurements (see Supporting Figure IV.S3 for details). For the theoretical calculations, the best-fit λ values in Figure IV.4B, obtained at 6.5 pmol/cm^2, were used with other parameters defined in Table IV.1 (*parameter set 2*).

To further validate our analysis, we determined the thickness of the synthetic FG domain brushes experimentally for selected grafting densities spanning from 4.5 to 13 pmol/cm^2, and compared the results with theoretical predictions for the brush thickness with all input parameters fixed to the above-established values. The consistent match within the experimental uncertainty revealed in Figure IV.5 provides additional support to the applicability of the theoretical model to our experimental system.
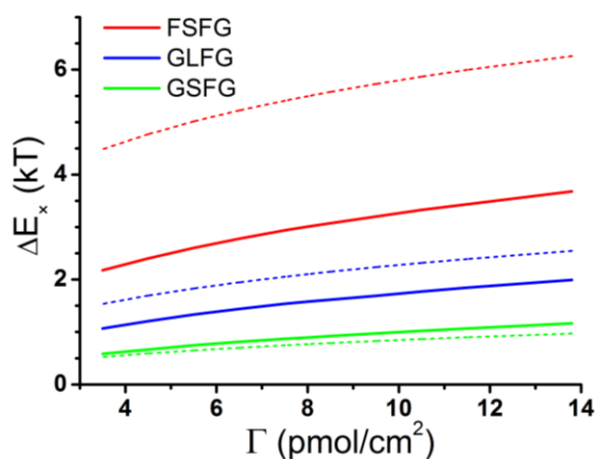
Figure IV.6 Free energy predictions. *Solid lines* are predicted gains in free energy $\Delta E_\times$ per chain in the cross-linked neo-FG-domain brushes compared to the sticker-free SSSG reference brush as a function of grafting density Γ. *Dashed lines* in corresponding colors represent the total binding energy of the engaged stickers, which is $\varepsilon\langle q\rangle N_{\mathrm{st}}/2$. Values were obtained based on the theoretically predicted thickness values shown in Figure IV.5, and assuming $v_{\mathrm{b}}/a^3 = 1.0$.

IV.5.2 Free energy gains upon cross-linking

Using the derived parameters, it becomes possible to explore the free energy balance upon assembly of the neo FG domains. Figure IV.6 (*solid lines*) shows the theoretically predicted free energy gains $\Delta E_\times$ per polymer chain in the cross-linked neo-FG-domain brushes compared to the sticker-free SSSG reference brush. It can be seen that this quantity increases rather weakly with grafting density and is typically small, in the range of a few kT. A comparison with the total binding energy of the engaged stickers $\varepsilon\langle q\rangle N_{\mathrm{st}}/2$ (*dashed lines* in matching colors) reveals that other contributions to the free

energy are significant, and that these can be positive or negative. Apparently, the reduction in elastic energy and the enhancement in excluded volume interactions upon cross-linking balance such that they make for a net extra energy gain in the case of GSFG whereas there are penalties for GLFG and FSFG. Reassuringly, the magnitude of $\Delta E_\times$ is consistent with previously reported results obtained with brushes of the FG domains of the native nucleoporin Nsp1 (180).

IV.6   DISCUSSION

We have developed an analytical mean-field theory to predict the morphology of physically cross-linked brushes and, by correlating theory with experiment, estimated (i) the effective excluded volume of the FG-motif free reference polymer, (ii) the binding strength of inter-FG-motif interactions, and (iii) the morphology and degree of cross-linking of neo-FG-domain films. The main results are that the reference polymer effectively behaves like a homopolymer close to θ conditions ($v \approx 0$), that the interaction of individual FG motifs is relatively weak ($K_d \gtrsim 10$ mM), and that only a relatively small fraction of FG motifs is simultaneously engaged in cross-linking ($\langle q \rangle \lesssim 25\%$).

It is likely that, on a qualitative level, these findings are also valid for native FG domains at the concentrations that prevail inside the nuclear pore complex. A case in point is the Nsp1 FG domain which is 600 amino acids (or 300 polymer segments) long and features 33 FG motifs (18 FSFG and 15 other). We have previously reported the thickness of films made from Nsp1 and from a FILV→S mutant in which all hydrophobic amino acids were replaced by the hydrophilic serine (Figure IV.3*B* in ref. (180)). Using the here-described method, we can estimate $v/a^3 = 0.21$ from the Nsp1 FILV→S film thickness, which is moderately larger than for our regular SSSG construct yet again closer to zero than to the value of 0.5 expected for a polymer in good solvent. The fraction of stickers per segment in Nsp1 is $F_{st} = 0.11$, and the thickness of the Nsp1 brush was reduced by approximately 25% compared to the FILV→S analogue. Both values compare favorably with our neo FSFG domain, where $F_{st} = 0.094$ (cf. Table IV.1) and $H_{FSFG}/H_{SSSG} \approx 0.8$ (cf. Figure IV.5), indicating that the mean sticker strength in Nsp1 is comparable to the sticker strength in our neo FSFG domain. Moreover, we also found that both neo FSFG domains and Nsp1 FG domains form macroscopic hydrogels whereas the respective F→S and FILV→S analogues do not.

Taken together, the correlation of the morphological effects of FSFG motifs in the neo-FG-domain with FG motifs in the Nsp1 context is remarkably good. We thus propose that the results obtained here can be generalized to native FG domains.

Evidently, native FG domains are diverse: they vary not only in FG motif type (FxFG, GLFG and other) and the mean density and distribution of FG motifs along the chain but also in the nature of the sequences that flank the FG motifs and more generally in the composition of the spacer sequences. These variations may well modulate the morphology of FG domain assemblies locally (e.g. as a function of distance from the equator of the NPC (283)). Systematic studies will be needed to resolve this question, where tailored regular neo FG domains can reveal, for example, how important the flanking sequences are for the affinity between FG motifs.

IV.6.1 Implications for the morphology of FG domain assemblies and the permeability barrier

In previous works (180, 281), we had analyzed the cohesive interactions between FG domains using theoretical models that treat FG domains as regular polymers where all interactions are effectively smeared out homogeneously along the polymer chain. In our new, extended model, we consider the discreteness of stickers explicitly, and this revealed that the homopolymer approximation describes brush thickness and density profiles well in the limit of weak stickers ($\langle q \rangle \ll 1$), but increasingly fails as the stickers become stronger ($\langle q \rangle \rightarrow 1$) (Figure IV.1*A-B*). The $\langle q \rangle$ values for our neo FG domains are moderate to small (Figure IV.4*B*, *right panel*). We can hence conclude that the homopolymer approximation, despite its simplicity, is satisfactory for predicting the brush thickness and density profiles for all neo FG domains used here, and most likely also for native FG domains. In particular, the effect of discrete cross-links to make brushes more box like (Figures IV.1*B* and S2) is likely to be marginal for FG domains, not only because $\langle q \rangle$ is moderate but also because the equivalent sticker-free polymers are like homopolymers close to θ conditions.

In the computational model by Zahn, Osmanovic et al. (281), we quantified the effective attractive interaction between homopolymer segments by the parameter $\varepsilon_{\mathrm{pp}}$, and reported $\varepsilon_{\mathrm{pp}} = 0.030\,kT$ for the neo FSFG domain. A comparison of the predictions of this model (Figure IV.3*B* in ref. (281)) with the thickness of the reference SSSG film (Figure IV.5) reveals that FG motifs contribute only approximately $0.008\,kT$ to this energy term. Thus, only about 25% of the attraction between neo FSFG

domains comes from the FG motifs, whereas the rest is intrinsic to the (sticker-free) polymer itself. In our new model, attractive interactions reduce the excluded volume and, unsurprisingly, we see an equivalent effect: the reduction in excluded volume due to attraction between SSSG polypeptides compared to polymers in good solvent ($\Delta v/a^3 = 0.5 - 0.048 \approx 0.45$) is larger than the additional effect of the FSFG stickers ($v_{st}/a^3 = F_{st}^2 \lambda/a^3 = 0.10$; recall that $v_{eff} = v - v_{st}$). These comparisons highlight that not only FG motifs but also the spacer regions between them contribute significantly to the cohesion of FG domains.

IV.6.2 Implications for the permselectivity mechanism of the permeability barrier

NTRs are known to be strongly enriched in the nuclear pore. Next to inter-FG-domain interactions, the morphology and function of the permeability barrier are thus also defined by NTR•FG domain interactions, and it is instructive to compare the two. Since inter-FG-domain as well as NTR•FG domain interactions are mediated by FG motifs and intrinsically multivalent, we need to discriminate the *affinity* of individual inter-FG-motif and NTR•FG motif interactions from the *avidity* of multivalent inter-FG-domain and NTR•FG domain interactions.

Milles et al. (259) recently determined dissociation constants of individual NTR•FG motif interactions in the context of a 78 amino acid long FG-rich strand of Nup153 and found these to scatter around 1 mM irrespective of the NTR type for all FG motifs in the sequence. With an equivalent strand in which all but one of the strongest binding FG motifs were impaired by F→A mutations, the K_d of the remaining NTR•FG motif interaction increased to 7 mM. Collectively, these data would suggest that individual NTR•FG motif interactions have K_d values in the lower 10 mM range. This is comparable to (or slightly smaller than) the affinity of individual inter-FG-motif interactions determined here, and implies that these two types of interactions can effectively compete with each other.

How important is this competition? Based on work with two selected NTRs (importin β and NTF2) and three selected FG domains (Nsp1, Nup98 and neo FSFG), we have previously estimated that, within the range of physiological NTR and FG domain concentrations, less than 20% of all FG motifs within FG domain assemblies are simultaneously engaged in NTR binding (281). We show here that the fraction of FG motifs engaged in inter-FG-domain interactions is also unlikely to exceed a few 10%

(Figure IV.4*B*, *right panel*). Extrapolated to other FG domains and NTRs, this would suggest that the total number of available FG motifs available in the NPC is more than sufficient to allow for simultaneous FG-domain cross-linking and NTR binding.

However, the local arrangement of the participating molecules also affects multivalent interactions and thus the avidity of NTR•FG domain and inter-FG-domain interactions. We propose that it is at this level that competing effects come into play. Our recent finding that NTRs bind to FG domain films with negative cooperativity (281) supports this hypothesis. Specifically, we had attributed the negative cooperativity to the effect of excluded-volume interactions and entropic costs of NTR absorption that, in turn, reduce the conformational freedom of the grafted and flexible FG domains. It can hence be expected that NTR binding also effectively reduces the avidity of inter-FG-domain interactions. The reduction in direct interactions between FG domains does not imply an opening of the permeability barrier though, because cross-links between two FG motifs are effectively replaced by FG-motif•NTR•FG-motif cross-links.

Another important aspect of permselectivity is the dynamics of interactions. Milles et al. revealed NTR•FG motif interactions to be ultrafast (259). The rates of individual inter-FG-motif interactions are, to our knowledge, not known, but the low affinity of these interactions and the small number of amino acids involved suggest that they are also very fast, possibly as fast as (or even faster than) NTR•FG motif interactions. With all elementary interactions being short lived, it can thus be expected that the nuclear pore permeability barrier is highly dynamic.

Taken together, the emerging picture is that NTR•FG motif and inter-FG-motif interactions co-exist. The short lifetime of all elementary interactions facilitates rapid local rearrangements of the FG domain/NTR assembly and thus uptake and permeation of nuclear transport receptors (NTRs) and their cargo. At the same time, the multivalency of NTR•FG domain interactions ensures adequate avidity to enrich NTRs in the permeability barrier (thus enhancing their translocation compared to other molecules of comparable size) and, together with the multivalent cohesive interactions between FG domains, reduces the effective mesh size of the permeability barrier (thus limiting the size of molecules that can permeate unhindered and optimizing size selectivity (180)).

IV.6.3 Validity of the theory

Our mean-field theory of physically cross-linked brushes predicted the experimentally observed film thickness trends well (Figure IV.5) yet clearly remains a simplified representation of the experimental neo-FG-domain brushes. Some simplifications such as the assumption of the sticker-free reference polymer to be homogeneous were made deliberately to be able to focus on generic features. Others were needed to arrive at simple analytical expressions that reveal key parameters and their dependencies without the need for heavy computational work.

Firstly, we assumed the chains to obey Gaussian elasticity on all length scales. This approximation is likely to hold as long as the density of bonds (determined by F_{st} and q) is small. This is the case in our experiments, but implies that theoretical predictions (Figures IV.1 and S1-2) in cases where both F_{st} and λ are large are unlikely to be matched by any experiment.

Secondly, the model relies on the strong stretching approximation. In our experiments (Figure IV.5), this is the case at the higher grafting densities (were $H \gg s$) but only marginally so at the lowest grafting densities (were $H \gtrsim s$) (284). However, since the cross-linked neo-FG-domain brushes are rather compact with a box-like profile, excluded volume effects will dominate over elastic effects, and our model therefore is expected to give reasonable results even if the brush is not much thicker than the Flory radius of the polymer chains.

Thirdly, the value used for the third virial coefficient w is a reasonable guess that cannot be confirmed experimentally, and we also assumed the effective thickness determined from the QCM-D data to be equivalent to the thickness defined in the theory. The impact of these assumptions on the determination of λ (and thus ε and K_d) and $\langle q \rangle$ is likely to be small, because the trends in experimental and theoretical thickness are likely to be comparable, and moderate systematic deviations in w and H would affect the reference SSSG brush and the neo-FG-domain brushes to similar extents.

Finally, we considered binary associations between stickers and up to ternary excluded volume interactions. The neglect of all higher-order interactions appears appropriate for the analysis of our experiments, given that the normalized polymer concentrations inside the brushes remain moderate ($\langle c \rangle < 0.4/a^3$, equivalent to < 0.3 mg/mL), but the theoretical predictions at the highest concentrations in Figures IV.S1-2 will need to be considered with caution.

Taken together, we can conclude that the theoretical model represents our experimental system well and therefore expect the derived values for the strengths of inter-FG-motif interactions and $\langle q \rangle$ to be reasonably accurate.

IV.6.4 Future applications of the theory

The theory presented here is valid for physical (i.e. reversibly) cross-linked brushes, for which the degree of cross-linking will adjust dynamically as environmental factors such as solvent quality or grafting density are modified (Figure IV.1C). This case is distinct from chemically (i.e. covalently) cross-linked brushes, where not only the number of cross-links but also the conditions under which the cross-links are introduced can appreciably influence the brush morphology ('memory effect'), as pointed out in recent theoretical work by Lang et al. (285).

The nuclear pore permeability barrier that we have considered here is not the only biological system bearing resemblance to a physically cross-linked brush. Another salient example is pericellular coats rich in the polysaccharide hyaluronan (HA). This case is somewhat different from the case considered here in that soluble HA-binding proteins constitute the cross-linking nodes (26, 28), and that the local stiffening of HA chain makes the properties of the sticker-free brush distinct (20). These features could be captured by future extensions of the model presented here.

The predictions of our theory of physically cross-linked brushes also make it possible to rationally design novel synthetic polymer brushes with tailored stimuli-responsive properties that could be useful in a broad range of applications. For example, morphological changes upon cross-linking of brushes by soluble target molecules that are selectively captured by recognition elements on polymers may be exploited for biological or environmental sensing, and the modulation of cross-linking in polymer-filled channels by environmental stimuli could be used to switch molecular transport and sieving. Here, the range of high $\langle q \rangle$ should be particularly interesting because new morphologies become feasible that cannot be produced with homopolymers and simple variations in solvent quality. In contrast to physical hydrogels, for which a wide range of synthetic routes and applications have already been established (286), the current literature on polymer brushes with discrete, reversible cross-links is sparse and much remains to explore, though at least one work (287) has demonstrated how such brushes can be produced synthetically.

IV.7 CONCLUSION

We have developed a mean-field theory to describe the morphology of physically cross-linked brushes. The theory predicts that the compaction and changes in the density profile due to cross-links is equivalent to an effective reduction in excluded volume, by $v_{\mathrm{st}} = F_{\mathrm{st}}^2 \lambda$, for weak stickers ($\langle q \rangle \ll 1$) whereas a qualitatively new behavior arises for stronger stickers. Specifically, a desired modulation of brush thickness can be achieved with either a few strong stickers or many weak stickers, but a few strong stickers make the brushes more box-like than many weak stickers. The theoretical model should be of interest for the design of synthetic brushes with novel 'smart' properties, but also to understand morphological remodeling and transport phenomena in biological systems, such as the nuclear pore permeability barrier and glycan-rich or mucosal cell coats.

By using the theory to analyze experimental data on regular neo-FG-domain brushes we revealed that individual inter-FG-motif interactions are rather weak ($K_{\mathrm{d}} > 10$ mM) and that only a fraction of FG motifs is simultaneously engaged in cross-links at FG domain concentrations that are likely to prevail in the NPC. From this analysis a model for permselectivity emerges in which the individual inter-FG-motif and NTR•FG-motif interactions all are of *low affinity* thus rendering the permeability barrier highly dynamic and enabling rapid NTR translocation, whereas the *avidity* of the collective inter-FG-domain and NTR•FG-domain interactions is tuned to simultaneously promote (i) the formation of a size-selective meshwork and (ii) selective entry (and thus translocation) of NTRs with their cargo. Our soft matter physics approach thus contributes important information towards understanding the mechanism of selective gating of nucleo-cytoplasmic transport.

IV.8 SUPPORTING MATERIAL
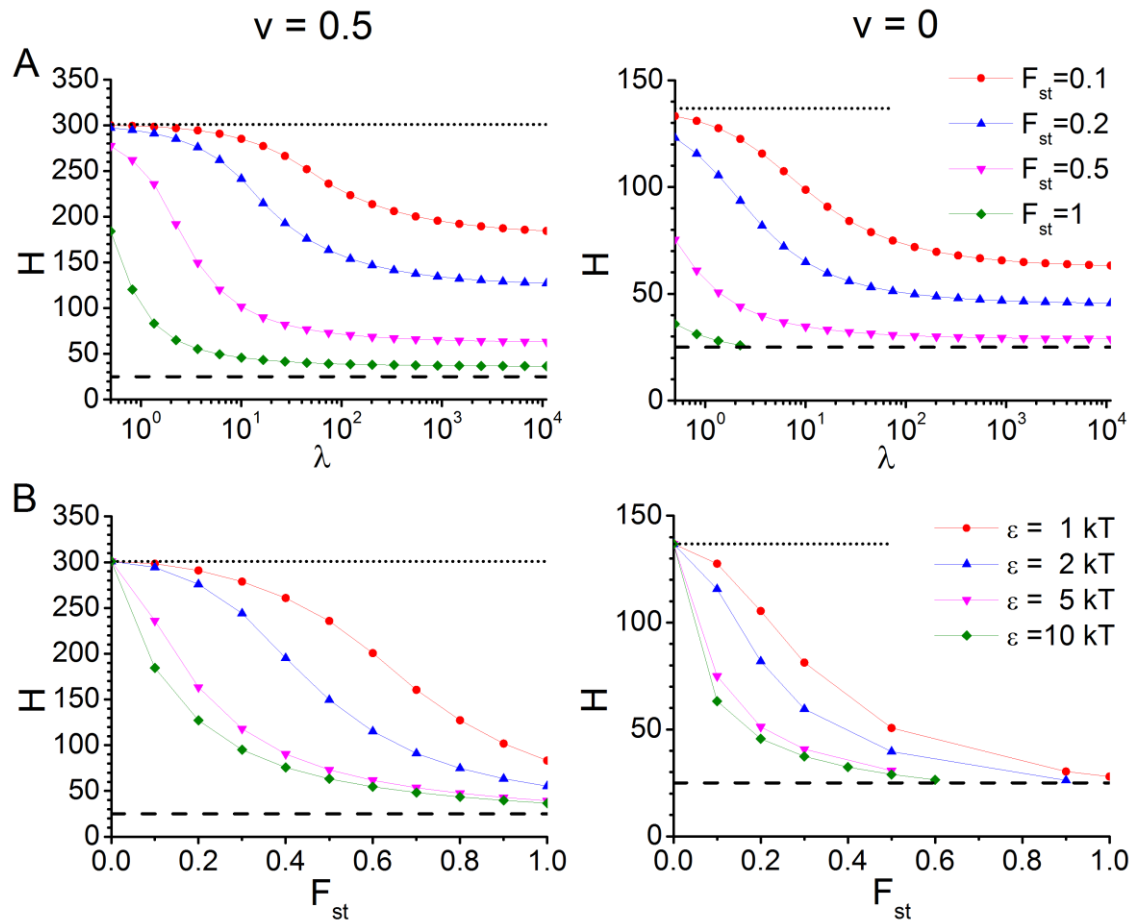
Figure IV.S1 Effect of stickers on the brush thickness. Theoretically predicted brush thickness H as function of the attractive sticker volume $\lambda = v_b e^{\varepsilon/kT}$ (for selected numbers of stickers per segment F_{st}; A), and as a function of F_{st} (for selected λ, expressed as ε with fixed $v_b = 0.5$; B) for brushes in good solvent ($v = 0.5$; *left*) and θ solvent ($v = 0$; *right*). The dotted lines on the top represent the thickness of the brush without stickers (reached at $\lambda = 0$), and the dashed lines on the bottom the thickness of the fully collapsed brush ($N/s^2 = 25$). ε and F_{st} are indicated in the figure, and all other parameter settings are listed in Table IV.1 (*parameter set 1*).
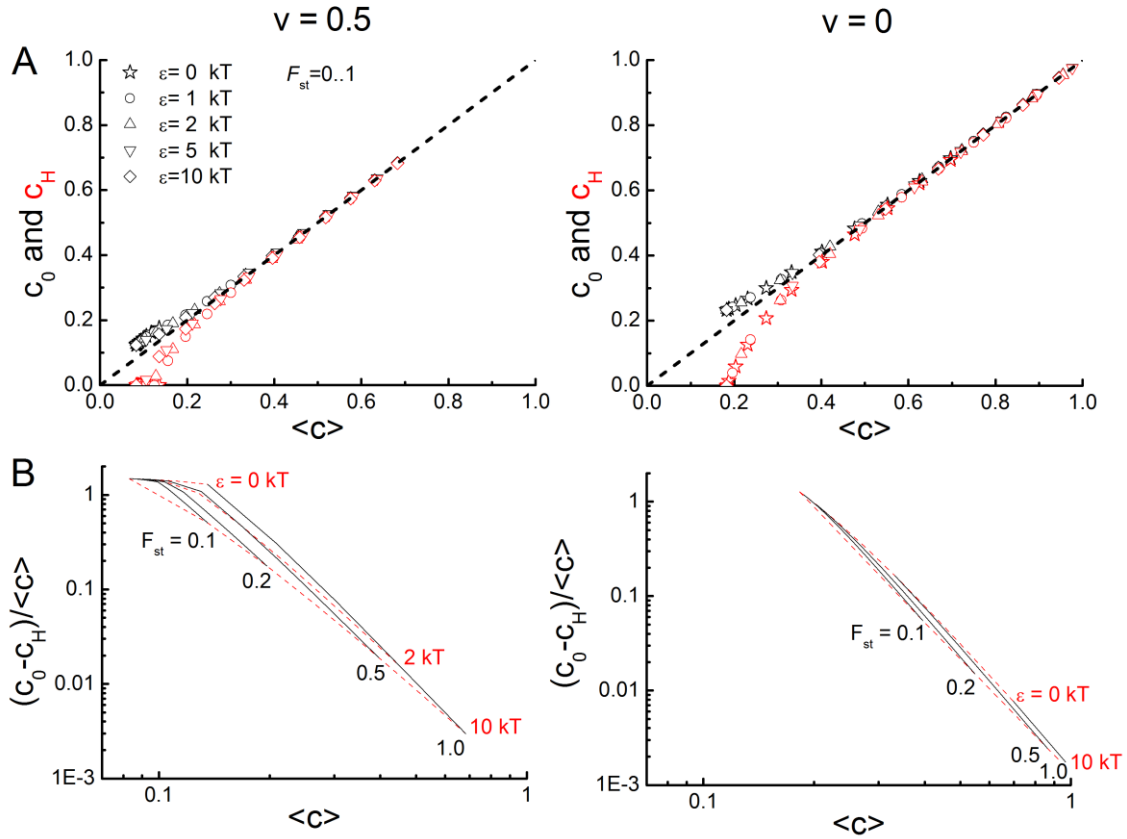
Figure IV.S2 Effect of stickers on the brush density profile. We exploited the parameters $c_0 = c(x = 0)$ and $c_H = c(x = H)$, compared to the average density $\langle c \rangle$, as quantitative measures of the shape of the segment density profile. The information provided by c_0 and c_H can be appreciated by considering the extreme case of a 'box' profile, where the density is constant throughout the brush and drops to zero at $x = H$. In this case, $c_0 = \langle c \rangle = c_H$. On the other hand, it is clear that in the general case $c_0 \geq \langle c \rangle \geq c_H$ because the density profile decreases monotonously with x under all conditions, and that c_0 and c_H will increasingly diverge from $\langle c \rangle$ as the brush becomes less compact. The relative deviations of c_0 and c_H from $c_0 = \langle c \rangle = c_H$, therefore, are two interrelated measures for the homogeneity of the brush. The quantity $(c_0 - c_H)/\langle c \rangle$ merges these into a single number, and the smaller $(c_0 - c_H)/\langle c \rangle$ the more box-like the density profile.

(A) c_0 (black symbols) and c_H (red symbols) over the range $0 \leq F_{st} \leq 1$ (in steps of 0.1) for selected $\lambda = v_b e^{\varepsilon/kT}$ (expressed as ε with fixed $v_b = 0.5$) as a function of $\langle c \rangle$ for brushes in good solvent ($v = 0.5$; left) and θ solvent ($v = 0$; right). All other parameter settings are listed in Table IV.1 (parameter set 1). The 'box profile' limit is shown as dashed lines for reference. (B) Selected data from A presented as $(c_0 - c_H)/\langle c \rangle$ in the

form of a mesh of iso-F_{st} lines (black solid lines) and iso-ε lines (red dashed lines). The meshes formed by the iso-F_{st} and iso-ε lines demonstrate that a given average segment density $\langle c \rangle$ (or equivalently, a given brush height H) can be reached with various combinations of F_{st} and ε (or λ), and that a few strong stickers render the brush more box-like than many weak stickers. Moreover, the difference in the area spanned by the meshes illustrates that the diversity of possible morphologies is larger for brushes in good solvent than in θ solvent.
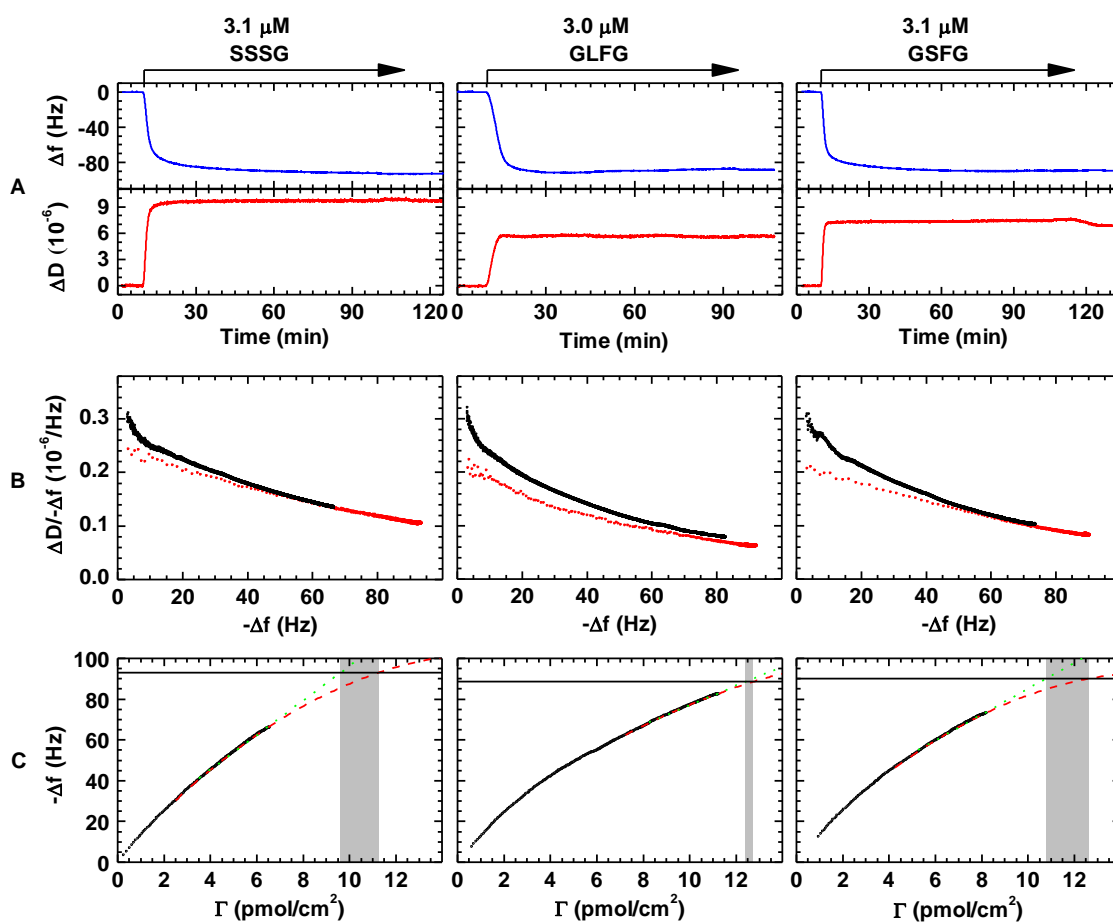
Figure IV.S3 Estimation of grafting densities for QCM-D data lacking corresponding SE data. Figure IV.2 illustrates that the maximal grafting density practically attainable in the combined SE/QCM-D measurements is ~6.5 pmol/cm2 for SSSG, ~9 pmol/cm2 for GSFG and 11 pmol/cm2 for GLFG. Essentially, this is because the incubation conditions required for combined SE/QCM-D measurements limit the applicable solution concentration (because during the brief initial stirring for solution homogenization (cf. Materials and Methods) binding should remain low). In independent QCM-D measurements, however, higher grafting densities can be reached, because these can be performed at higher concentrations, and with the application of

flow adsorption which is additionally enhanced when binding is mass-transport limited. To be able to cover a large range of grafting densities in the comparison of theory with experiment (Figure IV.5), we therefore performed independent QCM-D measurements using a Q-Sense E4 system equipped with flow modules (Biolin Scientific AB; flow rate 5 µL/min). The FG domain concentration for these measurements was 3 µM, and we determined the film thickness at the end of the film formation processes by viscoelastic modeling. To estimate the grafting density, we extrapolated reference curves that relate Δf (measured by QCM-D) with Γ (measured by SE) obtained from combined SE/QCM-D measurements.

(A) FG domain film formation monitored in independent QCM-D measurements. Arrows on top of each panel indicate the start and duration of incubation with different sample solutions; during remaining times, the surface was exposed to working buffer. (B) $\Delta D/-\Delta f$ vs. $-\Delta f$ plots obtained from the data in A (independent QCM-D measurements; red symbols) and in Figure IV.2 (corresponding QCM-D measurements combined with SE; black symbols). Data for large values of $-\Delta f$ superpose well, demonstrating that the film morphology at high coverage is not affected by the different incubation conditions. The reduced $\Delta D/-\Delta f$ values for low $-\Delta f$ in the independent QCM-D measurements are likely due to heterogeneous surface coverage in the initial phase of film formation (which is strongly affected by mass transport limitations). (C) Representative reference curves (black open circles), obtained from the data in Figure IV.2. Towards high grafting densities, extrapolation of a linear fit to the experimental data over the largest 3 pmol/cm2 available (green dotted line) provides an upper bound of Δf, and extrapolation of a quadratic fit over the largest 4 pmol/cm2 available (red dashed line) a lower bound. The intersections of the interpolation lines with the experimentally determined frequency shift (after film formation and rinsing) for the independent QCM-D data (black horizontal line) thus determine the error range in the grafting density (indicated as grey shaded area).

V   Conclusions and perspectives

The objective of this thesis was to elucidate physical principles that underlie the structure, mechanics and dynamic re-organization of HA-rich matrices. To address this question, a systematic study covering distinct levels of matrix complexity was performed. Salient structural and mechanical features of both native HA-rich ECM and *in-vitro* reconstituted HA matrices at given conditions, which reflect the physical principles of interest, were obtained from characterizations using AFM with optical microscopy, and RICM and QCM-D, respectively. The properties of supramolecular assemblies were linked to individual molecular features using polymer physics theory. In the next paragraphs, the main findings of this study and the potential development and impact on future studies are summarized.

V.1   CONCLUSIONS

We first successfully quantified the micromechanical response of an example of native HA-rich matrix, the COC matrix, to compression by colloidal probe AFM. The matrix was confirmed to be elastic rather than plastic or viscous. With a tailored immobilization procedure and size of the colloidal probe, we determined the most compliant parts of mouse COC matrix to have a Young's modulus below 1 Pa. To our knowledge, this is the lowest elastic modulus thus far determined for any mammalian tissue. Another salient feature of the COC compressive mechanics is marked stiffening in response to stress, which suggests a heterogeneous network structure in which mesh size increases with distance from the oocyte perimeter. Through the combination of mechanical and optical analysis, we discovered the presence of a thick cumulus free coat that is particularly pronounced around *in-vivo* expanded matrix. The COC matrix heterogeneity and the unique combination of elasticity and extreme softness may be functionally important, in particular for the maintenance of COC integrity during transport through the oviduct and for the proper selection, capture and guidance of sperm.

Thereafter, we systematically analyzed the impact of a broad range of Ca^{2+} concentrations and pH on structural and mechanical properties of a simplified *in-vitro* model of HA-rich matrices, the HA brush. The variations of thickness and softness of HA brushes were characterized by RICM and QCM-D, respectively. On one hand, we found the softness and thickness of HA brushes to be exquisitely sensitive to Ca^{2+}

concentrations but essentially insensitive to pH within the physiologically relevant ranges of these two parameters. These results are relevant for rationalizing the basic physical properties of HA-rich matrices in biological systems. On the other hand, by viewing a broad range of Ca^{2+} concentrations and pH, we discovered that the effect of divalent calcium ions on HA brush thickness is virtually identical to the effect of monovalent sodium ions at 10-fold higher concentrations, and that HA brushes collapse upon protonation below pH 6.0.

Last but not least, we developed a mean-field theory to describe the effect of physical (reversible) cross-links on the morphology of polymer brushes. This theory connects the molecular properties of the constituents with the behaviour of the supramolecular assemblies. The theory predicts that the compaction and changes in the density profile due to cross-links is equivalent to an effective reduction in excluded volume (*i.e.* a reduction in solvent quality) in the presence of weak cross-linking, whereas stronger cross-linking makes the density profile more box-like than a reduction in solvent quality for a given brush thickness. Specifically, a desired modulation of brush thickness can be achieved with either a few strong stickers or many weak stickers, but a few strong stickers make the brush density profile more box-like than many weak stickers. By using the theory to analyze experimental data on regular neo-FG-domain brushes (a model of the nuclear pore permeability barrier that has in common with HA-rich matrices that it is made from flexible polymers), we quantified properties that were not directly accessible in experiments, such as the strength of individual inter-FG-motif interactions (which are rather weak, in the millimolar range) and the fraction of FG motifs that is simultaneously engaged in cross-linking at FG domain concentrations that are likely to prevail in the nuclear pore. Comparison of experiment also confirmed the applicability of our theory.

V.2   PERSPECTIVES

Many questions remain that are related to the work in this thesis that can be potentially developed in the future and facilitate a more comprehensive understanding of the physical principles underlying the structure, mechanics and dynamic reorganization of HA-rich matrices.

The micromechanical properties of native matrix, as we acquired on the COC matrix in this thesis, are potentially mapped at higher resolution in three dimensions upon improvement of the AFM setup and/or proper deconstruction of the complex native

matrix (e.g. cut the matrix into slices or dissociate the outer layer(s) by controlled method). Such a mapping of micro or nanomechanical properties can be correlated with future structural studies that measure the permeability of the matrix directly with probes of different size and thus reflect the fine structure (*i.e.* mesh size and mesh size distribution) of the matrix. Although varying environmental conditions impact on all components within the native matrix and consequently identifying the contribution of each component is challenging, it is possible to quantitatively characterize the structural and mechanical properties of the matrix analogously in the presence of specific activator/inhibitor of selected component to understand how the selected component contribute to the matrix features. Indeed, the methods we have established should also be valuable for characterization of hyaluronan-rich matrices in a wide range of other cells and tissues.

Potential future work on *in-vitro* reconstituted HA brushes includes comparative studies of the effect of different divalent ions, and possibly also monovalent and trivalent ions on brush thickness, which may resolve the question of the mechanism underlying the ten-fold potentiation of calcium over sodium ions with regard to brush thickness variations. Moreover, the organization in native HA-rich matrices is far more complex than the HA brushes investigated in this thesis. By adding other components of native matrices, more complex *in-vitro* models can be reconstituted and analogous mechanical and structural characterization can be performed on such more complex *in-vitro* model, which should bring us closer to the behaviour of the native HA-rich matrices. The results can benefit the rational design of synthetic HA-rich materials with tailored properties (e.g. stimuli-responsive surface coatings).

We obtained good agreement between the developed theory describing the impact of physical cross-links on polymer brush morphology and experimental data regarding neo-FG-domain brushes as models of the nuclear pore permeability barrier in this thesis. However, there are many more biological systems bearing resemblance to a physically cross-linked brush, such as pericellular coats rich in HA that can be mimicked in *in-vitro* studies by HA brushes as we used in this thesis. The case of such HA brushes is somewhat different from the assumptions in our developed theory in that soluble HA-binding proteins constitute the cross-linking nodes and that the local stiffening of HA chains makes the properties of the brush distinct. Extensions of the model presented in this thesis are required to capture these distinct features of HA brush, or other biologically relevant systems. The theoretical model with further improvements should

be of interest for the design of synthetic brushes with novel properties, and also for understanding morphological remodeling and transport phenomena in other biological systems.

More generally, our results reflecting the physical principles underlying key features of HA-rich matrices can potentially be integrated with the research on intracellular space, to build up a comprehensive path of mechanotransduction covering dual directions between the interstitial space and the nuclear. Moreover, the physical principles found in this thesis can be combined with relevant biochemical principles, to reveal how both aspects regulate each other. Finally, interventions that exploit ultrastructural or mechanical properties based on physical principles can be potentially considered for therapeutic applications that complement drugs designed relying on biochemical interactions.

References

1. Frantz, C., K. M. Stewart, and V. M. Weaver. 2010. The extracellular matrix at a glance. J. Cell Sci. 123:4195-4200.
2. Mouw, J. K., G. Ou, and V. M. Weaver. 2014. Extracellular matrix assembly: a multiscale deconstruction. Nat. Rev. Mol. Cell Biol. 15:771-785.
3. Naba, A., K. R. Clauser, H. Ding, C. A. Whittaker, S. A. Carr, and R. O. Hynes. 2016. The extracellular matrix: Tools and insights for the "omics" era. Matrix Biol. 49:10-24.
4. Humphrey, J. D., E. R. Dufresne, and M. A. Schwartz. 2014. Mechanotransduction and extracellular matrix homeostasis. Nat. Rev. Mol. Cell Biol. 15:802-812.
5. Hynes, R. O. 2009. The extracellular matrix: not just pretty fibrils. Science 326:1216-1219.
6. Charras, G., and E. Sahai. 2014. Physical influences of the extracellular environment on cell migration. Nat. Rev. Mol. Cell Biol. 15:813-824.
7. Campbell, I. D., and M. J. Humphries. 2011. Integrin structure, activation, and interactions. Cold Spring Harb. Perspect. Biol. 3.
8. Rozario, T., and D. W. DeSimone. 2010. The extracellular matrix in development and morphogenesis: a dynamic view. Dev. Biol. 341:126-140.
9. Bonnans, C., J. Chou, and Z. Werb. 2014. Remodelling the extracellular matrix in development and disease. Nat. Rev. Mol. Cell Biol. 15:786-801.
10. Daley, W. P., S. B. Peters, and M. Larsen. 2008. Extracellular matrix dynamics in development and regenerative medicine. J. Cell Sci. 121:255-264.
11. Fraser, J. R., T. C. Laurent, and U. B. Laurent. 1997. Hyaluronan: its nature, distribution, functions and turnover. J. Intern. Med. 242:27-33.
12. Laurent, T. C., and J. R. Fraser. 1992. Hyaluronan. FASEB J. 6:2397-2404.
13. Almond, A., A. Brass, and J. K. Sheehan. 2000. Oligosaccharides as model systems for understanding water−biopolymer interaction: Hydrated dynamics of a hyaluronan decamer. J. Phys. Chem. B 104:5634-5640.
14. Cleland, R. L., J. L. Wang, and D. M. Detweiler. 1982. Polyelectrolyte properties of sodium hyaluronate. 2. Potentiometric titration of hyaluronic acid. Macromolecules 15:386-395.
15. Day, A. J., and J. K. Sheehan. 2001. Hyaluronan: polysaccharide chaos to protein organisation. Curr. Opin. Struct. Biol. 11:617-622.
16. Cleland, R. L. 1977. The persistence length of hyaluronic acid: an estimate from small-angle x-ray scattering and intrinsic viscosity. Arch. Biochem. Biophys. 180:57-68.
17. Fouissac, E., M. Milas, M. Rinaudo, and R. Borsali. 1992. Influence of the ionic strength on the dimensions of sodium hyaluronate. Macromolecules 25:5613-5617.
18. Weigel, P. H., V. C. Hascall, and M. Tammi. 1997. Hyaluronan synthases. J. Biol. Chem. 272:13997-14000.
19. Fan, Z., F. Zhang, T. Liu, and B. Q. Zuo. 2014. Effect of hyaluronan molecular weight on structure and biocompatibility of silk fibroin/hyaluronan scaffolds. Int. J. Biol. Macromol. 65:516-523.
20. Attili, S., O. V. Borisov, and R. P. Richter. 2012. Films of end-grafted hyaluronan are a prototype of a brush of a strongly charged, semiflexible

polyelectrolyte with intrinsic excluded volume. Biomacromolecules 13:1466-1477.

21. Grundelova, L., A. Mracek, V. Kasparkova, A. Minarik, and P. Smolka. 2013. The influence of quarternary salt on hyaluronan conformation and particle size in solution. Carbohydr. Polym. 98:1039-1044.

22. Suzuki, T., M. Suzuki, S. Ogino, R. Umemoto, N. Nishida, and I. Shimada. 2015. Mechanical force effect on the two-state equilibrium of the hyaluronan-binding domain of CD44 in cell rolling. Proc. Natl. Acad. Sci. U. S. A. 112:6991-6996.

23. Wolny, P. M., S. Banerji, C. Gounou, A. R. Brisson, A. J. Day, D. G. Jackson, and R. P. Richter. 2010. Analysis of CD44-hyaluronan interactions in an artificial membrane system: insights into the distinct binding properties of high and low molecular weight hyaluronan. J. Biol. Chem. 285:30170-30180.

24. Hall, C. L., and E. A. Turley. 1995. Hyaluronan: RHAMM mediated cell locomotion and signaling in tumorigenesis. J. Neurooncol. 26:221-229.

25. Hamilton, S. R., S. F. Fard, F. F. Paiwand, C. Tolg, M. Veiseh, C. Wang, J. B. McCarthy, M. J. Bissell, J. Koropatnick, and E. A. Turley. 2007. The hyaluronan receptors CD44 and Rhamm (CD168) form complexes with ERK1,2 that sustain high basal motility in breast cancer cells. J. Biol. Chem. 282:16667-16680.

26. Baranova, N. S., E. Nileback, F. M. Haller, D. C. Briggs, S. Svedhem, A. J. Day, and R. P. Richter. 2011. The inflammation-associated protein TSG-6 cross-links hyaluronan via hyaluronan-induced TSG-6 oligomers. J. Biol. Chem. 286:25675-25686.

27. Baranova, N. S., S. J. Foulcer, D. C. Briggs, V. Tilakaratna, J. J. Enghild, C. M. Milner, A. J. Day, and R. P. Richter. 2013. Inter-alpha-inhibitor impairs TSG-6-induced hyaluronan cross-linking. J. Biol. Chem. 288:29642-29653.

28. Baranova, N. S., A. Inforzato, D. C. Briggs, V. Tilakaratna, J. J. Enghild, D. Thakar, C. M. Milner, A. J. Day, and R. P. Richter. 2014. Incorporation of pentraxin 3 into hyaluronan matrices is tightly regulated and promotes matrix cross-linking. J. Biol. Chem. 289:30481-30498.

29. Attili, S., and R. P. Richter. 2013. Self-assembly and elasticity of hierarchical proteoglycan-hyaluronan brushes. Soft Matter 9:10473-10483.

30. Toole, B. P. 1990. Hyaluronan and its binding proteins, the hyaladherins. Curr. Opin. Cell Biol. 2:839-844.

31. Chen, W. Y., and G. Abatangelo. 1999. Functions of hyaluronan in wound repair. Wound Repair Regen. 7:79-89.

32. Koochekpour, S., G. J. Pilkington, and A. Merzak. 1995. Hyaluronic acid/CD44H interaction induces cell detachment and stimulates migration and invasion of human glioma cells in vitro. Int. J. Cancer 63:450-454.

33. Hardingham, T. E., and H. Muir. 1972. The specific interaction of hyaluronic acid with cartilage proteoglycan. Biochim. Biophys. Acta 279:401-405.

34. Watanabe, H., Y. Yamada, and K. Kimata. 1998. Roles of aggrecan, a large chondroitin sulfate proteoglycan, in cartilage structure and function. J. Biochem. 124:687-693.

35. Wu, Y. J., D. P. L. A. Pierre, J. Wu, A. J. Yee, and B. B. Yang. 2005. The interaction of versican with its binding partners. Cell Res. 15:483-494.

36. Day, A. J., and C. A. de la Motte. 2005. Hyaluronan cross-linking: a protective mechanism in inflammation? Trends Immunol. 26:637-643.

37. Marei, W. F., F. Ghafari, and A. A. Fouladi-Nashta. 2012. Role of hyaluronic acid in maturation and further early embryo development of bovine oocytes. Theriogenology 78:670-677.

38. Salustri, A., A. Camaioni, M. Di Giacomo, C. Fulop, and V. Hascall. 1999. Hyaluronan and proteoglycans in ovarian follicles. Hum. Reprod. Update 5:293-301.

39. Toole, B. P., and V. C. Hascall. 2002. Hyaluronan and tumor growth. Am. J. Pathol. 161:745-747.

40. Lu, P., V. M. Weaver, and Z. Werb. 2012. The extracellular matrix: a dynamic niche in cancer progression. J. Cell Biol. 196:395-406.

41. Plotnikov, S. V., A. M. Pasapera, B. Sabass, and C. M. Waterman. 2012. Force fluctuations within focal adhesions mediate ECM-rigidity sensing to guide directed cell migration. Cell 151:1513-1527.

42. Discher, D. E., P. Janmey, and Y. L. Wang. 2005. Tissue cells feel and respond to the stiffness of their substrate. Science 310:1139-1143.

43. Hadjipanayi, E., V. Mudera, and R. A. Brown. 2009. Close dependence of fibroblast proliferation on collagen scaffold matrix stiffness. J. Tissue Eng. Regen. Med. 3:77-84.

44. Lo, C.-M., H.-B. Wang, M. Dembo, and Y.-l. Wang. 2000. Cell movement is guided by the rigidity of the substrate. Biophys. J. 79:144-152.

45. Pathak, A., and S. Kumar. 2012. Independent regulation of tumor cell migration by matrix stiffness and confinement. Proc. Natl. Acad. Sci. U. S. A. 109:10334-10339.

46. Engler, A. J., S. Sen, H. L. Sweeney, and D. E. Discher. 2006. Matrix elasticity directs stem cell lineage specification. Cell 126:677-689.

47. Wang, H.-B., M. Dembo, and Y.-L. Wang. 2000. Substrate flexibility regulates growth and apoptosis of normal but not transformed cells. Am. J. Physiol. Cell Physiol. 279:C1345-C1350.

48. Paszek, M. J., N. Zahir, K. R. Johnson, J. N. Lakins, G. I. Rozenberg, A. Gefen, C. A. Reinhart-King, S. S. Margulies, M. Dembo, D. Boettiger, D. A. Hammer, and V. M. Weaver. 2005. Tensional homeostasis and the malignant phenotype. Cancer Cell 8:241-254.

49. Evanko, S. P., M. I. Tammi, R. H. Tammi, and T. N. Wight. 2007. Hyaluronan-dependent pericellular matrix. Adv. Drug Deliv. Rev 59:1351-1365.

50. Han, L., A. J. Grodzinsky, and C. Ortiz. 2011. Nanomechanics of the Cartilage Extracellular Matrix. Annu Rev Mater Res 41:133-168.

51. Talbot, P., C. Geiske, and M. Knoll. 1999. Oocyte pickup by the mammalian oviduct. Mol. Biol. Cell 10:5-8.

52. Schneider, A., G. Francius, R. Obeid, P. Schwinte, J. Hemmerle, B. Frisch, P. Schaaf, J. C. Voegel, B. Senger, and C. Picart. 2006. Polyelectrolyte multilayers with a tunable Young's modulus: influence of film stiffness on cell adhesion. Langmuir 22:1193-1200.

53. Russell, D. L., and A. Salustri. 2006. Extracellular matrix of the cumulus-oocyte complex. Semin. Reprod. Med. 24:217-227.

54. Mochizuki, S., H. Vink, O. Hiramatsu, T. Kajita, F. Shigeto, J. A. Spaan, and F. Kajiya. 2003. Role of hyaluronic acid glycosaminoglycans in shear-induced endothelium-derived nitric oxide release. Am. J. Physiol. Heart Circ. Physiol. 285:H722-726.

55. Egeblad, M., M. G. Rasch, and V. M. Weaver. 2010. Dynamic interplay between the collagen scaffold and tumor evolution. Curr. Opin. Cell Biol. 22:697-706.

56. Kass, L., J. T. Erler, M. Dembo, and V. M. Weaver. 2007. Mammary epithelial cell: influence of extracellular matrix composition and organization during development and tumorigenesis. Int. J. Biochem. Cell Biol. 39:1987-1994.

57. Russell, D. L., and R. L. Robker. 2007. Molecular mechanisms of ovulation: co-ordination through the cumulus complex. Hum. Reprod. Update 13:289-312.

58. Chen, F. H., K. T. Rousche, and R. S. Tuan. 2006. Technology Insight: adult stem cells in cartilage regeneration and tissue engineering. Nat Clin Pract Rheum 2:373-382.

59. Esko, J. D., K. Kimata, and U. Lindahl. 2009. Proteoglycans and sulfated glycosaminoglycans. In Essentials of Glycobiology. A. Varki, R. D. Cummings, J. D. Esko, H. H. Freeze, P. Stanley, C. R. Bertozzi, G. W. Hart, and M. E. Etzler, editors. Cold Spring Harbor Laboratory Press, NY.

60. Uyama, T., H. Kitagawa, and K. Sugahara. 2007. Biosynthesis of Glycosaminoglycans and Proteoglycans. In Comprehensive Glycoscience. J. P. Kamerling, editor. Elsevier, Oxford. 79-104.

61. Taylor, K. R., and R. L. Gallo. 2006. Glycosaminoglycans and their proteoglycans: host-associated molecular patterns for initiation and modulation of inflammation. FASEB J. 20:9-22.

62. Ori, A., M. C. Wilkinson, and D. G. Fernig. 2008. The heparanome and regulation of cell function: structures, functions and challenges. Front. Biosci. 13:4309-4338.

63. Nap, R. J., and I. Szleifer. 2008. Structure and interactions of aggrecans: statistical thermodynamic approach. Biophys. J. 95:4570-4583.

64. Cain, S. A., C. Baldock, J. Gallagher, A. Morgan, D. V. Bax, A. S. Weiss, C. A. Shuttleworth, and C. M. Kielty. 2005. Fibrillin-1 interactions with heparin. Implications for microfibril and elastic fiber assembly. J. Biol. Chem. 280:30526-30537.

65. Cain, S. A., A. K. Baldwin, Y. Mahalingam, B. Raynal, T. A. Jowitt, C. A. Shuttleworth, J. R. Couchman, and C. M. Kielty. 2008. Heparan sulfate regulates fibrillin-1 N- and C-terminal interactions. J. Biol. Chem. 283:27017-27027.

66. Meyer, K., and J. W. Palmer. 1934. The polysaccharide of the vitreous humor. J. Biol. Chem. 107:629-634.

67. Weissmann, B., and K. Meyer. 1954. The structure of hyalobiuronic acid and of haluronic acid from umbilical cord1,2. J. Am. Chem. Soc. 76:1753-1757.

68. Hascall, V. C., and J. D. Esko. 2009. Hyaluronan. In Essentials of Glycobiology. A. Varki, R. D. Cummings, J. D. Esko, H. H. Freeze, P. Stanley, C. R. Bertozzi, G. W. Hart, and M. E. Etzler, editors. Cold Spring Harbor Laboratory Press, NY.

69. Scott, J. E., C. Cummings, A. Brass, and Y. Chen. 1991. Secondary and tertiary structures of hyaluronan in aqueous solution, investigated by rotary shadowing-electron microscopy and computer simulation. Hyaluronan is a very efficient network-forming polymer. Biochem. J. 274 (Pt 3):699-705.

70. Scott, J. E., and F. Heatley. 1999. Hyaluronan forms specific stable tertiary structures in aqueous solution: a 13C NMR study. Proc. Natl. Acad. Sci. U. S. A. 96:4850-4855.

71. Gribbon, P., B. C. Heng, and T. E. Hardingham. 1999. The molecular basis of the solution properties of hyaluronan investigated by confocal fluorescence recovery after photobleaching. Biophys. J. 77:2210-2216.

72. Gribbon, P., B. C. Heng, and T. E. Hardingham. 2000. The analysis of intermolecular interactions in concentrated hyaluronan solutions suggest no evidence for chain-chain association. Biochem. J. 350:329-335.

73. DeAngelis, P. L., and P. H. Weigel. 1994. Immunochemical confirmation of the primary structure of streptococcal hyaluronan synthase and synthesis of high molecular weight product by the recombinant enzyme. Biochemistry 33:9033-9039.

74. Markovitz, A., J. A. Cifonelli, and A. Dorfman. 1959. The biosynthesis of hyaluronic acid by group A Streptococcus. VI. Biosynthesis from uridine nucleotides in cell-free extracts. J. Biol. Chem. 234:2343-2350.

75. Philipson, L. H., and N. B. Schwartz. 1984. Subcellular localization of hyaluronate synthetase in oligodendroglioma cells. J. Biol. Chem. 259:5017-5023.

76. Prehm, P. 1984. Hyaluronate is synthesized at plasma membranes. Biochem. J. 220:597-600.

77. Cyphert, J. M., C. S. Trempus, and S. Garantziotis. 2015. Size matters: molecular weight specificity of hyaluronan effects in cell biology. Int. J. Cell Biol. 2015:563818.

78. Prehm, P. 1983. Synthesis of hyaluronate in differentiated teratocarcinoma cells. Mechanism of chain growth. Biochem. J. 211:191-198.

79. Hascall, V. C., D. K. Heinegård, and T. N. Wight. 1991. Proteoglycans. In Cell Biology of Extracellular Matrix: Second Edition. E. D. Hay, editor. Springer US, Boston, MA. 149-175.

80. Prehm, P. 2006. Biosynthesis of hyaluronan: direction of chain elongation. Biochem. J. 398:469-473.

81. Lidholt, K., J. L. Weinke, C. S. Kiser, F. N. Lugemwa, K. J. Bame, S. Cheifetz, J. Massagué, U. Lindahl, and J. D. Esko. 1992. A single mutation affects both N-acetylglucosaminyltransferase and glucuronosyltransferase activities in a Chinese hamster ovary cell mutant defective in heparan sulfate biosynthesis. Proc. Natl. Acad. Sci. U. S. A. 89:2267-2271.

82. Lidholt, K., and M. Fjelstad. 1997. Biosynthesis of the escherichia coli K4 capsule polysaccharide. A parallel system for studies of glycosyltransferases in chondroitin formation. J. Biol. Chem. 272:2682-2687.

83. Salustri, A., C. Garlanda, E. Hirsch, M. De Acetis, A. Maccagno, B. Bottazzi, A. Doni, A. Bastone, G. Mantovani, P. Beck Peccoz, G. Salvatori, D. J. Mahoney, A. J. Day, G. Siracusa, L. Romani, and A. Mantovani. 2004. PTX3 plays a key role in the organization of the cumulus oophorus extracellular matrix and in in vivo fertilization. Development 131:1577-1586.

84. Eppig, J. J. 1980. Regulation of cumulus oophorus expansion by gonadotropins in vivo and in vitro. Biol. Reprod. 23:545-552.

85. Salustri, A., M. Yanagishita, C. B. Underhill, T. C. Laurent, and V. C. Hascall. 1992. Localization and synthesis of hyaluronic acid in the cumulus cells and mural granulosa cells of the preovulatory follicle. Dev. Biol. 151:541-551.

86. Salustri, A., M. Yanagishita, and V. C. Hascall. 1989. Synthesis and accumulation of hyaluronic acid and proteoglycans in the mouse cumulus cell-oocyte complex during follicle-stimulating hormone-induced mucification. J. Biol. Chem. 264:13840-13847.

87. Fülöp, C., R. V. Kamath, Y. Li, J. M. Otto, A. Salustri, B. R. Olsen, T. T. Glant, and V. C. Hascall. 1997. Coding sequence, exon–intron structure and chromosomal localization of murine TNF-stimulated gene 6 that is specifically expressed by expanding cumulus cell–oocyte complexes. Gene 202:95-102.

88. Fülöp, C., A. Salustri, and V. C. Hascall. 1997. Coding sequence of a hyaluronan synthase homologue expressed during expansion of the mouse cumulus-oocyte complex. Arch. Biochem. Biophys. 337:261-266.

89. Schoenfelder, M., and R. Einspanier. 2003. Expression of hyaluronan synthases and corresponding hyaluronan receptors is differentially regulated during oocyte maturation in cattle. Biol. Reprod. 69:269-277.

90. Kimura, N., Y. Konno, K. Miyoshi, H. Matsumoto, and E. Sato. 2002. Expression of hyaluronan synthases and CD44 messenger RNAs in porcine cumulus-oocyte complexes during in vitro maturation. Biol. Reprod. 66:707-717.

91. Itano, N., T. Sawai, M. Yoshida, P. Lenas, Y. Yamada, M. Imagawa, T. Shinomura, M. Hamaguchi, Y. Yoshida, Y. Ohnuki, S. Miyauchi, A. P. Spicer, J. A. McDonald, and K. Kimata. 1999. Three isoforms of mammalian hyaluronan synthases have distinct enzymatic properties. J. Biol. Chem. 274:25085-25092.

92. Alho, A. M., and C. B. Underhill. 1989. The hyaluronate receptor is preferentially expressed on proliferating epithelial cells. J. Cell Biol. 108:1557-1565.

93. Ohta, N., H. Saito, T. Kuzumaki, T. Takahashi, M. M. Ito, T. Saito, K. Nakahara, and M. Hiroi. 1999. Expression of CD44 in human cumulus and mural granulosa cells of individual patients in in-vitro fertilization programmes. Mol. Hum. Reprod. 5:22-28.

94. Ball, G. D., M. L. Leibfried, R. W. Lenz, R. L. Ax, B. D. Bavister, and N. L. First. 1983. Factors affecting successful in vitro fertilization of bovine follicular oocytes. Biol. Reprod. 28:717-725.

95. Laufer, N., B. C. Tarlatzis, and F. Naftolin. 1984. In vitro fertilization: state of the art. In Semin. Reprod. Endocrinol. Copyright© 1984 by Thieme Medical Publishers, Inc. 197-219.

96. Foote, R. H. 1987. In vitro fertilization and embryo transfer in domestic animals: applications in animals and implications for humans. J. In Vitro Fert. Embryo Transf. 4:73-88.

97. Fatehi, A. N., B. A. J. Roelen, B. Colenbrander, E. J. Schoevers, B. M. Gadella, M. M. Bevers, and R. van den Hurk. 2005. Presence of cumulus cells during in vitro fertilization protects the bovine oocyte against oxidative stress and improves first cleavage but does not affect further development. Zygote 13:177-185.

98. Davis, B. J., D. E. Lennard, C. A. Lee, H. F. Tiano, S. G. Morham, W. C. Wetsel, and R. Langenbach. 1999. Anovulation in cyclooxygenase-2-deficient mice is restored by prostaglandin E2 and interleukin-1beta. Endocrinology 140:2685-2695.

99. Lam, X., C. Gieseke, M. Knoll, and P. Talbot. 2000. Assay and importance of adhesive interaction between hamster (mesocricetus auratus) oocyte-cumulus complexes and the oviductal epithelium. Biol. Reprod. 62:579-588.

100. Talbot, P., B. D. Shur, and D. G. Myles. 2003. Cell adhesion and fertilization: steps in oocyte transport, sperm-zona pellucida interactions, and sperm-egg fusion. Biol. Reprod. 68:1-9.

101. Mahi-Brown, C. A., and R. Yanagimachi. 1983. Parameters influencing ovum pickup by oviductal fimbria in the golden hamster. Gamete Res. 8:1-10.

102. Odor, D. L., and R. J. Blandau. 1973. EGG transport over the fimbrial surface of the rabbit oviduct under experimental conditions. Fertil. Steril. 24:292-300.

103. Eisenbach, M., and I. Tur-Kaspa. 1999. Do human eggs attract spermatozoa? Bioessays 21:203-210.

104. Van Soom, A., S. Tanghe, I. De Pauw, D. Maes, and A. de Kruif. 2002. Function of the cumulus oophorus before and during mammalian fertilization. Reprod Domestic Anim 37:144-151.

105. Hong, S. J., P. C. Chiu, K. F. Lee, J. M. Tse, P. C. Ho, and W. S. Yeung. 2004. Establishment of a capillary-cumulus model to study the selection of sperm for fertilization by the cumulus oophorus. Hum. Reprod. 19:1562-1569.

106. Drahorád, J., J. Tesařík, D. Čechová, and V. Vilím. 1991. Proteins and glycosaminoglycans in the intercellular matrix of the human cumulus-oophorus and their effect on conversion of proacrosin to acrosin. Reproduction 93:253-262.

107. Tesařik, J., L. Pilka, J. Drahorád, D. Čechová, and L. Veselský. 1988. The role of cumulus cell-secreted proteins in the development of human sperm fertilizing ability: implication in IVF. Hum. Reprod. 3:129-132.

108. Talbot, P., and G. DiCarlantonio. 1984. Architecture of the hamster oocyte-cumulus complex. Gamete Res. 9:261-272.

109. Yudin, A. I., G. N. Cherr, and D. F. Katz. 1988. Structure of the cumulus matrix and zona pellucida in the golden hamster: a new view of sperm interaction with oocyte-associated extracellular matrices. Cell Tissue Res. 251:555-564.

110. Cherr, G. N., A. I. Yudin, and D. F. Katz. 1990. Organization of the hamster cumulus extracellular matrix: A hyaluronate-glycoprotein gel which modulates sperm access to the oocyte. Dev. Growth Differ. 32:353-365.

111. Yokoo, M., Y. Miyahayashi, T. Naganuma, N. Kimura, H. Sasada, and E. Sato. 2002. Identification of hyaluronic acid-binding proteins and their expressions in porcine cumulus-oocyte complexes during in vitro maturation. Biol. Reprod. 67:1165-1171.

112. Bourguignon, L. Y., H. Zhu, B. Zhou, F. Diedrich, P. A. Singleton, and M. C. Hung. 2001. Hyaluronan promotes CD44v3-Vav2 interaction with Grb2-p185(HER2) and induces Rac1 and Ras signaling during ovarian tumor cell migration and growth. J. Biol. Chem. 276:48679-48692.

113. Misra, S., S. Ghatak, and B. P. Toole. 2005. Regulation of MDR1 expression and drug resistance by a positive feedback loop involving hyaluronan, phosphoinositide 3-kinase, and ErbB2. J. Biol. Chem. 280:20310-20315.

114. Ghatak, S., S. Misra, and B. P. Toole. 2005. Hyaluronan constitutively regulates ErbB2 phosphorylation and signaling complex formation in carcinoma cells. J. Biol. Chem. 280:8875-8883.

115. Krasilnikov, M. A. 2000. Phosphatidylinositol-3 kinase dependent pathways: the role in control of cell growth, survival, and malignant transformation. Biochemistry (Mosc.) 65:59-67.

116. Zheng Shu, X., Y. Liu, F. S. Palumbo, Y. Luo, and G. D. Prestwich. 2004. In situ crosslinkable hyaluronan hydrogels for tissue engineering. Biomaterials 25:1339-1348.

117. Borzacchiello, A., L. Russo, B. M. Malle, K. Schwach-Abdellaoui, and L. Ambrosio. 2015. Hyaluronic acid based hydrogels for regenerative medicine applications. Biomed Res Int 2015:871218.

118. Vanderhooft, J. L., M. Alcoutlabi, J. J. Magda, and G. D. Prestwich. 2009. Rheological properties of cross-linked hyaluronan-gelatin hydrogels for tissue engineering. Macromol. Biosci. 9:20-28.

119. Burdick, J. A., C. Chung, X. Jia, M. A. Randolph, and R. Langer. 2005. Controlled degradation and mechanical behavior of photopolymerized hyaluronic acid networks. Biomacromolecules 6:386-391.

120. Jeon, O., S. J. Song, K.-J. Lee, M. H. Park, S.-H. Lee, S. K. Hahn, S. Kim, and B.-S. Kim. 2007. Mechanical properties and degradation behaviors of hyaluronic acid hydrogels cross-linked at various cross-linking densities. Carbohydr Polym. 70:251-257.

121. Ouasti, S., R. Donno, F. Cellesi, M. J. Sherratt, G. Terenghi, and N. Tirelli. 2011. Network connectivity, mechanical properties and cell adhesion for hyaluronic acid/PEG hydrogels. Biomaterials 32:6456-6470.

122. Miller, K., K. Chinzei, G. Orssengo, and P. Bednarz. 2000. Mechanical properties of brain tissue in-vivo: experiment and computer simulation. J. Biomech. 33:1369-1376.

123. O'Callaghan, R., K. M. Job, R. O. Dull, and V. Hlady. 2011. Stiffness and heterogeneity of the pulmonary endothelial glycocalyx measured by atomic force microscopy. Am. J. Physiol. Lung Cell Mol. Physiol. 301:L353-360.

124. McLane, L. T., P. Chang, A. Granqvist, H. Boehm, A. Kramer, J. Scrimgeour, and J. E. Curtis. 2013. Spatial organization and mechanical properties of the pericellular matrix on chondrocytes. Biophys. J. 104:986-996.

125. Prein, C., N. Warmbold, Z. Farkas, M. Schieker, A. Aszodi, and H. Clausen-Schaumann. 2016. Structural and mechanical properties of the proliferative zone of the developing murine growth plate cartilage assessed by atomic force microscopy. Matrix Biol. 50:1-15.

126. Carr, M. E., and N. M. Hadler. 1980. Permeability of hyaluronic acid solutions. Arthritis Rheum. 23:1371-1375.

127. Gabriel, D. A., and M. E. Carr, Jr. 1989. Calcium destabilizes and causes conformational changes in hyaluronic acid. Am. J. Med. Sci. 298:8-14.

128. Napier, M. A., and N. M. Hadler. 1978. Effect of calcium on structure and function of a hyaluronic acid matrix: carbon-13 nuclear magnetic resonance analysis and the diffusional behavior of small solutes. Proc. Natl. Acad. Sci. U. S. A. 75:2261-2265.

129. Ghosh, K., X. Z. Shu, R. Mou, J. Lombardi, G. D. Prestwich, M. H. Rafailovich, and R. A. Clark. 2005. Rheological characterization of in situ cross-linkable hyaluronan hydrogels. Biomacromolecules 6:2857-2865.

130. Attili, S., and R. P. Richter. 2012. Combining colloidal probe atomic force and reflection interference contrast microscopy to study the compressive mechanics of hyaluronan brushes. Langmuir 28:3206-3216.

131. Fujii, T., Y. L. Sun, K. N. An, and Z. P. Luo. 2002. Mechanical properties of single hyaluronan molecules. J. Biomech. 35:527-531.

132. Nilebäck, E., F. Westberg, J. Deinum, and S. Svedhem. 2010. Viscoelastic sensing of conformational changes in plasminogen induced upon binding of low molecular weight compounds. Anal. Chem. 82:8374-8376.

133. Nilebäck, E., L. Feuz, H. Uddenberg, R. Valiokas, and S. Svedhem. 2011. Characterization and application of a surface modification designed for QCM-D studies of biotinylated biomolecules. Biosens. Bioelectron. 28:407-413.

134. Rebsdat, S., and D. Mayer. 2000. Ethylene Glycol. In Ullmann's Encyclopedia of Industrial Chemistry. Wiley-VCH Verlag GmbH & Co. KGaA.

135. Chen, X., W. W. Qoutah, P. Free, J. Hobley, D. G. Fernig, and D. Paramelle. 2012. Features of thiolated ligands promoting resistance to ligand exchange in self-assembled monolayers on gold nanoparticles. Aust. J. Chem. 65:266-274.

136. Prime, K. L., and G. M. Whitesides. 1993. Adsorption of proteins onto surfaces containing end-attached oligo(ethylene oxide): a model system using self-assembled monolayers. J. Am. Chem. Soc. 115:10714-10721.

137. Hoffmann, J., J. Groll, J. Heuts, H. Rong, D. Klee, G. Ziemer, M. Moeller, and H. P. Wendel. 2006. Blood cell and plasma protein repellent properties of star-PEG-modified surfaces. J. Biomater. Sci. Polym. Ed. 17:985-996.

138. Lokanathan, A. R., S. Zhang, V. R. Regina, M. A. Cole, R. Ogaki, M. Dong, F. Besenbacher, R. L. Meyer, and P. Kingshott. 2011. Mixed poly (ethylene glycol) and oligo (ethylene glycol) layers on gold as nonfouling surfaces created by backfilling. Biointerphases 6:180-188.

139. Ostuni, E., L. Yan, and G. M. Whitesides. 1999. The interaction of proteins and cells with self-assembled monolayers of alkanethiolates on gold and silver. Colloids Surf. B. Biointerfaces 15:3-30.

140. Chen, S., J. Zheng, L. Li, and S. Jiang. 2005. Strong resistance of phosphorylcholine self-assembled monolayers to protein adsorption: insights into nonfouling properties of zwitterionic materials. J. Am. Chem. Soc. 127:14473-14478.

141. Migliorini, E., D. Thakar, R. Sadir, T. Pleiner, F. Baleux, H. Lortat-Jacob, L. Coche-Guerente, and R. P. Richter. 2014. Well-defined biomimetic surfaces to characterize glycosaminoglycan-mediated interactions on the molecular, supramolecular and cellular levels. Biomaterials 35:8903-8915.

142. Altgarde, N., E. Nileback, L. de Battice, I. Pashkuleva, R. L. Reis, J. Becher, S. Moller, M. Schnabelrauch, and S. Svedhem. 2013. Probing the biofunctionality of biotinylated hyaluronan and chondroitin sulfate by hyaluronidase degradation and aggrecan interaction. Acta Biomater. 9:8158-8166.

143. Haeussling, L., H. Ringsdorf, F. J. Schmitt, and W. Knoll. 1991. Biotin-functionalized self-assembled monolayers on gold: surface plasmon optical studies of specific recognition reactions. Langmuir 7:1837-1840.

144. Richter, R. P., K. K. Hock, J. Burkhartsmeyer, H. Boehm, P. Bingen, G. Wang, N. F. Steinmetz, D. J. Evans, and J. P. Spatz. 2007. Membrane-grafted hyaluronan films: a well-defined model system of glycoconjugate cell coats. J. Am. Chem. Soc. 129:5306-5307.

145. Binnig, G., C. F. Quate, and C. Gerber. 1986. Atomic force microscope. Phys. Rev. Lett. 56:930-933.

146. Hutter, J. L., and J. Bechhoefer. 1993. Calibration of atomic force microscope tips. Rev. Sci. Instrum 64:1868-1873.

147. Franze, K., M. Francke, K. Gunter, A. F. Christ, N. Korber, A. Reichenbach, and J. Guck. 2011. Spatial mapping of the mechanical properties of the living retina using scanning force microscopy. Soft Matter 7:3147-3154.

148. Gautier, H. O. B., A. J. Thompson, S. Achouri, D. E. Koser, K. Holtzmann, E. Moeendarbary, and K. Franze. 2015. Atomic force microscopy based force measurements on animal cells and tissues. In Methods Cell Biol. K. P. Ewa, editor. Academic Press. 211-235.

149. Ng, L., H. H. Hung, A. Sprunt, S. Chubinskaya, C. Ortiz, and A. Grodzinsky. 2007. Nanomechanical properties of individual chondrocytes and their developing growth factor-stimulated pericellular matrix. J. Biomech. 40:1011-1023.

150. Staunton, J. R., B. L. Doss, S. Lindsay, and R. Ros. 2016. Correlating confocal microscopy and atomic force indentation reveals metastatic cancer cells stiffen during invasion into collagen I matrices. Sci. Rep. 6:19686.

151. Guo, D., J. Li, G. Xie, Y. Wang, and J. Luo. 2014. Elastic properties of polystyrene nanospheres evaluated with atomic force microscopy: size effect and error analysis. Langmuir 30:7206-7212.

152. Stolz, M., R. Gottardi, R. Raiteri, S. Miot, I. Martin, R. Imer, U. Staufer, A. Raducanu, M. Duggelin, W. Baschong, A. U. Daniels, N. F. Friederich, A. Aszodi, and U. Aebi. 2009. Early detection of aging cartilage and osteoarthritis in mice and patient samples using atomic force microscopy. Nat. Nanotechnol. 4:186-192.

153. Butt, H.-J. 1991. Electrostatic interaction in atomic force microscopy. Biophys. J. 60:777-785.

154. Ducker, W. A., T. J. Senden, and R. M. Pashley. 1991. Direct measurement of colloidal forces using an atomic force microscope. Nature 353:239-241.

155. Feiler, A., M. A. Plunkett, and M. W. Rutland. 2003. Atomic force microscopy measurements of adsorbed polyelectrolyte layers. 1. Dynamics of forces and friction. Langmuir 19:4173-4179.

156. Dimitriadis, E. K., F. Horkay, J. Maresca, B. Kachar, and R. S. Chadwick. 2002. Determination of elastic moduli of thin layers of soft material using the atomic force microscope. Biophys. J. 82:2798-2810.

157. Butt, H.-J., B. Cappella, and M. Kappl. 2005. Force measurements with the atomic force microscope: Technique, interpretation and applications. Surf. Sci. Rep. 59:1-152.

158. Hertz, H. 1881. Ueber die Berührung fester elastischer Körper. J. Reine Angew. Math. 92:156-171.

159. Poisson, S. D. 1827. Note sur l'Extension des Fils et des Plaques élastiques. Ann. Chim. Phys. 36:384-387.

160. Greaves, G. N., A. L. Greer, R. S. Lakes, and T. Rouxel. 2011. Poisson's ratio and modern materials. Nat Mater 10:823-837.

161. Reviakine, I., D. Johannsmann, and R. P. Richter. 2011. Hearing what you cannot see and visualizing what you hear: interpreting quartz crystal microbalance data from solvated interfaces. Anal. Chem. 83:8838-8848.

162. Johannsmann, D. 2008. Viscoelastic, mechanical, and dielectric measurements on complex samples with the quartz crystal microbalance. Phys. Chem. Chem. Phys. 10:4516-4534.

163. Marx, K. A. 2003. Quartz crystal microbalance: a useful tool for studying thin polymer films and complex biomolecular systems at the solution-surface interface. Biomacromolecules 4:1099-1120.

164. Valasek, J. 1921. Piezo-electric and allied phenomena in rochelle salt. Phys. Rev. 17:475-481.

165. Rodahl, M., F. Höök, A. Krozer, P. Brzezinski, and B. Kasemo. 1995. Quartz crystal microbalance setup for frequency and Q‐factor measurements in gaseous and liquid environments. Rev. Sci. Instrum 66:3924-3930.

166. Sauerbrey, G. 1959. Verwendung von Schwingquarzen zur Wägung dünner Schichten und zur Mikrowägung. Z. Phys. 155:206-222.

167. Eisele, N. B., F. I. Andersson, S. Frey, and R. P. Richter. 2012. Viscoelasticity of thin biomolecular films: a case study on nucleoporin phenylalanine-glycine repeats grafted to a histidine-tag capturing QCM-D sensor. Biomacromolecules 13:2322-2332.

168. Curtis, A. S. 1964. The mechanism of adhesion of cells to glass. a study by interference reflection microscopy. J. Cell Biol. 20:199-215.

169. Limozin, L., and K. Sengupta. 2009. Quantitative reflection interference contrast microscopy (RICM) in soft matter and cell adhesion. Chemphyschem 10:2752-2768.

170. Weber, I. 2001. Interference reflection microscopy. In eLS. John Wiley & Sons, Ltd.

171. Kühner, M., and E. Sackmann. 1996. Ultrathin hydrated dextran films grafted on glass: preparation and characterization of structural, viscous, and elastic properties by quantitative microinterferometry. Langmuir 12:4866-4876.

172. Raedler, J., and E. Sackmann. 1992. On the measurement of weak repulsive and frictional colloidal forces by reflection interference contrast microscopy. Langmuir 8:848-853.

173. Flory, P. J. 1953. Principles of polymer chemistry. Cornell University Press, Ithaca,.

174. de Gennes, P. G. 1979. Scaling concepts in polymer physics. Cornell University Press, Ithaca, N.Y.

175. Rubinstein, M., and R. H. Colby. 2003. Polymer physics. Oxford University Press, Oxford ; New York.

176. de Gennes, P. G. 1976. Scaling theory of polymer adsorption. J. Phys. France 37:1445-1452.

177. Pincus, P. 1991. Colloid stabilization with grafted polyelectrolytes. Macromolecules 24:2912-2919.

178. Zhulina, E. B., J. Klein Wolterink, and O. V. Borisov. 2000. Screening effects in a polyelectrolyte brush: self-consistent-field theory. Macromolecules 33:4945-4953.

179. Borisov, O. V., E. B. Zhulina, and T. M. Birshtein. 1994. Diagram of the states of a grafted polyelectrolyte layer. Macromolecules 27:4795-4803.

180. Eisele, N. B., A. A. Labokha, S. Frey, D. Gorlich, and R. P. Richter. 2013. Cohesiveness tunes assembly and morphology of FG nucleoporin domain meshworks - Implications for nuclear pore permeability. Biophys J 105:1860-1870.

181. Zhulina, Y. B., V. A. Pryamitsyn, and O. V. Borisov. 1989. Structure and conformational transitions in grafted polymer chain layers. A new theory. Polym. Sci. (USSR) 31:205-216.

182. Zhulina, E. B., O. V. Borisov, and V. A. Priamitsyn. 1990. Theory of steric stabilization of colloid dispersions by grafted polymers. J. Colloid Interface Sci. 137:495-511.

183. Chakrabarti, A., and R. Toral. 1990. Density profile of terminally anchored polymer chains: a Monte Carlo study. Macromolecules 23:2016-2021.

184. Murat, M., and G. S. Grest. 1989. Structure of a grafted polymer brush: a molecular dynamics simulation. Macromolecules 22:4054-4059.

185. de Gennes, P. G. 1987. Polymers at an interface; a simplified view. Adv. Colloid Interface Sci. 27:189-209.

186. Milner, S. T., T. A. Witten, and M. E. Cates. 1988. Theory of the grafted polymer brush. Macromolecules 21:2610-2619.

187. Milner, S. T. 1991. Polymer brushes. Science 251:905-914.

188. Zhulina, E. B., O. V. Borisov, and T. M. Birshtein. 1992. Structure of grafted polyelectrolyte layer. J. Phys. II France 2:63-74.

189. Zhulina, E. B., and O. V. Borisov. 1997. Structure and interaction of weakly charged polyelectrolyte brushes: Self-consistent field theory. J. Chem. Phys. 107:5952-5967.

190. Chen, L., S. J. Mao, and W. J. Larsen. 1992. Identification of a factor in fetal bovine serum that stabilizes the cumulus extracellular matrix. A role for a member of the inter-alpha-trypsin inhibitor family. J. Biol. Chem. 267:12380-12386.

191. Fülöp, C., S. Szántó, D. Mukhopadhyay, T. Bárdos, R. V. Kamath, M. S. Rugg, A. J. Day, A. Salustri, V. C. Hascall, T. T. Glant, and K. Mikecz. 2003. Impaired cumulus mucification and female sterility in tumor necrosis factor-induced protein-6 deficient mice. Development 130:2253-2261.

192. Zhuo, L., M. Yoneda, M. Zhao, W. Yingsung, N. Yoshida, Y. Kitagawa, K. Kawamura, T. Suzuki, and K. Kimata. 2001. Defect in SHAP-hyaluronan complex causes severe female infertility. A study by inactivation of the bikunin gene in mice. J. Biol. Chem. 276:7693-7696.

193. Scarchilli, L., A. Camaioni, B. Bottazzi, V. Negri, A. Doni, L. Deban, A. Bastone, G. Salvatori, A. Mantovani, G. Siracusa, and A. Salustri. 2007. PTX3 interacts with inter-alpha-trypsin inhibitor: implications for hyaluronan organization and cumulus oophorus expansion. J. Biol. Chem. 282:30161-30170.

194. Rienzi, L., G. Vajta, and F. Ubaldi. 2011. Predictive value of oocyte morphology in human IVF: a systematic review of the literature. Hum. Reprod. Update 17:34-45.

195. Dunn, P. F., and B. F. Picologlou. 1976. Viscoelastic properties of cumulus oophorus. Biorheology 13:379-384.

196. Blandau, R. J., and J. L. Boling. 1973. An experimental approach to the study of egg transport through the oviducts of mammals. In Regulation of mammalian reproduction. S. J. Segal, R. Crozier, P. A. Corfman, and P. G. Condliffe, editors. Springfield, Illinois, Charles C. Thomas, United States. 400-415.

197. Boehm, H., T. A. Mundinger, C. H. J. Boehm, V. Hagel, U. Rauch, J. P. Spatz, and J. E. Curtis. 2009. Mapping the mechanics and macromolecular organization of hyaluronan-rich cell coats. Soft Matter 5:4331-4337.

198. Gambini, C., B. Abou, A. Ponton, and Annemiek J. M. Cornelissen. 2012. Micro- and Macrorheology of Jellyfish Extracellular Matrix. Biophys. J. 102:1-9.

199. Sokolov, I., S. Iyer, V. Subba-Rao, R. M. Gaikwad, and C. D. Woodworth. 2007. Detection of surface brush on biological cells in vitro with atomic force microscopy. Appl. Phys. Lett. 91:023902.

200. Lu, Y. B., K. Franze, G. Seifert, C. Steinhauser, F. Kirchhoff, H. Wolburg, J. Guck, P. Janmey, E. Q. Wei, J. Kas, and A. Reichenbach. 2006. Viscoelastic properties of individual glial cells and neurons in the CNS. Proc. Natl. Acad. Sci. U. S. A. 103:17759-17764.

201. Di Giacomo, M., A. Camaioni, F. G. Klinger, R. Bonfiglio, and A. Salustri. 2016. Cyclic AMP-elevating Agents Promote Cumulus Cell Survival and Hyaluronan Matrix Stability, Thereby Prolonging the Time of Mouse Oocyte Fertilizability. J. Biol. Chem. 291:3821-3836.

202. Naldini, L., U. Blomer, P. Gallay, D. Ory, R. Mulligan, F. H. Gage, I. M. Verma, and D. Trono. 1996. In vivo gene delivery and stable transduction of nondividing cells by a lentiviral vector. Science 272:263-267.

203. Sneddon, I. N. 1965. The relation between load and penetration in the axisymmetric boussinesq problem for a punch of arbitrary profile. Int. J. Eng. Sci. 3:47-57.

204. Liu, C., E. S. Litscher, S. Mortillo, Y. Sakai, R. A. Kinloch, C. L. Stewart, and P. M. Wassarman. 1996. Targeted disruption of the mZP3 gene results in production of eggs lacking a zona pellucida and infertility in female mice. Proc. Natl. Acad. Sci. U. S. A. 93:5431-5436.

205. Rico, F., P. Roca-Cusachs, N. Gavara, R. Farré, M. Rotger, and D. Navajas. 2005. Probing mechanical properties of living cells by atomic force microscopy with blunted pyramidal cantilever tips. Physical Review E 72:021914.

206. Levental, I., P. C. Georges, and P. A. Janmey. 2007. Soft biological materials and their impact on cell function. Soft Matter 3:299-306.

207. Velegol, D., and F. Lanni. 2001. Cell traction forces on soft biomaterials. I. Microrheology of type I collagen gels. Biophys. J. 81:1786-1792.

208. Hu, Y., X. Zhao, J. J. Vlassak, and Z. Suo. 2010. Using indentation to characterize the poroelasticity of gels. Appl. Phys. Lett. 96:121904.

209. Moeendarbary, E., L. Valon, M. Fritzsche, A. R. Harris, D. A. Moulding, A. J. Thrasher, E. Stride, L. Mahadevan, and G. T. Charras. 2013. The cytoplasm of living cells behaves as a poroelastic material. Nat Mater 12:253-261.

210. Lieleg, O., and K. Ribbeck. 2011. Biological Hydrogels as Selective Diffusion Barriers. Trends Cell Biol. 21:543-551.

211. Dunning, K. R., M. Lane, H. M. Brown, C. Yeo, R. L. Robker, and D. L. Russell. 2007. Altered composition of the cumulus-oocyte complex matrix during in vitro maturation of oocytes. Hum. Reprod. 22:2842-2850.

212. Drobnis, E. Z., A. I. Yudin, G. N. Cherr, and D. F. Katz. 1988. Kinematics of hamster sperm during penetration of the cumulus cell matrix. Gamete Res. 21:367-383.

213. Coticchio, G., M. A. Bonu, R. Sciajno, E. Sereni, V. Bianchi, and A. Borini. 2007. Truths and myths of oocyte sensitivity to controlled rate freezing. Reproductive BioMedicine Online 15:24-30.

214. Cappella, B., and G. Dietler. 1999. Force-distance curves by atomic force microscopy. Surf. Sci. Rep. 34:1-104.

215. Johnson, K. L., K. Kendall, and A. D. Roberts. 1971. Surface Energy and the Contact of Elastic Solids. Proc. R. Soc. London, Ser. A 324:301-313.

216. Bourguignon, L. Y., V. B. Lokeshwar, X. Chen, and W. G. Kerrick. 1993. Hyaluronic acid-induced lymphocyte signal transduction and HA receptor (GP85/CD44)-cytoskeleton interaction. J. Immunol. 151:6634-6644.

217. Fraser, S. P. 1997. Hyaluronan activates calcium-dependent chloride currents in Xenopus oocytes. FEBS Lett. 404:56-60.

218. Jessen, T. E., and L. Odum. 2004. TSG-6 and calcium ions are essential for the coupling of inter-alpha-trypsin inhibitor to hyaluronan in human synovial fluid. Osteoarthritis Cartilage 12:142-148.

219. Lenormand, H., and J.-C. Vincent. 2011. pH effects on the hyaluronan hydrolysis catalysed by hyaluronidase in the presence of proteins: Part II. The electrostatic hyaluronan – Protein complexes. Carbohydr. Polym. 85:303-311.

220. Morra, M., and C. Cassineli. 1999. Non-fouling properties of polysaccharide-coated surfaces. J. Biomater. Sci. Polym. Ed. 10:1107-1124.

221. Horkay, F., P. J. Basser, D. J. Londono, A. M. Hecht, and E. Geissler. 2009. Ions in hyaluronic acid solutions. J. Chem. Phys. 131:184902.

222. Buhler, E., and F. Boué. 2004. Chain persistence length and structure in hyaluronan solutions: Ionic strength dependence for a model semirigid polyelectrolyte. Macromolecules 37:1600-1610.

223. Chakrabarti, B., and E. A. Balazs. 1973. Optical properties of hyaluronic acid: Ultraviolet circular dichroism and optical rotatory dispersion. J. Mol. Biol. 78:135-141.

224. Winter, W. T., and S. Arnott. 1977. Hyaluronic acid: the role of divalent cations in conformation and packing. J. Mol. Biol. 117:761-784.

225. Gatej, I., M. Popa, and M. Rinaudo. 2005. Role of the pH on hyaluronan behavior in aqueous solution. Biomacromolecules 6:61-67.

226. Maleki, A., A. L. Kjøniksen, and N. Bo. 2008. Effect of pH on the behavior of hyaluronic acid in dilute and semidilute aqueous solutions. Macromol. Symp. 274:131–140.

227. Schilling, J., K. Sengupta, S. Goennenwein, A. R. Bausch, and E. Sackmann. 2004. Absolute interfacial distance measurements by dual-wavelength reflection interference contrast microscopy. Phys. Rev. E Stat. Nonlin. Soft Matter Phys. 69:021901.

228. Takahashi, R., S. Al-Assaf, P. A. Williams, K. Kubota, A. Okamoto, and K. Nishinari. 2003. Asymmetrical-flow field-flow fractionation with on-line multiangle light scattering detection. 1. Application to wormlike chain analysis of weakly stiff polymer chains. Biomacromolecules 4:404-409.

229. Ligoure, C., and L. Leibler. 1990. Thermodynamics and kinetics of grafting end-functionalized polymers to an interface. J. Phys. (France) 51:1313-1328.

230. Mohan, C. 2006. Buffers. A guide for the preparation and use of buffers in biological systems. EMD Bioscience

231. Borisov, O. V., Y. B. Zhulina, and T. M. Birshtein. 1988. Constitutional diagram and collapse of grafted chain layers. Polym. Sci. (USSR) 30:772-779.

232. Zhulina, E. B., T. M. Birshtein, V. A. Priamitsyn, and L. I. Klushin. 1995. Inhomogeneous Structure of Collapsed Polymer Brushes Under Deformation. Macromolecules 28:8612-8620.

233. Gura, E., M. Hückel, and P. J. Müller. 1998. Specific degradation of hyaluronic acid and its rheological properties. Polym. Degradation Stab. 59:297-302.

234. Sivasankar, S., S. Subramaniam, and D. Leckband. 1998. Direct molecular level measurements of the electrostatic properties of a protein surface. Proc. Natl. Acad. Sci. U. S. A. 95:12961-12966.

235. Balazs, E. A., and J. Cui. 2013. The story of "Hyaluronan putty". Bioact. Carbohydr. Dietary Fibre 2:143-151.

236. Wu, S., L. Ai, J. Chen, J. Kang, and S. W. Cui. 2013. Study of the mechanism of formation of hyaluronan putty at pH 2.5: Part II—Theoretical analysis. Carbohydr. Polym. 98:1683-1688.

237. Israelachvili, J. N. 2011. Chapter 14 - Electrostatic forces between surfaces in liquids. In Intermolecular and Surface Forces (Third Edition). Academic Press, San Diego. 291-340.

238. Zhulina, E. B., R. Israels, and G. J. Fleer. 1994. Theory of planar polyelectrolyte brush immersed in solution of asymmetric salt. Colloids Surf. A: Physicochem. Eng. Asp. 86:11-24.

239. Zhulina, E. 1996. Equilibrium structure of ionizable polymer brushes. In Solvents and Self-Organization of Polymers. S. E. Webber, P. Munk, and Z. Tuzar, editors. Springer Netherlands, Dordrecht. 227-258.

240. Winter, W. T., and S. Arnott. 1977. Hyaluronic acid: the role of divalent cations in conformation and packing. J. Mol. Biol. 117:761-784.

241. Fujiwara, H. 2007. Principles of optics. In Spectroscopic Ellipsometry. John Wiley & Sons, Ltd. 13-48.

242. Fahrenkrog, B., and U. Aebi. 2003. The nuclear pore complex: nucleocytoplasmic transport and beyond. Nat. Rev. Mol. Cell Biol. 4:757-766.

243. Grossman, E., O. Medalia, and M. Zwerger. 2012. Functional architecture of the nuclear pore complex. Annual review of biophysics 41:557-584.

244. Fernandez-Martinez, J., and M. P. Rout. 2012. A jumbo problem: mapping the structure and functions of the nuclear pore complex. Curr. Opin. Cell Biol. 24:92-99.

245. Floch, A. G., B. Palancade, and V. Doye. 2014. Fifty Years of Nuclear Pores and Nucleocytoplasmic Transport Studies: Multiple Tools Revealing Complex Rules. In Nuclear Pore Complexes and Nucleocytoplasmic Transport - Methods. V. Doye, editor. 1-40.

246. Gorlich, D., and U. Kutay. 1999. Transport between the cell nucleus and the cytoplasm. Annu. Rev. Cell. Dev. Biol. 15:607-660.

247. Keminer, O., and R. Peters. 1999. Permeability of single nuclear pores. Biophys. J. 77:217-228.

248. Yang, W., and S. M. Musser. 2006. Nuclear import time and transport efficiency depend on importin beta concentration. J. Cell Biol. 174:951-961.

249. Mohr, D., S. Frey, T. Fischer, T. Guttler, and D. Gorlich. 2009. Characterisation of the passive permeability barrier of nuclear pore complexes. EMBO J. 28:2541-2553.

250. Denning, D. P., V. Uversky, S. S. Patel, A. L. Fink, and M. Rexach. 2002. The Saccharomyces cerevisiae nucleoporin Nup2p is a natively unfolded protein. J. Biol. Chem. 277:33447-33455.

251. Denning, D. P., S. S. Patel, V. Uversky, A. L. Fink, and M. Rexach. 2003. Disorder in the nuclear pore complex: the FG repeat regions of nucleoporins are natively unfolded. Proc. Natl. Acad. Sci. U. S. A. 100:2450-2455.

252. Denning, D. P., and M. F. Rexach. 2007. Rapid evolution exposes the boundaries of domain structure and function in natively unfolded FG nucleoporins. Mol. Cell. Proteomics 6:272-282.

253. Cronshaw, J. M., A. N. Krutchinsky, W. Zhang, B. T. Chait, and M. J. Matunis. 2002. Proteomic analysis of the mammalian nuclear pore complex. J. Cell Biol. 158:915-927.

254. Schmidt, H. B., and D. Gorlich. 2015. Nup98 FG domains from diverse species spontaneously phase-separate into particles with nuclear pore-like permselectivity. eLife 4:e04251.

255. Frey, S., and D. Gorlich. 2007. A saturated FG-repeat hydrogel can reproduce the permeability properties of nuclear pore complexes. Cell 130:512-523.

256. Frey, S., R. P. Richter, and D. Goerlich. 2006. FG-rich repeats of nuclear pore proteins form a three-dimensional meshwork with hydrogel-like properties. Science 314:815-817.

257. Patel, S. S., B. J. Belmont, J. M. Sante, and M. F. Rexach. 2007. Natively unfolded nucleoporins gate protein diffusion across the nuclear pore complex. Cell 129:83-96.

258. Hulsmann, B. B., A. A. Labokha, and D. Gorlich. 2012. The permeability of reconstituted nuclear pores provides direct evidence for the selective phase model. Cell 150:738-751.

259. Milles, S., D. Mercadante, I. V. Aramburu, M. R. Jensen, N. Banterle, C. Koehler, S. Tyagi, J. Clarke, S. L. Shammas, M. Blackledge, F. Grater, and E. A. Lemke. 2015. Plasticity of an ultrafast interaction between nucleoporins and nuclear transport receptors. Cell 163:734-745.

260. Bayliss, R., T. Littlewood, and M. Stewart. 2000. Structural basis for the interaction between FxFG nucleoporin repeats and importin-beta in nuclear trafficking. Cell 102:99-108.

261. Bayliss, R., S. W. Leung, R. P. Baker, B. B. Quimby, A. H. Corbett, and M. Stewart. 2002. Structural basis for the interaction between NTF2 and nucleoporin FxFG repeats. EMBO J. 21:2843-2853.

262. Isgro, T. A., and K. Schulten. 2005. Binding dynamics of isolated nucleoporin repeat regions to importin-beta. Structure 13:1869-1879.

263. Port, Sarah A., T. Monecke, A. Dickmanns, C. Spillner, R. Hofele, H. Urlaub, R. Ficner, and Ralph H. Kehlenbach. 2015. Structural and Functional Characterization of CRM1-Nup214 Interactions Reveals Multiple FG-Binding Sites Involved in Nuclear Export. Cell Reports 13:690-702.

264. Rout, M. P., and S. R. Wente. 1994. Pores for thought: nuclear pore complex proteins. Trends Cell Biol. 4:357-365.

265. Peters, R. 2009. Translocation through the nuclear pore: Kaps pave the way. Bioessays 31:466-477.

266. Rout, M. P., J. D. Aitchison, A. Suprapto, K. Hjertaas, Y. Zhao, and B. T. Chait. 2000. The yeast nuclear pore complex: composition, architecture, and transport mechanism. J. Cell Biol. 148:635-651.

267. Yamada, J., J. L. Phillips, S. Patel, G. Goldfien, A. Calestagne-Morelli, H. Huang, R. Reza, J. Acheson, V. V. Krishnan, S. Newsam, A. Gopinathan, E. Y. Lau, M. E. Colvin, V. N. Uversky, and M. F. Rexach. 2010. A bimodal distribution of two distinct categories of intrinsically disordered structures with separate functions in FG nucleoporins. Mol. Cell. Proteomics 9:2205-2224.

268. Zahn, R., D. Osmanović, S. Ehret, C. Araya Callis, S. Frey, M. Stewart, C. You, D. Görlich, B. W. Hoogenboom, and R. P. Richter. 2016. A physical model describing the interaction of nuclear transport receptors with FG nucleoporin domain assemblies. eLife 5:e14119.

269. Vovk, A., C. Gu, M. G. Opferman, L. E. Kapinos, R. Y. Lim, R. D. Coalson, D. Jasnow, and A. Zilman. 2016. Simple biophysics underpins collective conformations of the intrinsically disordered proteins of the Nuclear Pore Complex. eLife 5.

270. Bestembayeva, A., A. Kramer, A. A. Labokha, D. Osmanović, I. Liashkovich, E. V. Orlova, I. J. Ford, G. Charras, A. Fassati, and B. W. Hoogenboom. 2015. Nanoscale stiffness topography reveals structure and mechanics of the transport barrier in intact nuclear pore complexes. Nat Nano 10:60-64.

271. Eisele, N. B., S. Frey, J. Piehler, D. Gorlich, and R. P. Richter. 2010. Ultrathin nucleoporin phenylalanine-glycine repeat films and their interaction with nuclear transport receptors. EMBO Rep 11:366-372.

272. Semenov, A. N., and M. Rubinstein. 1998. Thermoreversible Gelation in Solutions of Associative Polymers. 1. Statics. Macromolecules 31:1373-1385.

273. Frey, S., R. P. Richter, and D. Gorlich. 2006. FG-rich repeats of nuclear pore proteins form a three-dimensional meshwork with hydrogel-like properties. Science 314:815-817.

274. Labokha, A. A., S. Gradmann, S. Frey, B. B. Hulsmann, H. Urlaub, M. Baldus, and D. Gorlich. 2013. Systematic analysis of barrier-forming FG hydrogels from Xenopus nuclear pore complexes. EMBO J. 32:204-218.

275. Richter, R. P., K. B. Rodenhausen, N. B. Eisele, and M. Schubert. 2014. Coupling spectroscopic ellipsometry and quartz crystal microbalance to study organic films at the solid-liquid interface. In Ellipsometry of Functional Organic Surfaces and Films. K. Hinrichts, and K.-J. Eichhorn, editors. Springer, Berlin, Heidelberg.

276. Carton, I., A. R. Brisson, and R. P. Richter. 2010. Label-Free Detection of Clustering of Membrane-Bound Proteins. Anal. Chem. 82:9275-9281.

277. Lata, S., M. Gavutis, and J. Piehler. 2006. Monitoring the Dynamics of Ligand−Receptor Complexes on Model Membranes. J. Am. Chem. Soc. 128:6-7.

278. De Feijter, J. A., J. Benjamins, and F. A. Veer. 1978. Ellipsometry as a tool to study the adsorption behavior of synthetic and biopolymers at the air-water interface. Biopolymers 17:1759-1772.

279. Johannsmann, D. QTM Software. http://www2.pc.tu-clausthal.de/dj/software_en.shtml.

280. Johannsmann, D. 1999. Viscoelastic analysis of organic thin films on quartz resonators. Macromol. Chem. Phys. 200:501-516.

281. Zahn, R., D. Osmanovic, S. Ehret, C. Araya Callis, S. Frey, M. Stewart, C. You, D. Gorlich, B. W. Hoogenboom, and R. P. Richter. 2016. A physical model describing the interaction of nuclear transport receptors with FG nucleoporin domain assemblies. eLife 5:e14119.

282. Stirnemann, G., D. Giganti, J. M. Fernandez, and B. J. Berne. 2013. Elasticity, structure, and relaxation of extended proteins under force. Proc. Natl. Acad. Sci. U. S. A. 110:3847-3852.

283. Tu, L. C., G. Fu, A. Zilman, and S. M. Musser. 2013. Large cargo transport by nuclear pores: implications for the spatial organization of FG-nucleoporins. EMBO J. 32:3220-3230.

284. Romeis, D., and M. Lang. 2014. Excluded volume effects in polymer brushes at moderate chain stretching. J. Chem. Phys. 141:104902.

285. Lang, M., M. Hoffmann, R. Dockhorn, M. Werner, and J. U. Sommer. 2013. Fluctuation driven height reduction of crosslinked polymer brushes: a Monte Carlo study. J. Chem. Phys. 139:164903.

286. Hennink, W. E., and C. F. van Nostrum. 2002. Novel crosslinking methods to design hydrogels. Adv. Drug Del. Rev. 54:13-36.

287. Loveless, D. M., N. I. Abu-Lail, M. Kaholek, S. Zauscher, and S. L. Craig. 2006. Reversibly Cross-Linked Surface-Grafted Polymer Brushes. Angew. Chem. Int. Ed. 45:7812-7814.

Appendix - Curriculum Vitae

Name: Xinyue Chen

Education and research experience

Sep. 2012- Present CIC biomaGUNE, Spain	**PhD candidate, Biophysics** *Project*: Understanding the physical principles that underlie the structure and mechanics of glycan-rich extracellular matrices from tissues to supramolecular models in experiment and theory.
Sep. 2010- Sep. 2011 The University of Liverpool, UK	**Master of Research (Distinction), Biochemistry** *Course Included*: Fundamental principles of molecular cell biology and microbial physiology and interactions with surfaces, Glycobiology, Statistics for biologists, *etc.* *Project*: Identifying the quality of self-assembled monolayer (SAM) on gold nanoparticles (NP) affected by ligand structure to improve the NP stability.
Sep. 2004- Jun. 2008 Lanzhou University, China	**Bachelor of Science (Hons, 1st class), Theoretical Physics** *Course Included*: Advanced mathematics, Theoretical mechanics, Quantum mechanics, General theory of relativity, Introductory life sciences (elective), Physical chemistry (elective) *etc.* *Final project*: Robustness of a gene regulatory network.

Professional expertise

Atomic force microscopy, Reflection interference contrast microscopy, Quartz crystal microbalance with dissipation monitoring, Ellipsometry, UV-vis spectroscopy, Micromanipulator, Surface/nanoparticle functionalization, Chromatography, Polymer physics theory, Programming based on Matlab platform.

Award and presentation

Aug. 2015	EMBO student grant & poster, *Physics of Cells: From Molecules to Systems*, Gremany Topic: Micromechanical properties of cumulus cell-oocyte complex matrix.
Jun. 2015	Poster, *Hyaluronan 2015 Conference*, Italy Topic: Mechanical properties of hyaluronan-rich cumulus cell-oocyte complex matrix.
Oct. 2014	Contributed talk, *Fracture of Soft Materials: from soft solids to complex fluids*, France Topic: Quantification of the visco-elastic properties, fracture and recovery of reversibly cross-linked protein/polysaccharide films by colloidal probe AFM.
Jul. 2013	Poster, *Biological Surfaces and Interfaces*, Spain Topic: Quantitative reflection interference contrast microscopy on substrates with multi-layer coatings – a novel tool for characterization of soft interfaces.

List of publications and manuscripts in preparation

Manuscripts related to the PhD project work:

1. X. Chen, R. Bonfiglio, S. Banerji, D. G. Jackson, A. Salustri and R. P. Richter, 2016, Micromechanical analysis of the hyaluronan-rich matrix surrounding the oocyte reveals a uniquely soft and elastic composition, *Biophys. J.*, In press.
2. X. Chen*, R. Zahn*, S. Frey, D. Görlich, O. V. Borisov and R. P. Richter, Morphology and function of the nuclear pore permeability barrier – a case study of cross-linked polymer brushes, manuscript in preparation (target journal: *Biomacromolecules*).
3. X. Chen and R. P. Richter, Effect of calcium ions and pH on the morphology and mechanical properties of hyaluronan brushes, manuscript in preparation (target journal: *Langmuir*).

Other publications:

4. X. Chen, W. W. Qoutah, P. Free, J. Hobley, D. G. Fernig and D. Paramelle, 2012, Features of thiolated ligands promoting resistance to ligand exchange in self-assembled monolayers on gold nanoparticles, *Australian J. Chem.* **65**(3): 266-274.

* Authors contributed equally.

The extracellular matrix (ECM) is the acellular structure of all tissues and essential for multicellular life. Next to biochemical signals, the physical properties of the ECM provide important signals to cells. The polysaccharide hyaluronan (HA) is ubiquitous in the extracellular space of vertebrates and an important structural component of the ECM. HA is a linear, unbranched and regular polymer of the glycosaminoglycan (GAG) family, and serves as a scaffold that responds dynamically to molecular stimuli such as HA-binding proteins, or changes in pH or ionic strength. The objective of this PhD research project is to elucidate physical principles underlying the structure, mechanics and dynamic re-organization of HA-rich matrices. To address this question, we have studied the mechanical properties and morphology of HA-rich matrices at distinct levels of complexity. On one hand, we have studied the cumulus cell-oocyte complex (COC) matrix as an example of complex, native HA-rich tissue. On the other hand, we have studied so-called HA brushes as a well-defined *in vitro* reconstituted model of HA-rich matrices.

The HA-rich matrix in the COC forms around oocytes just before ovulation and plays vital roles in oocyte biology. We have analyzed the micromechanical response of mouse COC matrix by colloidal probe atomic force microscopy (AFM). We found the COC matrix to be extremely soft yet elastic, suggesting a stable gel-like network structure with high porosity and a large mesh size. With a Young's modulus around 1 Pa, COC matrices are among the softest elastic biological materials known to date. In addition, the elastic modulus increased progressively with indentation. Furthermore, using optical microscopy to correlate these mechanical properties with ultra-structure, we discovered that the COC is surrounded by a thick matrix shell that is essentially devoid of cumulus cells. We propose that the pronounced non-linear elastic behaviour of COC matrix is a consequence of structural heterogeneity and serves important functions in biological processes, such as oocyte transport in the oviduct and sperm penetration.

To understand more comprehensively the response of HA polymers to changes in their aqueous environment, the thickness and viscoelastic properties of films of end-grafted HA (also called HA brushes) as a well defined *in vitro* model of HA-rich matrices were characterized by reflection interference contrast microscopy (RICM) and quartz crystal microbalance with dissipation monitoring (QCM-D) as a function of Ca^{2+} concentration and pH. Within the physiological range, the thickness of HA brushes decreased significantly with Ca^{2+} concentration but did not change with pH. By screening a large range of Ca^{2+} concentrations, we discovered that the effect of Ca^{2+} on HA brush thickness is virtually identical to the effect of Na^+ at 10-fold higher concentrations. HA brushes responded only weakly to pH changes above pH 6.0, but showed a sharp collapse around pH 3. Our results provide insights into how HA matrices are affected by solution properties, which is relevant in biological systems and for the design of synthetic tissues.

Finally, using theoretical computations based on self-consistent mean field theory, we elucidated how the morphology of polymer brushes is influenced by the formation of physical cross-links between polymers, such as they would occur in the presence of cross-linking proteins. We find that cross-links promote a denser and more homogeneous brush morphology. The effect of cross-links is comparable to the effect of reduced solvent quality when the density of cross-links is low, but unique features including the retention of solvent even with strong cross-links emerge at high cross-linking densities.

This work provides novel insights into how the supramolecular structure and thus the mechanical properties of HA-rich matrices can be dynamically regulated by changes in microenvironmental conditions. This can be linked to different biological functions of native HA-rich extracellular matrices but is also of interest for the design of tailored, synthetic HA-based materials for applications in tissue engineering.

CIC biomaGUNE

Biomaterialetako Ikerkuntza Kooperatiboko Zentroa
Centro de Investigación Cooperativa en Biomateriales

MAX-PLANCK-GESELLSCHAFT